Study of Photon Production in e^+e^- Collisions at TRISTAN

by

Kangping Karen Hu

Dissertation submitted to the Faculty of the
Virginia Polytechnic Institute and State University
in partial fulfillment of the requirements for the degree of
DOCTOR OF PHILOSOPHY
in
Physics

APPROVED:

Alexander Abashian, Chairman

Kazuo Gotow

Leo Piilonen

L. David Roper

Hsiung Chia Tze

August, 1991

Blacksburg, Virginia

Study of Photon Production

in e^+e^- Collisions at TRISTAN

by

Kangping Karen Hu

Committee Chairman: Alexander Abashian

Physics

(ABSTRACT)

A study of photon production in multi-hadronic final states has been made at center-of-mass energies from 55 to 58 GeV with the AMY detector at the KEK e^+e^- storage ring TRISTAN. The study is based on a data sample of 40.8 pb^{-1} integrated luminosity. The inclusive photon cross sections have been measured, and found to scale with the center-of-mass energies $\sqrt{s}$ as a function of Feynman variable $x = 2\,E_\gamma/\sqrt{s}$, and also found to agree with the results of other experiments. The existence of final state radiation has been confirmed by both the inclusive and isolated photon analyses. The forward-backward charge asymmetry of quark jets with respect to the incoming beam direction in $e^+e^- \rightarrow q\bar{q}\gamma$ processes has been measured to be 0.000 ± 0.102, with the theoretical prediction of -0.112 ± 0.039. A search for a new heavy neutral scalar particle H° via $e^+e^- \rightarrow H^\circ + \gamma$ has been made. The cross section upper limits of this new process are extracted in the H° mass region of 15 to 40 GeV.

Acknowledgements

This thesis would not have been possible without the excellent and diligent work of the KEK staff and all AMY members. Especially, I would like to thank Eun-Joo Kim, Young-Kee Kim and Gu Ping, as my analysis has its roots in portions of theirs. I also thank Eva Low and Hong-Joo Kim, not only for their help and guidance during my stay in KEK, but also for their friendship and kindness.

I would like to express my deepest appreciation to my thesis advisors, Alexander Abashian, Kazuo Gotow and Leo Piilonen, for their continual guidance throughout my graduate studies. I have gained much invaluable knowledge of many things from my assoiation with them. I have benefited from discussions with Winston Ko, Tadao Nozaki and Torbjorn Sjostrand.

Thanks to Kevin Sterner, Mark Mattson and Anzhi Lai for their patience and many discussions on weekly meetings, for making graduate school life "bearable". Special thanks to Chris Thomas, for her help with all the paperworks for the past five years and also for being a friend.

My parents have always encouraged me to believe in my abilities. I will always be indebted to them for all the things they have done for me.

Finally, I dedicate this dissertation to my loving husband, Mark, for his understanding, continual encouragement and support.

Contents

List of Figures

List of Tables

Chapter 1

Introduction

The production of hadrons through e^+e^- annihilation is described as a process in which quark-antiquark pairs, occasionally together with energetic bremsstrahlung gluons, are produced initially. These partons then fragment into hadrons. Hadronic jets are formed in the direction of the initial partons. However, since QCD-based predictions are only valid at the parton level, models are needed to describe the transition from the parton state to the hadronic final state, *i.e.* the fragmentation process. The knowledge of the particle composition of the final states is therefore important for understanding the fragmentation of quarks and gluons into hadrons. In particular, the photons in hadronic final states have the special feature that they can result from the decays of unstable hadrons or from radiative emission by either the incoming electron, positron, or the primary quarks. In the first part of this thesis we present a study of the inclusive photon spectra through the process $e^+e^- \rightarrow \gamma + \textit{hadrons}$.

Photons from the radiative processes off quarks, also called direct photons, could give insight into the fragmentation mechanism. Since photons from radiative processes tend to be isolated from the final state hadronic jets, an isolated photon event analysis is performed to study these photons. New process such as $e^+e^- \rightarrow H^\circ + \gamma$, where H° is a unknown

heavy neutral particle, also could give additional isolated photons in the hadronic final states. We include this new process search in our isolated photon analysis.

This thesis is based on the data taken using the AMY detector at the TRISTAN e^+e^- storage ring at center-of-mass energy $\sqrt{s}$ = 55–58 GeV between 1987 and 1990. It is based on an accumulated luminosity of 40.8 pb^{-1}.

Different sources of photons in hadronic final states are described in this chapter. The description of TRISTAN collider and AMY detector is presented in Chapter 2. The offline analysis, Monte Carlo method, and hadronic event samples used in this analysis are described in Chapter 3. The selection criteria and detailed analysis of inclusive photons are presented in Chapter 4. The isolated photon analysis is presented in Chapter 5. Finally conclusions follow in Chapter 6.

1.1 Hadronic Event Production

In the TRISTAN energy region, hadron production takes place primarily via

$$e^+e^- \rightarrow \gamma/Z^\circ \rightarrow q\,\overline{q}$$

as shown in Figure 1-1, with the quark pair subsequently fragmenting into hadrons. Figure 1-2 shows some examples of higher-order electro-weak corrections to the basic annihilation process. Figure 1-3 shows some examples of higher-order QCD corrections to the basic annihilation process, caused by final state gluon bremsstrahlung.

The Feynman diagram for $e^+e^- \rightarrow q\,\overline{q}$ and $e^+e^- \rightarrow \mu^+\mu^-$ are the same except for the final state fermion charges. Since the quarks fragment into hadrons, it is useful to define the ratio R, the total hadronic cross section in units of the lowest order QED cross section. The lowest order QED cross section for muon pair production at center-of-mass energy $\sqrt{s}$ is given by

$$\sigma(e^+e^- \rightarrow \mu^+\mu^-) \equiv \sigma_{QED} = \frac{4\pi\alpha^2}{3s} = \frac{21.7}{E^2}\,nb\cdot(GeV)^2 \tag{1.1}$$

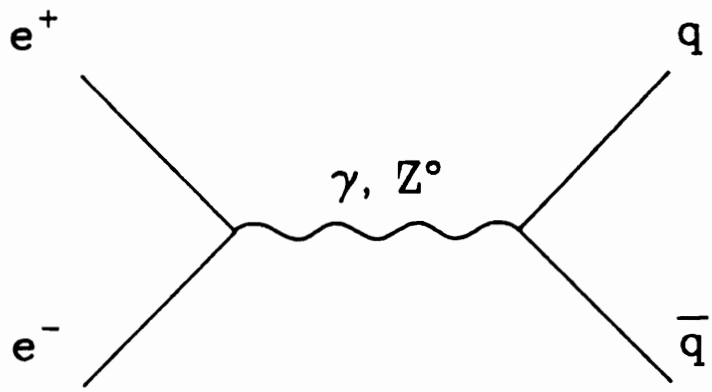

Figure 1-1: e^+e^- annihilation into a $q\,\overline{q}$ pair.

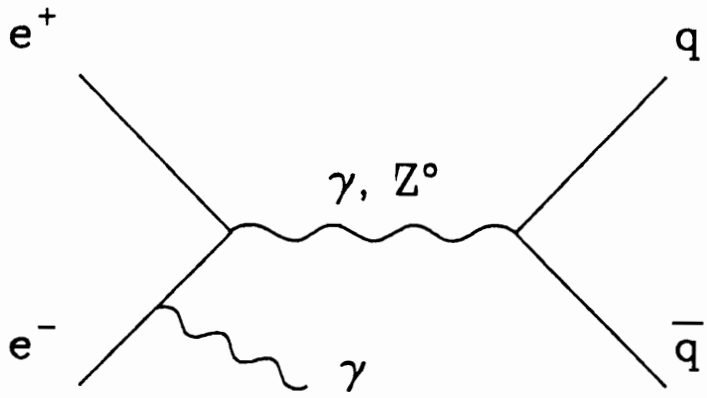

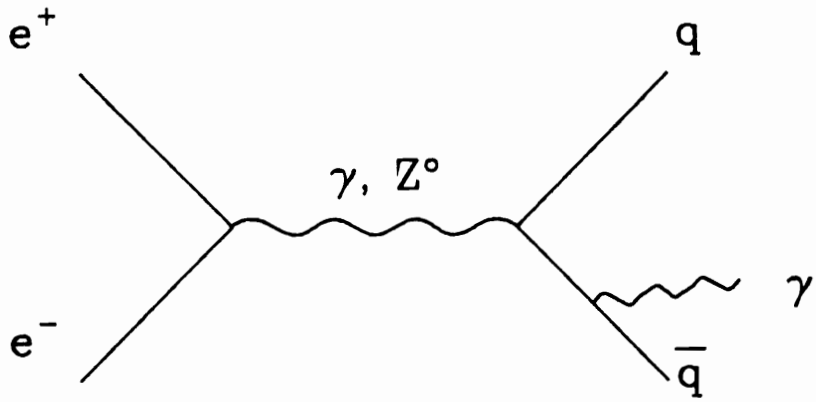

Figure 1-2: Some of higher-order electro-weak corrections.

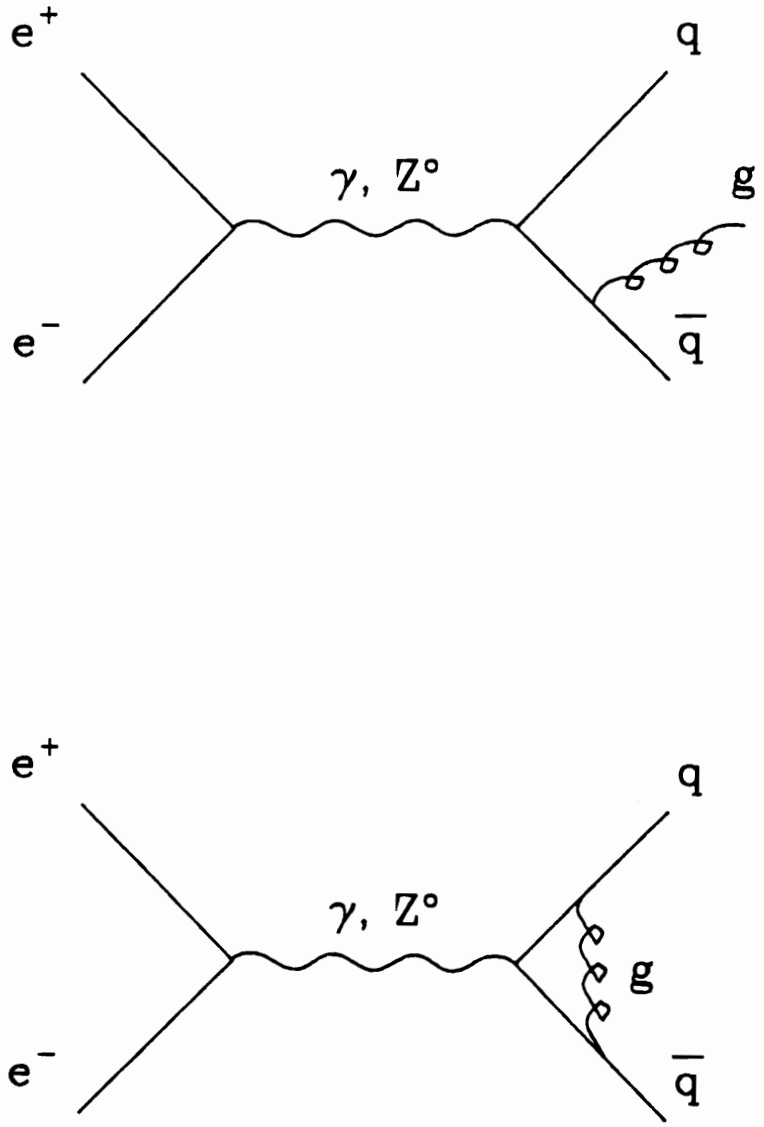

Figure 1-3: Some of Higher-order QCD corrections due to final state gluon bremsstrahlung.

where $E = \sqrt{s}/2$ is the beam energy, and α is the electromagnetic coupling constant.

R is calculated to the lowest order in the QED and QCD theories, R_o, as following:

$$\begin{aligned} R_o &= \frac{\sigma(e^+e^- \rightarrow \gamma \rightarrow hadrons)}{\sigma(e^+e^- \rightarrow \mu^+\mu^-)} \\ &= \frac{\sum_q \sigma(e^+e^- \rightarrow \gamma \rightarrow q\bar{q})}{\sigma(e^+e^- \rightarrow \mu^+\mu^-)} \\ &= 3\sum_q Q_q^2 \end{aligned} \tag{1.2}$$

where the summation is carried over all the quarks with $m_q < \sqrt{s}/2$, Q_q is the quark charge in units of the electron charge, and the factor 3 reflects the three color degrees of freedom of each quark. Therefore R_o is independent of s as long as $\sqrt{s} << M_{Z^o}$.

In the Standard Model, this simple prediction of R_o is modified by higher order QCD effects (C_{QCD}) due to emission of the gluons, and by electro-weak effects (C_{EW}) coming from annihilation via the Z^o boson and the radiative processes [1] [2] [3]. Assuming the velocity of the quark $\beta_q = 1$, which is a good approximation for energies substantially above quark-pair production thresholds [4], the Standard Model predicts

$$\begin{aligned} R &= \frac{\sigma(e^+e^- \rightarrow \gamma/Z^o \rightarrow hadrons)}{\sigma(e^+e^- \rightarrow \mu^+\mu^-)} \\ &= R_o(1 + C_{EW})(1 + C_{QCD}) \\ &= R_o(1 + C_{EW})[1 + \frac{\alpha_s}{\pi} + C_2(\frac{\alpha_s}{\pi})^2 + C_3(\frac{\alpha_s}{\pi})^3 + \cdots] \end{aligned} \tag{1.3}$$

where R_o is given by Equation 1.2, and α_s is the QCD coupling constant at scale $\sqrt{s}$. C_2 and C_3 depend on the renormalization scheme. In the modified minimal subtraction scheme, $C_2 = 1.986 - 0.115\,N_f$ [3] and $C_3 = 70.985 - 1.2\,N_f - 0.005\,N_f^2$ [5], where N_f is the number of quark flavors that can be created in the hadronic events. It is difficult to calculate C_{EW} theoretically in a closed form, and thus it is usually calculated by Monte Carlo methods [6] [7]. At the TRISTAN energies, the correction term C_{EW} is approximately equal to 0.3 [8].

The fragmentation process, in which quarks fragment into hadrons, is not well understood theoretically. Phenomenological models are used for parametrizing this process. There are

three commonly used fragmentation models [9]: the string model [10][11][12], the independent model [13], and the cluster model [14][15][16].

String Fragmentation

The string fragmentation model (used by the Lund JETSET Monte Carlo event generation program) [10] pictures a string connecting the two quarks. The potential energy in the string increases with the increasing separation between the quarks. When the quarks move apart, the potential energy stored in the string increases and the string breaks by the production of a new $q\,\overline{q}$ pair. The fraction of the total available energy which is given to each of the two resulting $q\,\overline{q}$ pairs is given by a probability distribution called the fragmentation function. These $q\,\overline{q}$ pairs again have strings connecting each pair, which can again break. Eventually there is not enough energy between the two quarks to break the string connecting them. The resulting quarks and antiquarks are then combined into hadrons. Two jets of hadrons are thus produced, whose momentum vectors are approximately equal to those of the initial q and $\overline{q}$. Radiated gluons can materialize into additional jets.

Independent Fragmentation

In this model, the initially produced quark q is iteratively connected to a $q'\,\overline{q'}$ pair forming a hadron $H(q\,\overline{q'})$ and another quark q',

$$q \;\rightarrow\; H(q\,\overline{q'}) \;+\; q'$$

and this process is repeated until all the energy is used up. In this model, the hadronization of the different partons is assumed to take place independently of each other, and thus energy and momentum can not be conserved simultaneously.

Cluster Fragmentation

In the cluster fragmentation model, $q\overline{q}$ clusters are formed after the parton shower evolution followed by the imposition of $g \rightarrow q\,\overline{q}$ breakups. Clusters heavier than a cut-off mass M_0 (typically $M_0 = 5\,GeV/c^2$) fragment into lighter clusters. Clusters below the cut-off mass are treated as a superposition of broad, short-lived resonances that decay into known resonances with probabilities proportional to the available phase space.

1.2 Photon Production in Hadronic Final States

Photons in hadronic final states can result from the decays of unstable hadrons or from radiative emission by either the incoming electron or positron in the initial state, or the primary quarks in the final state.

1.2.1 Photons from Unstable Hadron Decays

At energies below half of the beam energy most of the photons result from decays of unstable hadrons, for example π°, η, ω, η' and charm particle. Among these, the majority of photons are associated with π° decays. Photons from hadron decays usually have relatively small energies and appear inside the hadronic jets. This part of the inclusive photon spectra has already been investigated by other experiments at energies below the TRISTAN energy region [17], and is found to scale with the center-of-mass energy as a function of the Feynman variable $x = 2\,E_\gamma/\sqrt{s}$. A study of inclusive photon spectra in this analysis provides a test of scale invariance and of different fragmentation models in the TRISTAN energy region. Our results are given in Chapter 4; also shown are comparisons between our results and other experiments.

1.2.2 Photon Emission by Electrons and Quarks

In the energy region exceeding about half the beam energy, a substantial contribution to the photon yield can be attributed to bremsstrahlung from an electron or positron in the initial state or from a quark in the final state. Those photons are emitted "directly" in the $e^+e^- \rightarrow q\bar{q}\gamma$ process; thus they are called "direct photons". It has long been recognized that direct photons can be used as a powerful tool to explore the properties of the quark-gluon system at short distances, because quarks and gluons fragment into hadrons once they leave the short-distance regime, whereas photons can leave without further interactions. If a photon radiated from a quark is detected with a large transverse momentum relative to the hadron jets, short distances are probed and it is possible to study the properties of the quark-gluon system before the hadron fragmentation takes place.

The first order Feynman diagrams for the $e^+e^- \rightarrow q\bar{q}\gamma$ process are shown in Figure 1-4. Assuming that the interference term is small enough, the differential cross section for the process $q\bar{q}\gamma$ consists of two parts [18],

$$\frac{d\sigma}{dx} = \frac{d\sigma^e}{dx} + \frac{d\sigma^q}{dx} \tag{1.4}$$

where $x = 2\,E_\gamma/\sqrt{s}$, E_γ is the energy of the direct photon, and the differential cross sections of electron and quark bremsstrahlung are, respectively,

$$\frac{d\sigma^e}{dx} = \frac{4\pi\alpha^2}{3s(1-x)}\frac{\alpha}{\pi}[\frac{1+(1-x)^2}{x}](3\sum_q Q_q^2)[\ln(s/m_e^2) - 1] \tag{1.5}$$

$$\frac{d\sigma^q}{dx} = \frac{4\pi\alpha^2}{3s}\frac{\alpha}{\pi}[\frac{1+(1-x)^2}{x}]\,3\sum_q Q_q^4\,[\ln(s(1-x)/m_q^2) - 1] \tag{1.6}$$

where Q_q is the charge of quark q, m_e is the electron mass, and m_q the mass of quark q.

These formulae are valid for $x > 0.01$. The differential cross sections of electron and quark bremsstrahlung at $\sqrt{s} = 60\,GeV$ are shown in Figure 1-5, and the ratio of these differential cross sections is shown in Figure 1-6.

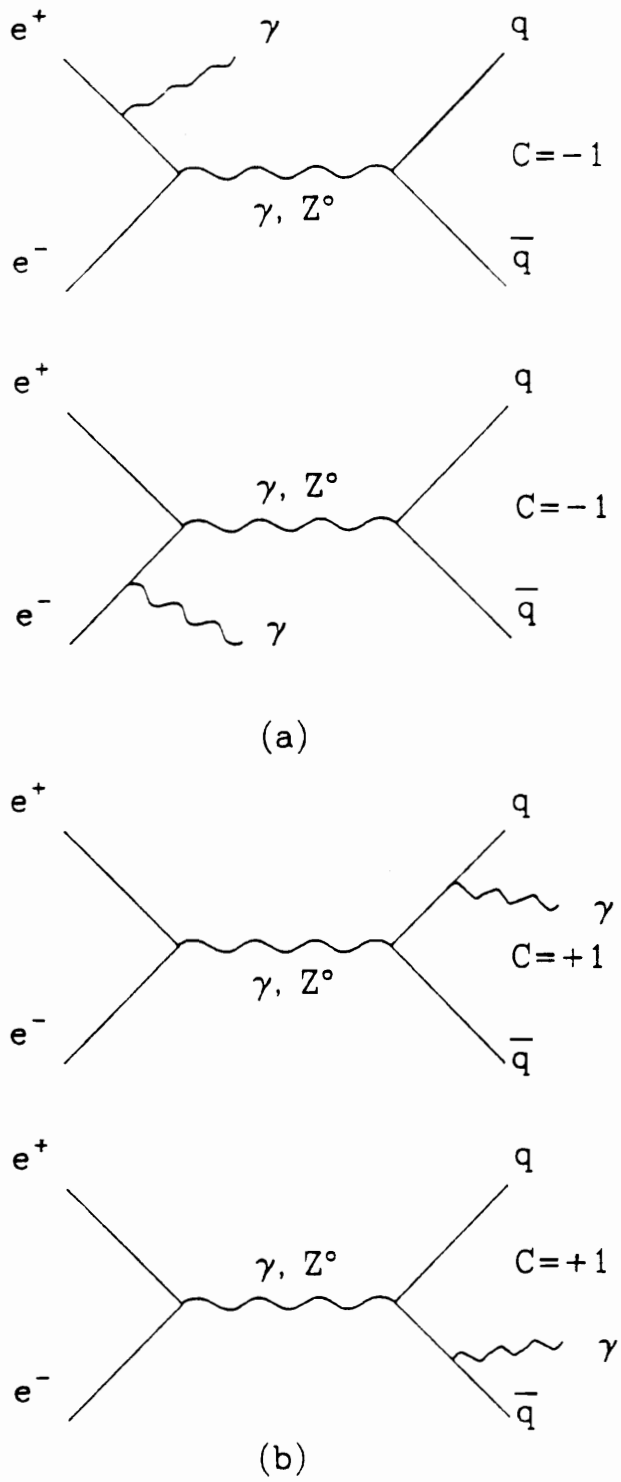

Figure 1-4: (a) Initial state radiation. (b) Final state radiation.

If the interference term is included, the calculation gets very complicated. Laermann *et al.* [19] have calculated the total cross section of the direct photon production, including the contribution from the interference term, in the lowest order assuming photon radiation from massless quarks. Figure 1-7 shows their calculation of total cross section for direct photon production normalized to the $e^+e^- \rightarrow q\overline{q}$ cross section, and Figure 1-8 shows the relative cross section contributions $\sigma^q(q\overline{q}\gamma)/\sigma^{total}(q\overline{q}\gamma)$, $\sigma^e(q\overline{q}\gamma)/\sigma^{total}(q\overline{q}\gamma)$, and $\sigma^{int}(q\overline{q}\gamma)/\sigma^{total}(q\overline{q}\gamma)$ for radiation off quarks, electrons and the interference term. A restriction of the direct photon polar angle to $45° \leq \theta_\gamma \leq 135°$ is made to stay away from the electron and positron beams, and a cut in the thrust (see Equation 5.1 for thrust definition) (thrust < 0.975) is made to keep away from singularities.

Photons from final state radiation and initial state radiation are usually mixed together, because they are both energetic and relatively isolated, *i.e.* far from the hadronic jet axis. Thus an isolated photon analysis is done to study these photons. It is expected that the initial state radiation rate becomes very high when the photon polar angle θ_γ becomes small or when the energy of the photon approaches the beam energy (see Figure 1-5). In order to observe the final state radiation from quark bremsstrahlung, it is necessarily to stay away from these two regions.

As shown in Figure 1-4, the initial state radiation process leaves the final state $q\overline{q}$ system with charge conjugation $C = -1$, and the final state radiation leaves the final state $q\overline{q}$ system in the $C = +1$ state. The interference between the amplitudes of opposite charge conjugation quantum number states is expected to induce a charge asymmmetry in the resultant jets with respect to the incident beam [20]. If the asymmetry is confirmed, in return it provides evidence for the existence of the final state photon radiation.

The forward-backward charge asymmetry of quark jets in the $e^+e^- \rightarrow q\overline{q}\gamma$ process was first calculated by Brodsky *et al.* [20]. Experimental studies have been performed by several groups [21] in the center-of-mass-energy region from 14 GeV to 44 GeV. The observed values for forward-backward charge asymmetry of positive jet with respect to the positron beam

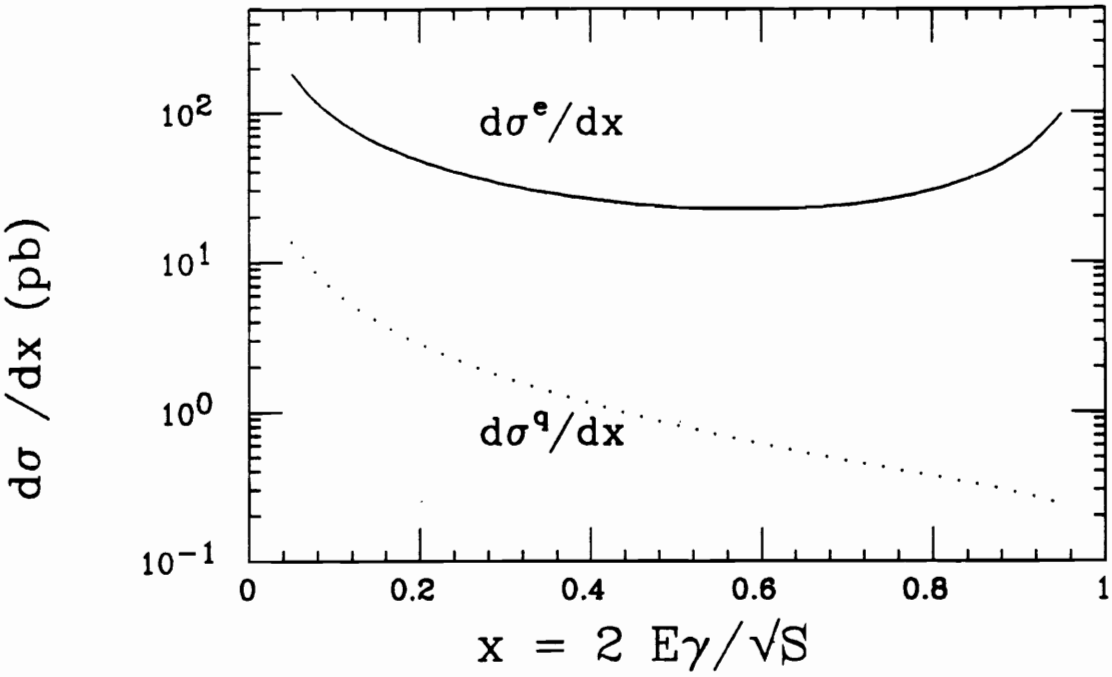

Figure 1-5: Differential cross sections for direct photon productions at $\sqrt{s}$=60 GeV.

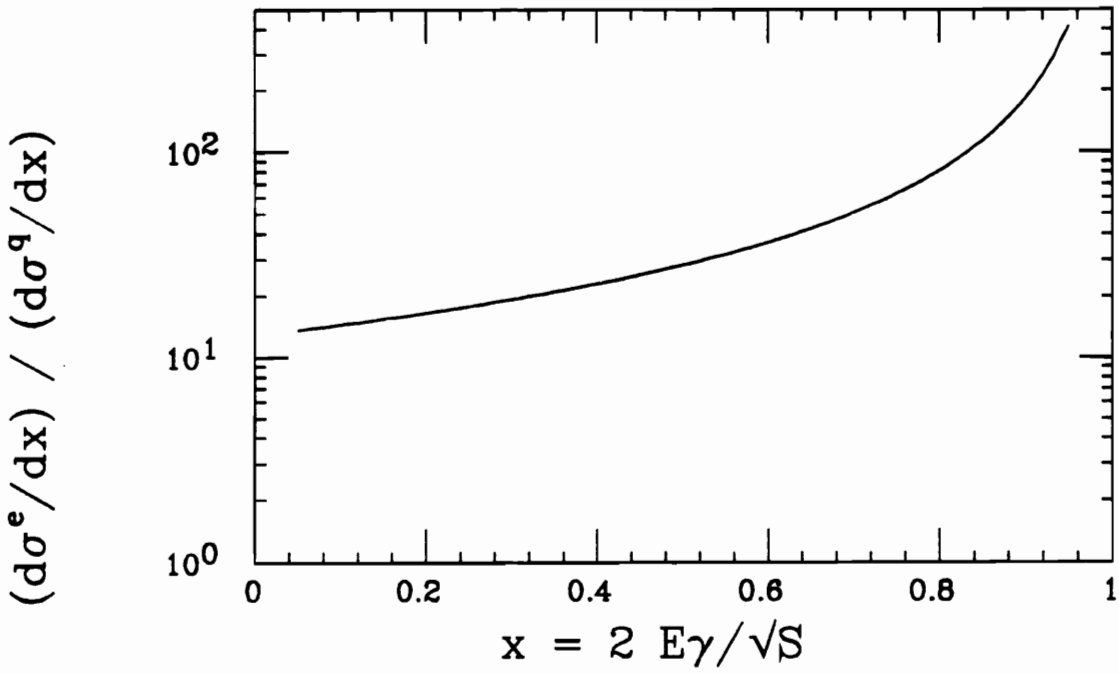

Figure 1-6: Ratio of direct photon production cross sections at $\sqrt{s}$=60 GeV.

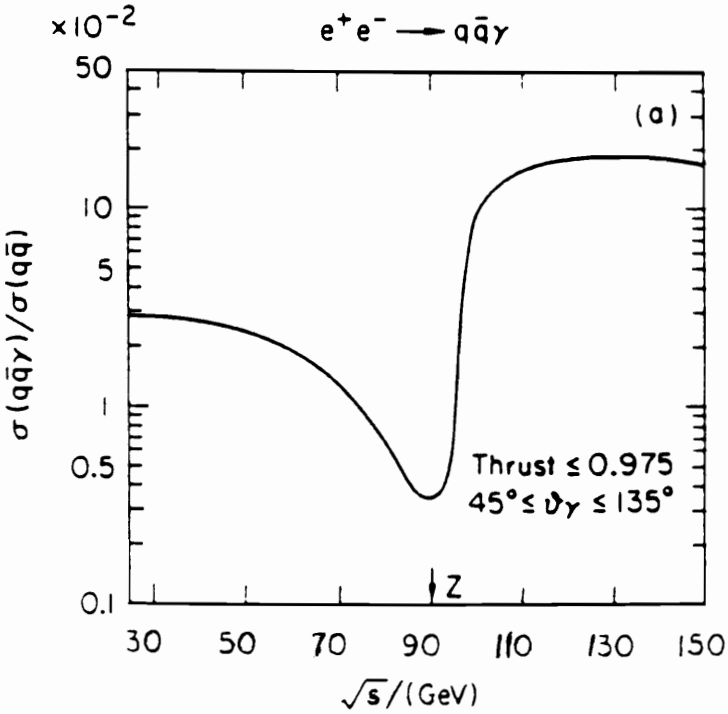

Figure 1-7: Total cross section for direct photon production.

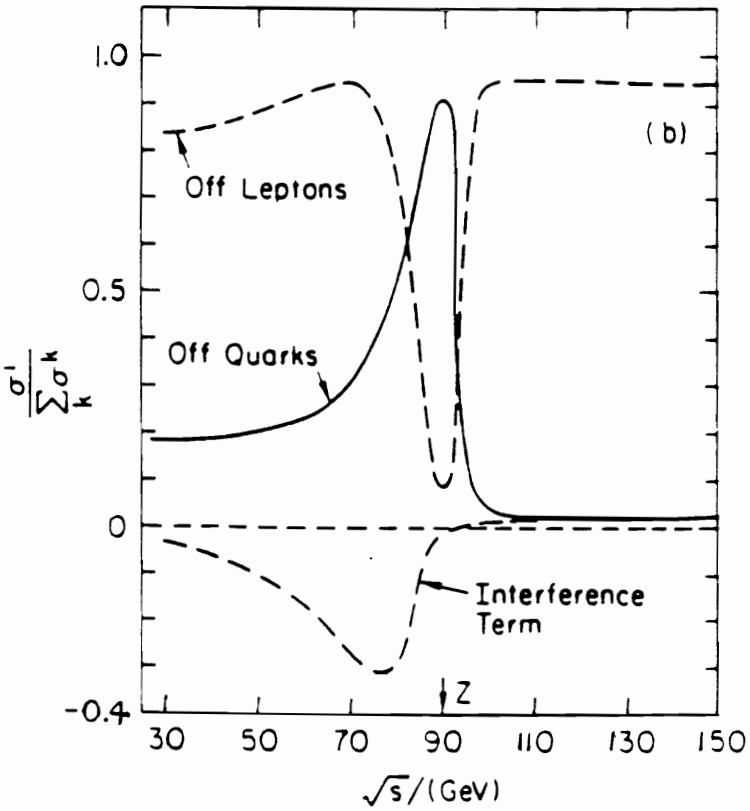

Figure 1-8: Relative cross section contributions for radiation off quarks, electrons and interference term.

direction are given in Table 5-3.

The charge asymmetry analysis of AMY data in the TRISTAN energy region is presented in Chapter 5. Also shown are the comparisons with the results of the other experiments.

1.2.3 Photons from New Particle Production

A process like $e^+e^- \rightarrow H^\circ + \gamma$, where H° is an unknown heavy neutral particle (such as a Higgs particle), could give additional isolated photons. Thus we include this new process search in our isolated photon analysis.

Assuming that the new particle H° is the neutral scalar Higgs particle, there are two different channels for $e^+e^- \rightarrow H^\circ + \gamma$ processes. One is through γ/Z° one-loop coupling [23], the other is via decay of a vector meson V [22] [24], where $V(q\overline{q})$ is a quarkonium bound state of heavy quarks $q = (c, b, t)$. The Feynman diagrams for these processes are shown in Figure 1-9 and Figure 1-10.

In the TRISTAN energy region, $\sqrt{s}$ is not high enough for Higgs to have the W-induced and Z-induced decays, therefore H° decays dominantly into the heaviest possible fermion pairs allowed by kinematics. The partial decay width of Higgs has the form [22] [23]

$$\Gamma(H^\circ \rightarrow f\overline{f}) = c_f \frac{G_F\, m_f^2\, m_{H^\circ}}{4\pi\sqrt{2}} [1 - \frac{4m_f^2}{m_{H^\circ}^2}]^{3/2} \tag{1.7}$$

where m_f and m_{H° are the final state fermion (either lepton or quark) mass and Higgs mass respectively, $c_f = 1$ for leptons and $c_f = 3$ for quarks.

The processes shown in Figure 1-9 and Figure 1-10 have the same final state, and they all have the same distinct signature of an isolated energetic photon with a monochromatic energy recoiling against the rest of the hadronic mass.

Numerous searches for H° have been done by different experimental groups [25] via various H° production channels. The AMY results of new particle H° search via $e^+e^- \rightarrow H^\circ + \gamma$

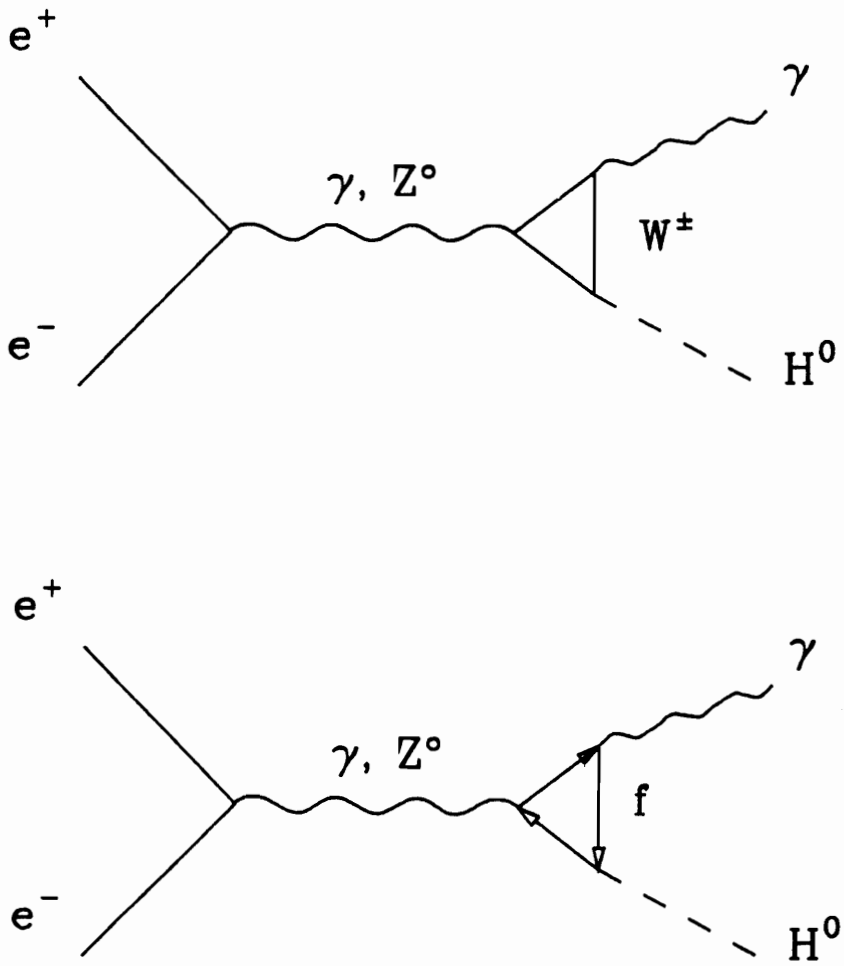

Figure 1-9: $e^+e^- \rightarrow \gamma/Z^\circ \rightarrow H^\circ + \gamma$.

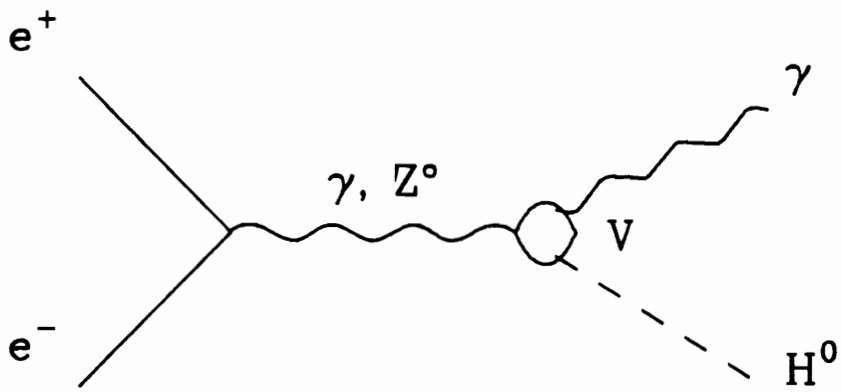

Figure 1-10: $e^+e^- \rightarrow V \rightarrow H^\circ + \gamma$.

are presented in Chapter 5, also shown are the comparisons with the results of the other experiments.

Chapter 2

Colliding Beams and the AMY Detector

2.1 TRISTAN

TRISTAN (Transposable Ring Intersecting STorage Accelerator in Nippon) is a system of particle accelerators which produces, accelerates and collides electron and positron beams. It is located at KEK (National Laboratory for High Energy Physics), in Tsukuba City, Japan. At the time of its initial operation in October 1986, TRISTAN was the highest energy e^+e^-collider in the world.

TRISTAN consists of 4 sections: the positron generator, the electron linear accelerator (LINAC), the accumulation ring (AR), and the main ring (MR) (Figure 2-1). The TRISTAN MR is 3 km in circumference and has 4 intersection regions. Three of the intersection regions contain general purpose detectors, AMY, TOPAZ, and VENUS. In the fourth region a special experiment SHIP is located , which is designed to find highly ionizing particles.

TRISTAN operation is a cyclical process, each cycle consisting of beam injection, acceleration and collision. Initially e^- beam is produced at 30 MeV, and e^+ beam is produced by

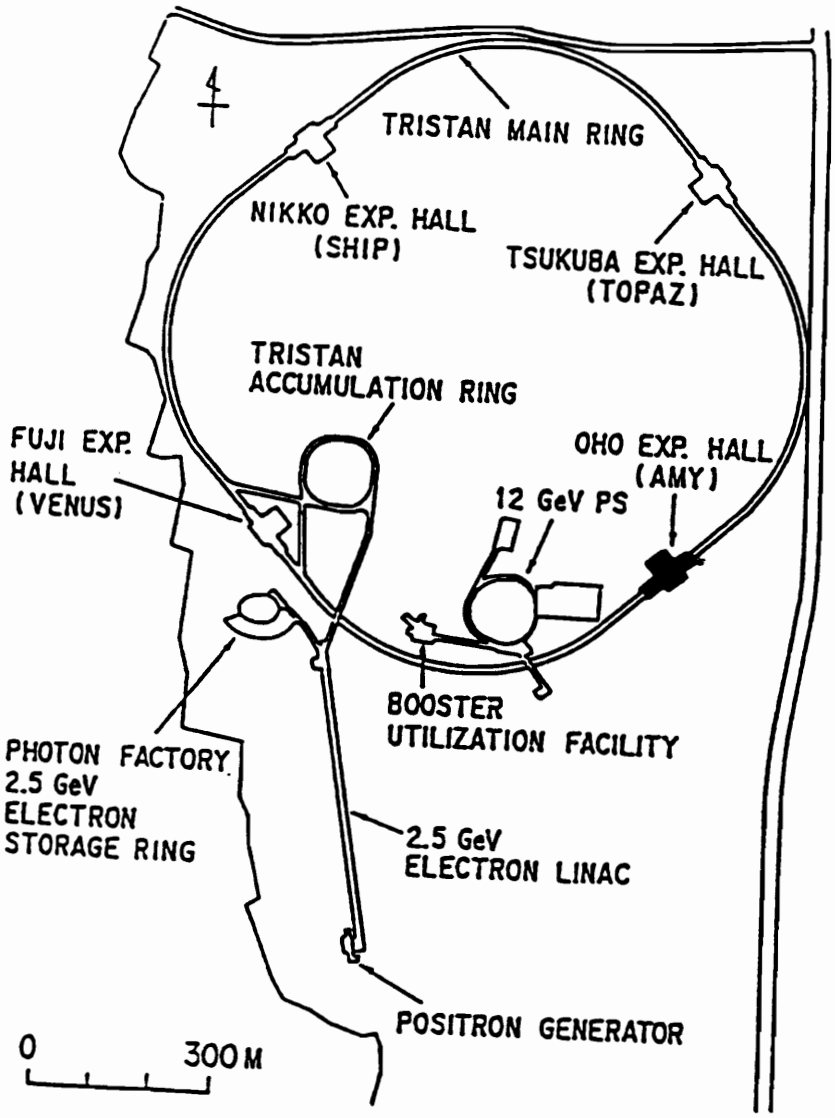

Figure 2-1: Overview of the TRISTAN e^+e^-Collider

bombarding a tantalum target with 200 MeV electrons. Electrons (or positrons) are accelerated to 2.5 GeV in the 400 m long LINAC, and they are further accelerated to 8 GeV in AR, which has a circumference of 377 m. When the accumulating AR beam current reaches 10 mA, the beam is injected into MR. A total of two positron and two electron bunches, each bunch a few cm in length, are stored in MR each cycle, where the electron bunches circulate in one direction and the positron bunches the other. The beams are accelerated to collision energy in MR, and then focused by magnets to collide at the four interaction regions. A typical cycle takes appoximately 1.5 hours, which includes about 1 hour of data taking.

Since the first collision started in November 1986 at $\sqrt{s}$= 50 GeV, $\sqrt{s}$ up to 64 GeV had been achieved by 1990. Total integrated luminosity at each center-of-mass energy is shown in Table 2-1. A total luminosity of 62.5 pb^{-1} was accumulated from November 1986 through July 1990.

2.2 The AMY Detector

The AMY detector, located at the Oho interaction region of TRISTAN, is a general purpose detector. A 3 tesla magnetic field provided by a superconducting solenoidal magnetic coil and overall compactness of the detector provide good lepton identification, high luminosity, and good momentum resolution.

The AMY detector in Figure 2-2 is approximately cylindrical in shape and is made up of several specialized subdetectors. Radially outward from the beam pipe are the Inner Tracking Chamber (ITC) and the Central Drift Chamber (CDC), which measure the momenta of charged particles. The barrel Electromagnetic Shower Counter (SHC), which measures the energies and track positions of photons and electrons, is between the CDC and the superconducting magnetic coil [30]. The magnet's return yoke contains the magnetic field and acts as a hadron filter for the outermost subdetector, the Muon Detector (MUO) [31].

Table 2-1: Integrated luminosity in AMY (Errors are statistical only).

$\sqrt{s}$ (GeV)	$\int \mathcal{L}\, dt$ pb^{-1}
50	0.636 ± 0.016
52	3.976 ± 0.043
54	0.5368 ± 0.017
55	3.266 ± 0.039
56	5.993 ± 0.053
56.5	0.994 ± 0.022
57	4.398 ± 0.046
57.25	0.0582 ± 0.004
57.5	0.0803 ± 0.005
57.75	0.0781 ± 0.005
58	27.234 ± 0.076
58.5	0.801 ± 0.016
58.75	0.0865 ± 0.005
59	0.7206 ± 0.020
59.05	0.504 ± 0.013
59.125	0.0756 ± 0.005
59.25	0.0984 ± 0.006
59.5	0.0724 ± 0.005
60	3.549 ± 0.044
60.8	3.494 ± 0.051
61.4	4.323 ± 0.054
63.6	0.4396 ± 0.0105
64	1.0967 ± 0.0263

Located in the endcap regions are various scintillator and drift tube detectors [32]: the Forward Luminosity Monitor (LUM) which is used to monitor the instantaneous luminosity and beam conditions; the Pole Tip Counter (PTC) which provides the precise measurement of integrated luminosity by counting small angle Bhabha ($e^+e^- \rightarrow e^+e^-$) events; and the Ring Veto Counter (RVC) which tags particles traveling between SHC and PTC.

In the AMY coordinate system the $+z$ direction is defined to be the direction of the e^- beam. The angle θ is measured relative to the z axis. Both ϕ and r are measured in the $x - y$ plane, where the x axis points to the center of curvature of the MR and the angle ϕ is the angle relative to the x axis.

In the following a brief description of several subdetectors, which comprise the basis of this analysis, is given.

2.2.1 The Inner Tracking Chamber (ITC)

Located just outside of the beam pipe, ITC is a small drift chamber used to measure the vertex of charged tracks and give the fast trigger information. The chamber has a total thickness of about 2.0 cm in r , with inner and outer radii of 12.2 cm and 14.2 cm respectively and a total length of 55 cm in the z direction. It consists of four layers of cyclindrical aluminum-coated tubes, with each tube having a radius of 3 mm and a 16 μm-diameter anode wire at 1.7 kV high voltage inside (Figure 2-3). A 50% Ar, 50% C_2H_6 gas mixture, pressurized to 1.48 kg/cm^2, is used to improve spatial resolution. Signals, after passing through preamplfiers and discriminators, are digitized by ADC (Analog to Digit Convertor) and TDC (Time to Digital Convertor).

The position resolution in the r–ϕ plane is approximately 80 μm. No z direction information is obtained.

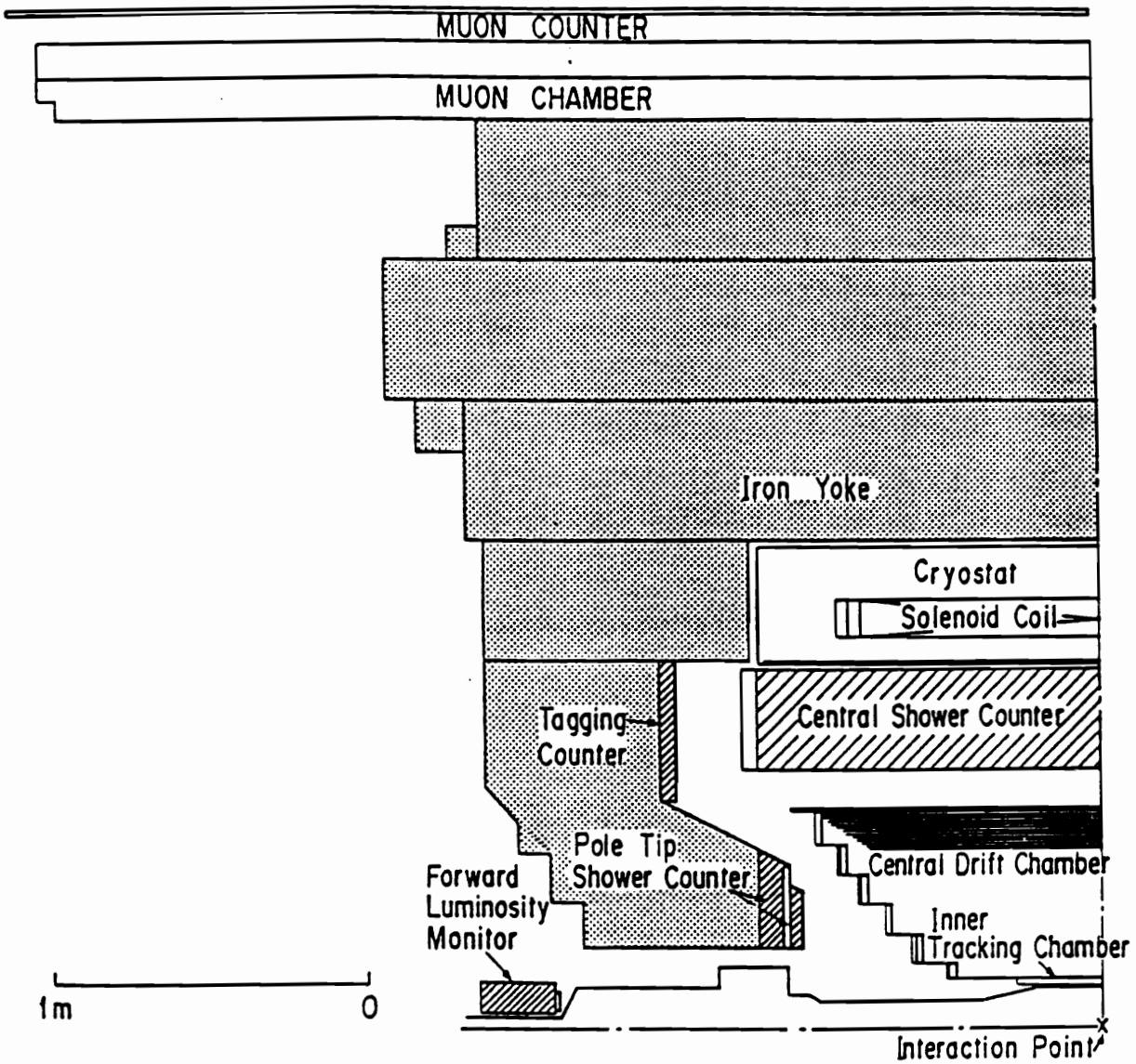

Figure 2-2: The AMY Detector

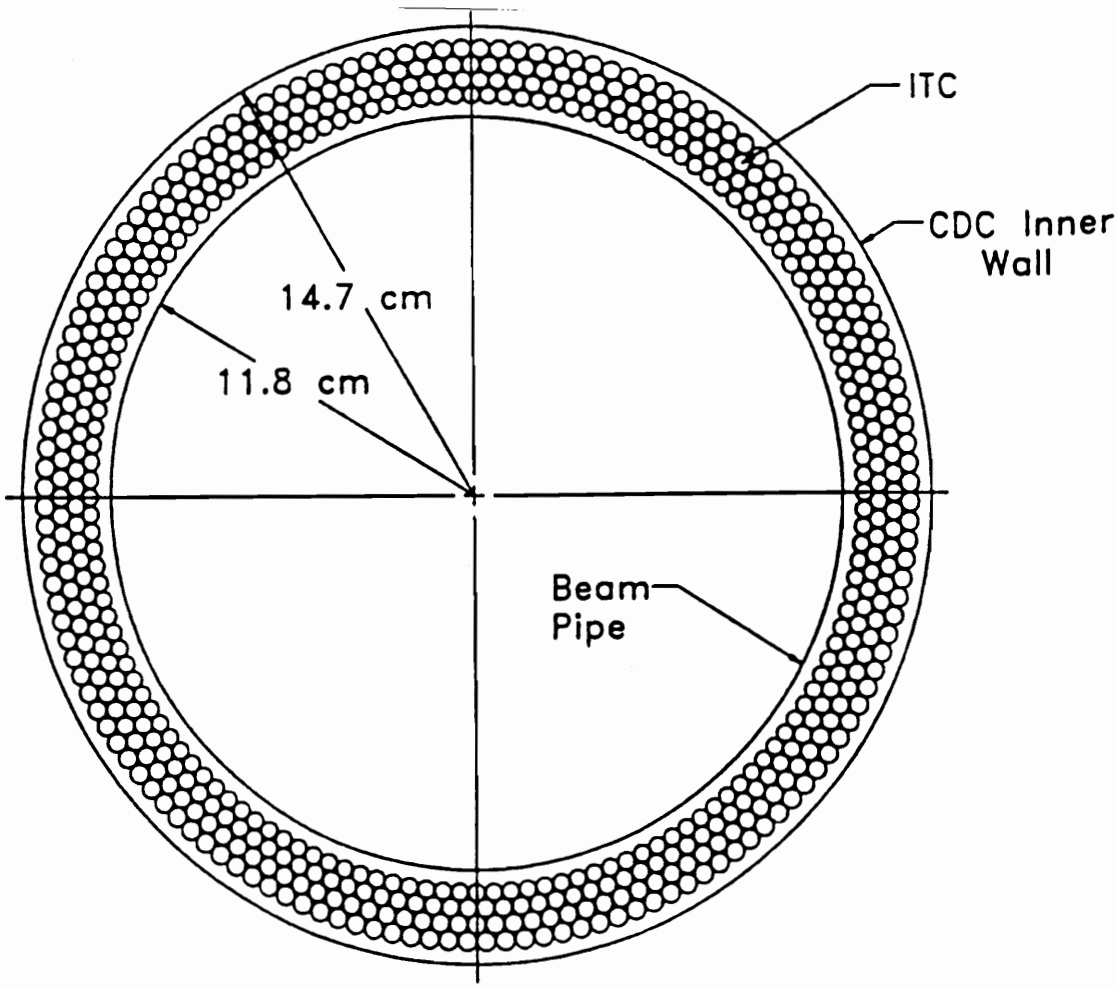

Figure 2-3: The AMY Inner Tracking Chamber

2.2.2 The Central Drift Chamber (CDC)

The CDC is primarily used in charged particle tracking. The momenta of charged particles are calculated by fitting tracks to the expected curvature in the 3 tesla magnetic field. The momentum resolution measured by Bhabha-scattering events is given as $\Delta p_T/p_T \sim 0.7\% \times p_T(GeV/c)^{-1}$, which corresponds to a spatial resolution of 170 μm. Angular resolutions are 0.18° for ϕ and 0.36° for θ.

The CDC, shown in Figure 2-4, consists of 25 axial and 15 stereo layers of anode wires extending from a radius of 16 cm to 65 cm. The CDC provides charged particle tracking in the region defined by $|cos\theta| \leq 0.87$. Axial wires are parallel to the z-axis, providing $r - \phi$ information. Stereo wires are slanted about 5° relative to the z direction, providing small angle stereo measurement of the z-coordinate. Each anode wire (either axial or stereo) is surrounded in a hexagonal pattern by 6 cathode wires, as shown in Figure 2-5. The 20 μm-diameter gold-plated tungsten anode wires are maintained at 1800 V dc, and the 160 μm gold plated aluminum cathode wires are at ground. From 1986 to Spring 1989, HRS gas (89% Ar, 10% CO_2, 1% CH_4) was used in the chamber. Since Spring 1989 the gas was switched to a 50% neon and 50% ethane gas mixture.

The CDC signals go into preamplifier and discriminator circuits, and then go through a time-to-digital fast conversion system, which is read out by the AMY data acquisition system. The CDC track reconstruction is performed by two tracking algorithm programs, ACE and DUET. More details on the CDC tracking algorithm can be found in references [26] [27].

2.2.3 The Barrel Electromagnetic Calorimeter (SHC)

The Barrel Electromagnetic Calorimeter (Shower Counter) [28] is designed to measure the energy of photons and to distinguish electrons from other charged particles. Its main feature

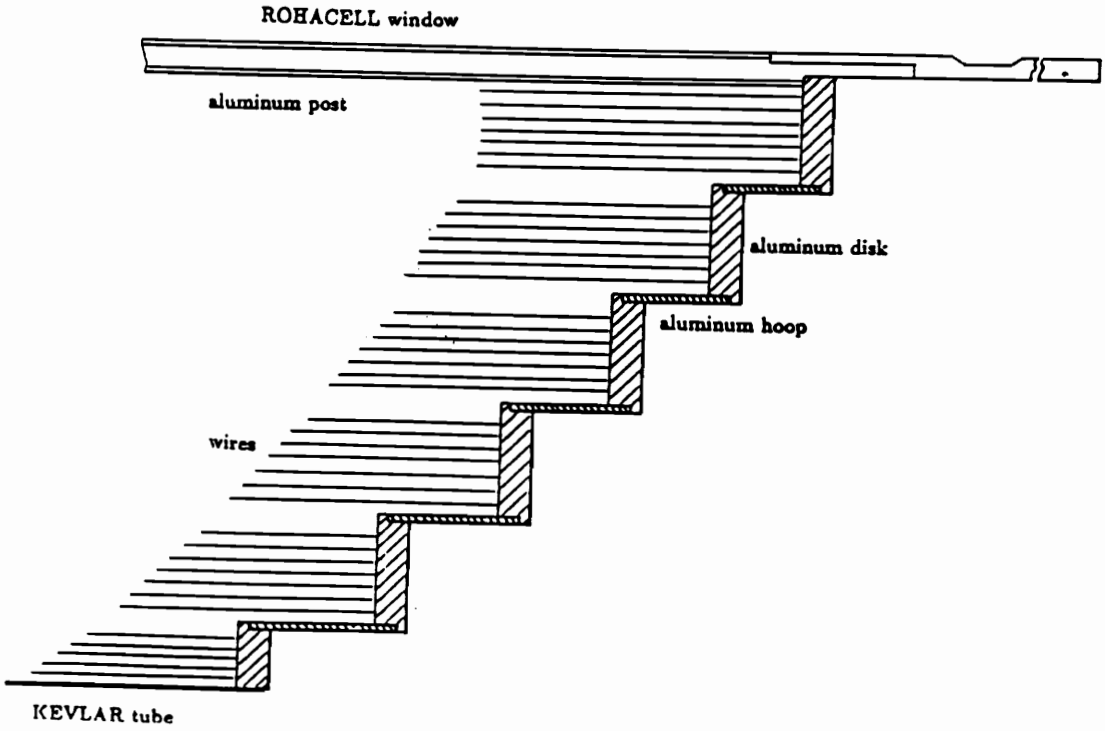

Figure 2-4: The AMY Central Drift Chamber

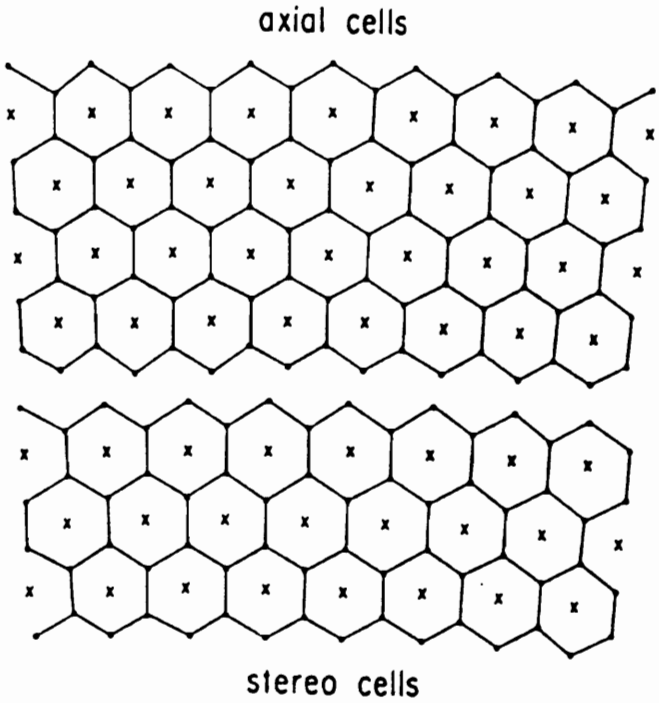

Figure 2-5: Anode pattern of the Central Drift Chamber

is the excellent spatial resolution, provided by the fine segmentation in both the r–ϕ plane and the z direction.

SHC, as shown in Figure 2-6, has a length of 220 cm in the z direction and inner and outer radii of 79 cm and 110 cm respectively. It covers the angular region $|cos\theta| \leq 0.73$. Azimuthally it is divided into six identical, independent subsections, called sextants. Each SHC sextant consists of 20 layers of gas-filled resistive plastic proportional tube planes interspersed with 19 layers of lead sheets, with the first 15 layers of lead sheets having a thickness of 3.5 mm/per-sheet, followed by 4 layers of 7 mm thick lead sheets. The innermost layer has 2.4 mm stainless steel instead of lead. Each sextant has a total of 14.5 radiation lengths given by 20 layers of tubes and lead sheets mentioned above. Figure 2-7 shows a cross section of one layer of the SHC consisting of resistive plastic tubes, gold plated 50 μm-diameter tungsten anode wires, and double sided copper clad G–10 board with cathode strips. The tubes are filled with 49.3% Ar, 49.3% C_2H_6, 1.5% C_2H_5OH gas mixture, except for the 55 GeV data where HRS gas was used. Ionization avalanches within the tubes induce signals on the cathodes, which are read out by strips. The inner radius strips (θ pads) are arranged perpendicular to the z direction, providing θ position information. The outer strips (ϕ pads) are parallel to z, providing ϕ position information. The twenty layers are divided into five cathode gangs of four layers each. The θ and ϕ cathodes, along with the anode signals, are read by the ADC modules. SHC analysis will be described more in Section 3.1.2. Details about SHC calibration can be found in [33].

The energy resolution of SHC [29] is typically $\sigma_E/E \sim 23\%/\sqrt{E} + 7\%$. The angular resolution is $\sigma_\theta \sim 0.3°$ and $\sigma_\phi \sim 0.1°$.

The SHC was damaged by an accident after the Summer of 1988 run. Approximately 20% of anode wires in sextant 1 and 17% of anode wires in sextant 6 were damaged. As a result, the energy resolution for runs after Summer 1988 is typically $\sigma_E/E \sim 36\%/\sqrt{E} + 17\%$. Since this analysis is sensitive to the resolution of SHC, data samples associated with the damaged SHC are not included. During the Summer of 1989, two new sextants were installed to

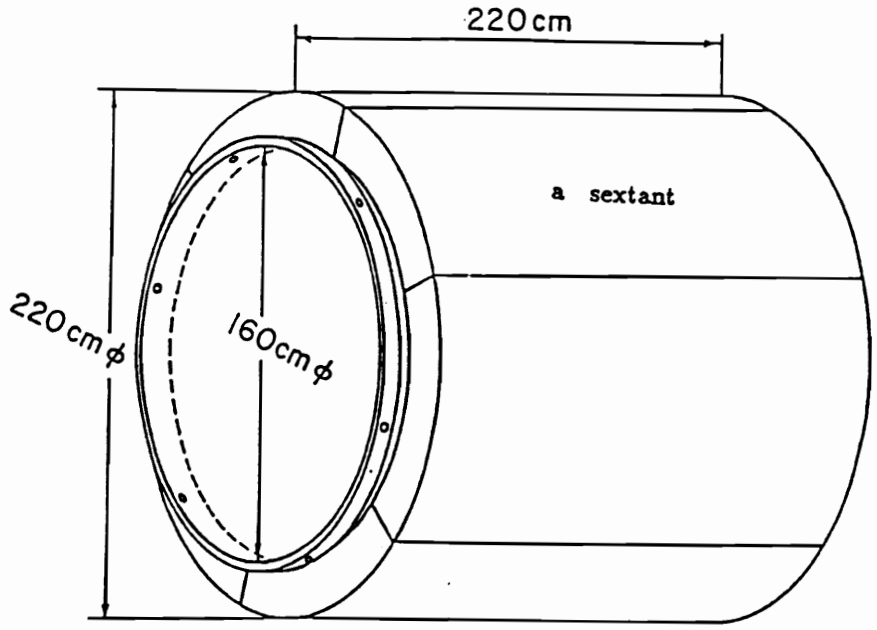

Figure 2-6: The AMY Shower Counter

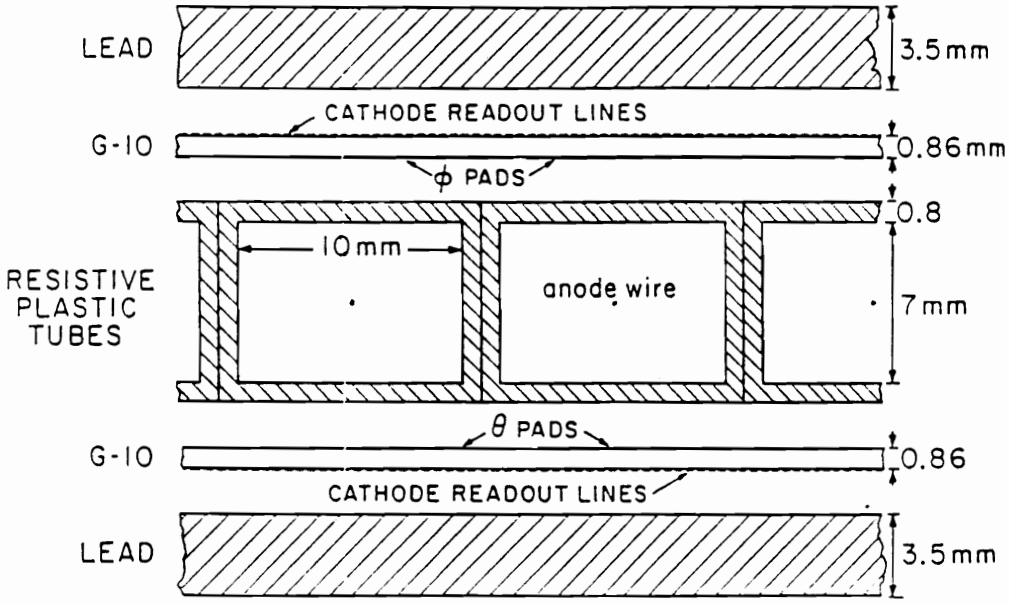

Figure 2-7: The side-view of one layer of SHC

replace the damaged sextants. In addition, some repair was done to the other four sextants. The energy resolution has been recovered to near its original value. This analysis will include the data samples taken before the Summer 1988 accident and after the summer 1989 SHC repair.

2.3 Trigger System

The e^+e^- beam crossing frequency at TRISTAN is about 200 kHz, that is once every 5 μs. However only a small percent of these crossings produce useful physical events, *i.e.* e^+e^- annihilation events. The trigger is used to decide, between the beam crossings, whether or not the last crossing has generated a physical event, and consequently if the event should be stored by the data acquisition system. The trigger rate has to be kept to less than 3 Hz, in order to minimize the deadtime in the AMY data aquisition system. A cosmic ray gate opens between beam crossings. Events triggered within these time intervals provide information on the cosmic ray contamination.

There are two basic types of triggers in AMY. One is the energy triggers, provided by SHC and the endcap detectors, based on total energy and individual cluster energy depositions. The other is the charged track triggers, provided by ITC and CDC, based on finding radial tracks in ITC and/or radial track segments in CDC. For redundancy, the two basic types are divided into 21 separate triggers, as summarized in Table 2-2. Some of the triggers relevant to this analysis include: 1) more than 4 tracks in CDC, 2) SHC energy of more than $\sim$ 3GeV. Because of the large redundancy, the overall trigger efficiency for hadronic events (cuts described in Section 3.3) has been estimated to be greater than 99% [26]. Therefore the trigger inefficiencies have negligible effects on this analysis.

Table 2-2: AMY trigger summary

Trigger bit	Name
5	PTC trigger
8	SHC total energy
10	Cosmic ray
11	RVC + PTC rear inclusive
13	ITC 2 track + CDC + SHC minimum ionizing particle
14	ITC 2 track back to back + CDC
15	ITC 2 track + CDC + SHC low majority 1
16	ITC multi track
17	CDC multi track
18	CDC losser multi track + SHC minimum ionizing particle
19	(SHC high majority 1 + SHC low majority 2)
	or (SHC high majority 3)
20	(SHC low majority 2 or SHC majority 1)
	+ CDC + not(Trigger 19)
21	ITC + CDC 2 track
22	CDC 3 or 4 track
23	ITC 2 track + Muon hit
24	ITC 2 track + CDC + SHC minimum ionizing particle
26	CDC + RVC dimuon trigger
27	ITC + RVC dimuon trigger
28	ITC 2 track + CDC + RVC
30	CDC perfect 2 track
31	CDC perfect 1 track, bachelor V

2.4 Data Acquisition System

The AMY data acquisition system is shown in Figure 2-8. The data flow is from AMY detectors → FASTBUS/CAMAC systems → VAX computer → FACOM computer.

A VAX 11/780 computer is used to control a FASTBUS data acquisition system. All the signals from various subdetectors are digitized and read out by the FASTBUS system.

The VAX also controls a CAMAC system, which obtains information from various monitors, such as high voltage, temperature, pressure, SHC gas gain, and trigger monitors.

The VAX temporarily stores the data, and also does some fast analysis of the data to assure all the subdetectors are working normally. Then the data are sent to a FUJITSU/FACOM mainframe computer through an optical link. Final data filtering and analysis are done on FACOM. Eventually the data are moved to a cassette-tape library for long term storage. Analysis is also performed on U.S. based VAX computers, with data being transferred by magnetic tapes from KEK.

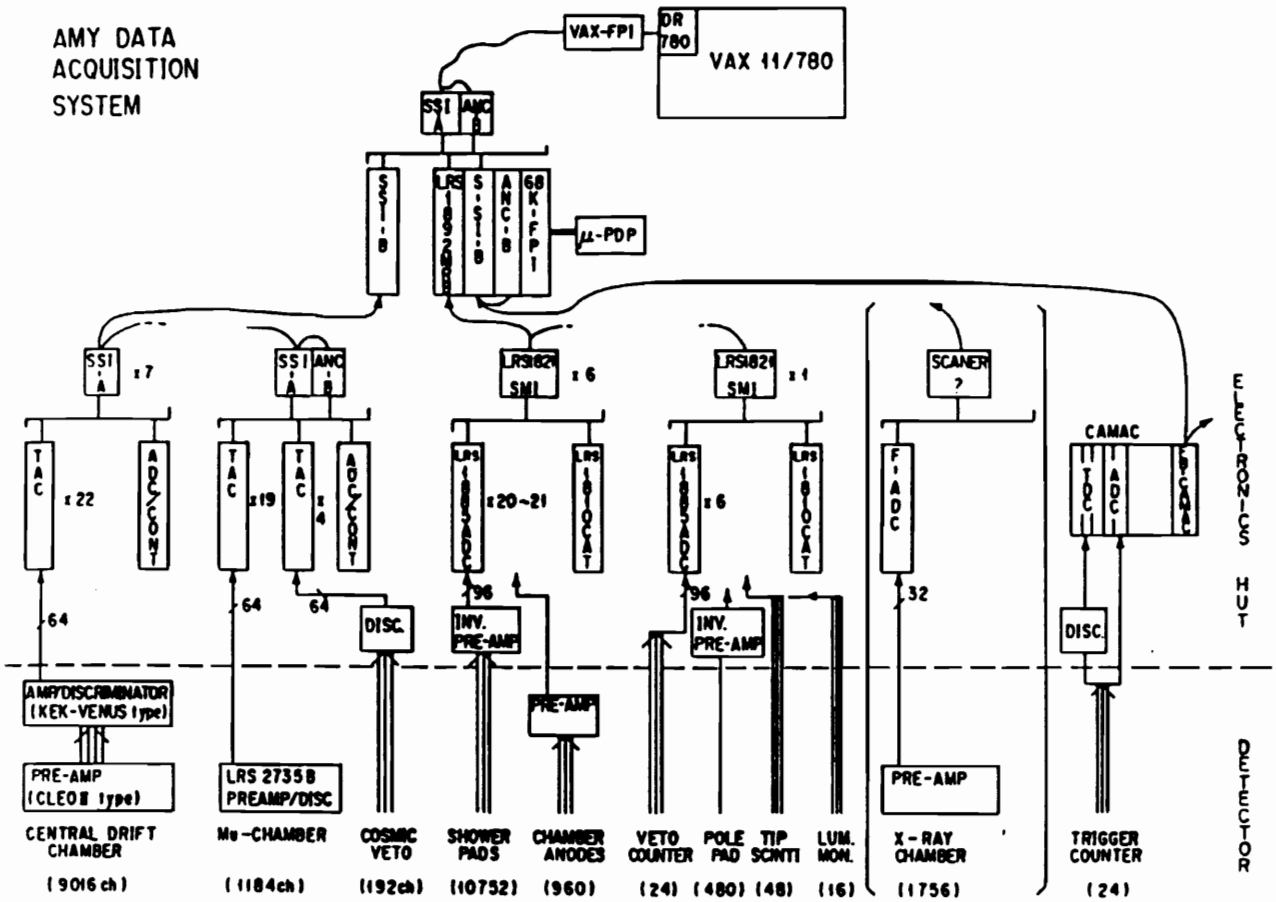

Figure 2-8: AMY data acquisition system

Chapter 3

Offline Analysis and Monte Carlo Techniques

3.1 Offline Analysis

Several offline analyses are run on the raw data to derive the 3-momenta of the particles from the individual subdetector signals. Among them, the CDC analysis and SHC analysis are directly related to the analysis presented in this thesis. A brief description is in the following sections.

3.1.1 CDC analysis

A charged particle moving through the CDC follows an approximately helical path because of the 3 tesla solenoidal magnetic field in the region. The 3-momentum of a charged particle can be derived from the curvature of the track and its inclination angle. Two offline programs, ACE [26] and DUET [27], are used to fit the patterns of hit wires in CDC to helices.

ACE is a program which provides fast reconstruction of tracks, designed according to the particular geometry of the AMY CDC: ACE algorithm is based on the assumption that a track is a circle passing through the origin, and that all the track hit sections belonging to the same track should have the same curvature and azimuthal production angle. Usually it takes ACE less than 20 msec to process one track in a typical multi-hadronic event on FACOM M–382 computer.

DUET is designed to do a more elaborate track reconstruction. It contains a routine which takes into account the effect of the non-uniformity of magnetic field on the particle's trajectory. For the purpose of further improving the momentum resolution, it has an option to include the ITC information in the track fitting. However at the price of providing higher quality tracking, DUET is about 50 times slower than ACE. Therefore DUET is only used on the events which are pre-selected on a basis of ACE results.

The momentum resolution and angular resolution of CDC are described in Section 2.2.2. More details on charged particle tracking can be found in reference [26].

3.1.2 SHC analysis

The SHC raw data undergo many corrections before the energy of a showering particle can be determined.

1. The gain change due to variations of high voltage (HV) on anode wires is corrected for. There are 20 HV lines for each sextant, one for each layer with the same HV being applied to anode wires except for the layers which have discharge or instability problems. The following correction factor is used for low HV layers:

$$HV\ correction\ =\ g^{\alpha}$$

$$\alpha\ =\ (supplied\ HV\ -\ standard\ HV)/100$$

where g is a gain drop factor per 100 voltage drop. The gain factor is determined to be 2.3 from a test beam experiment.

2. The gain change due to variations of gas composition, pressure, and temperature is corrected for. We use monitor tubes to monitor the gain change due to the gas condition. Four tubes containing ^{55}Fe sources are placed within the SHC gas volume at various locations in each sextant. The average gain is determined from at least 2 good tubes per sextant. This monitor tube information is read every 15 minutes during data taking and is analyzed before we start any other analysis.

3. Corrections are made for loss of signals due to dead cathode channels. Some of the cathode channels have a very low or zero gain because of HV problems, disconnected signal cables or dead ADC channels, *etc.* Approximately 1% of all cathode channels are found to be dead from the analysis of Bhabha events. Data of these channels are linearly interpolated from their nearest neighbors. This method also is used to correct noisy channels which constantly give high ADC counts during certain periods.

4. Since the ganged layer 5 has twice as much radiation length of material as the other layers, the signal size from layer 5 is multiplied by a factor of 2.

After the above corrections, the signals are formed into "clusters" using a cluster-finding algorithm [29] as described below. The anode wires in each layer are grouped into 48 towers. The anode signals from individual towers are used for SHC triggers. The cathode in each layer is segmented in θ and ϕ into 48 sections, 4 divisions in θ and 12 in ϕ. The cathode strips are grouped into 5 gangs of 4 layers each. We call them ganged layers. The strip signals (both θ and ϕ) from each section in each ganged layer is read out by ADC, giving information about the cluster in all 5 ganged layers in both θ and ϕ directions (Figure 3-1). Shower clusters are formed as follows:

1. Within each gang of each SHC section the signals are grouped into hits: the strip with maximum ADC counts is assigned as the center of a hit, the hit is formed by adding

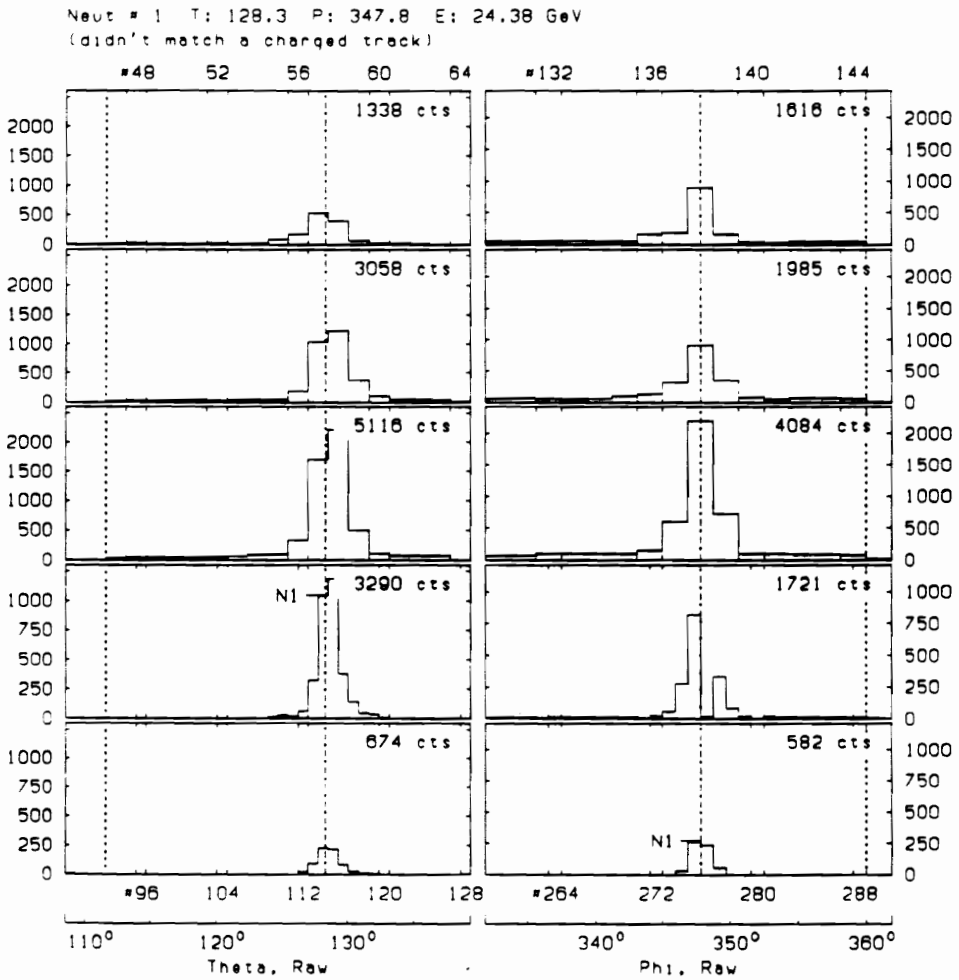

Figure 3-1: SHC cathode cluster development. Numbers in the horizontal axis are strip numbers and those in the vertical axis are ADC counts.

counts from the strips which lie within ± 3 strips from the center.

2. The hits in θ for a given gang are matched by position to θ hits in the other four gangs. Similar matching is done to ϕ hits.

3. Hits in θ and ϕ are matched into clusters by comparing counts summed over the five ganged layers. Real clusters have their counts roughly equally distributed between the θ and ϕ strips. When there are too many hits in one ϕ or θ section to unambiguously determine the individual energies of the clusters, the cluster-finding algorithm reverts to summing all of the energy in the section into a single value and locating the cluster at the section center. A "complicated cluster flag" for the entire group is set.

4. After clusters in each section have been defined, clusters overlapping section boundaries are merged together.

5. The θ and ϕ counts for a given cluster is summed for each ganged layer. This provides longitudinal information on the shower development through the SHC. ADC counts summed over all 5 ganged layers gives the total energy of the cluster by using the following procedure.

The energy of the ADC counts of a shower cluster is calibrated with a well known process, Bhabha scattering $e^+e^- \rightarrow e^+e^-$.

1. Leakage correction. Leakage of energy out to the back of SHC due to the limited longitudinal coverage of the calorimeter is estimated by EGS4 simulation [42]. In the case of a 30 GeV electron, energy leakage at the back of SHC is about 15% in the central region and 4% at the edge of the SHC. The energy leakage decreases as the incident energy decreases. For example, a 1 GeV electron has about 3% leakage in the central region of the SHC. The energy leakage factor for photons is larger than that for electrons because of the later shower development.

2. Geometrical correction in ϕ and θ. The leakage-corrected ADC counts of individual electrons or photons may not be uniform as a function of θ and ϕ, because of different thickness of material between the cathode plane and the plastic tube. To correct the energy in ϕ direction with Bhabha events, the ϕ angle is divided into 48 towers and the average energy of each tower is forced to be the expected average Bhabha electron energy, thus obtaining a calibration constant for ADC counts $\rightarrow$ energy for each ϕ tower. The distribution in θ direction is calibrated using the same method.

3. Gain saturation effect. Although the shower counter is designed to operate in the proportional mode, a gain saturation is observed both during test beam and when data are taken. In order to evaluate the saturation more quantitatively, the following second order polynomial fitting function has been used:

$$E_m = \alpha E - \beta E^2$$

where E_m is the measured energy, E is the true energy and parameters α and β have to be determined by experiment. The definition of saturation is

$$C_{sat}(\%) = 100\, E \frac{\beta}{\alpha}$$

The saturation is determined by Bhabha events and acollinear e^+e^- events for different center-of-mass energy runs. In case of acollinear e^+e^- events, we assume that the CDC momentum of the electron or positron is correct and use that as the true energy E. For example, the saturation is determined to be 18% for $\sqrt{s} = 56$ GeV data.

4. Noisy clusters caused by the discharging wires are identified and rejected by using the following criteria:

   - Total energy of the cluster is greater than 1.0 GeV.
   - Energy deposition for one of 5 cathode layers E_{max} is more than 80% of the total energy deposition, and more than 80% of E_{max} is deposited to one anode out of four anode layers in this particular cathode layer.

The current energy and angular resolutions of SHC are given in Section 2.2.3. More details about SHC calibration and the clustering algorithm can be found in references [29] [33].

3.2 Monte Carlo Techniques

The e^+e^- annihilation events are complicated, consisting of many particles in the final states. The AMY detector is also a complex imperfect system. Therefore, it is almost impossible to find a simple analytic method to analyse the properties of e^+e^- annihilation events as they would be observed by the AMY detector and to compute the effects of the acceptance, resolution, and efficiency of the detector. Instead, Monte Carlo(MC) techniques are used to estimate the detection efficiency and the response of the AMY detector to hadronic events and various background processes. By using this technique, we try to simulate as closely as possible what actually occurs, on an event by event basis, in the AMY detector when e^+e^-beams collide. There are two steps in this process:

1. Monte Carlo generation. This step re-produces particle physics in an e^+e^- annihilation event. It includes the production and fragmentation of partons, with the energies and directions of the partons randomly selected according to a probability function derived from QCD, and the decay of short-lived particles produced in the fragmentation process. Finally only electrons, photons, neutrinos, muons and reasonably long-lived hadrons (π^{+-}, K^{+-}, K_L, p, n, Λ°, ...) remain.

2. Monte Carlo simulation. This step simulates the responses of the AMY detector to the particles generated in the previous step, formatting the results in the same way as the actual experimental data, so that they can be analysed by the same offline analysis program.

3.2.1 Monte Carlo Generation

Two types of e^+e^- annihilation events are of special interest to this analysis, the hadronic events $e^+e^- \rightarrow \gamma/Z^\circ \rightarrow$ *hadrons*, and the Higgs-γ events $e^+e^- \rightarrow H^\circ + \gamma$. Therefore events of these types are generated by the Monte Carlo generators described in the following sections.

LUND Monte Carlo Generator

In this thesis, the hadronic five-flavor events are generated by the Lund Monte Carlo program Jetset version 7.2 [11] [12] (we will call it Lund 7.2 from now on).

Initially $q\,\overline{q}$, $\gamma\,q\,\overline{q}$, $q\,\overline{q}\,g$ and $\gamma\,q\,\overline{q}\,g$ events are generated. The gluon bremsstrahlung events are created from $q\,\overline{q}$ events using the parton shower model [11] [34]. Initial state radiation is included using the formalism of Behrends and Kleiss [6], and final state radiation (quark bremsstrahlung) is also included using Sjostrand's machinery [35] [36] [12]. The interference between initial and final state radiation is not included in this model. After the production of the initial partons, they are hadronized using the Lund string fragmentation model [10].

The Lund Monte Carlo has been shown to agree well with e^+e^- collider data at PEP [37], PETRA [38], and TRISTAN [39]. One exception is that the machinery for the final state radiation is possibly not advanced enough [36], the program gives about 15% fewer photons than observed experimently in all three experiments at LEP.

FKS Monte Carlo Generator

The FKS Monte Carlo generator [7] also generates hadronic 5-flavor events, including only the lowest order QCD corrections, and the full electro-weak corrections to the order of α^3.

Initially $q\overline{q}$, $q\overline{q}\gamma$, $q\overline{q}g$ are generated. Both initial and final state radiation corrections are included, as well as the interference term between initial and final state radiation. The gluon bremsstrahlung events are created from $q\overline{q}$ events using the parton shower model [11] [34], just as in Lund 7.2. Also, the initial partons are hadronized using the Lund string fragmentation model [10].

Monte Carlo events generated by the FKS generator are used only in the forward-backward charge asymmetry analysis in this thesis.

EPOCS Monte Carlo Generator

EPOCS [40] (Electron Positron Collision Simulator) is a Monte Carlo event generator designed to model e^+e^- annihilation events at center-of-mass energies below W^+W^- production, *i.e.* in the energy region of TRISTAN and LEP. It generates each event based on the standard model, QCD and electro-weak theory through the following two stages. In the first stage it generates partons according to the matrix element calculated by the perturbative QCD and the electro-weak theory. It may generate a quarkonium state if the beam energy is appropriate to produce it. In the second stage, partons are hadronized using either the independent fragmentation model [13] or the string fragmentation model (similar to that used in the Lund Model). Then unstable hadrons decay according to the particle data table [41].

The $e^+e^- \rightarrow H^\circ + \gamma$ events used in this analysis are generated by the EPOCS Monte Carlo generator, because EPOCS has enough flexibility to easily incorporate the production and decay of new particles, *i.e.* the Higgs particle in this case. The program uses the process $e^+e^- \rightarrow V \rightarrow H^\circ\gamma$ (see Figure 1-10) to generate the events.

3.2.2 Monte Carlo Simulation

The Monte Carlo simulation program models the interactions and decays of the particles generated by the event generator, and the response of the various detector components to the passages of charged and neutral particles. It "swims" each particle through the different parts of the AMY detector in small steps. At each step the particle is allowed to decay or undergo interactions according to the known probabilities. A charged particle loses its energy through ionization processes in material and may change its direction because of multiple Coulomb scattering. Its trajectory is bent as it moves under the influence of the magnetic field. Electrons can emit bremsstrahlung photons; photons may convert into an e^+e^- pair in material; hadrons may undergo nuclear interactions. All these processes are modeled in the simulation.

Electromagnetic showers initiated by photons and electrons inside the SHC and PTC are modeled by the electromagnetic simulation program EGS4 [42]. Hadronic interactions within the iron yoke are modeled by the hadronic simulation program GRANT [43].

All the detector signals thus obtained are formatted in the same way as the raw experimental data, and are subjected to the same offline analysis programs that analyze the experimental data.

Table 3-1 gives the number of simulated Monte Carlo events of each type used in this thesis, where $H^\circ\,\gamma$ events and Lund 7.2 events are fully simulated, and FKS Model events are partially simulated. Partial simulation means that only the events which contain the information directly related to my analysis are simulated, since simulation is very time consuming (simulating a hadronic event takes about 270 seconds of VAX 3100 CPU time on average).

Table 3-1: Simulated $H^\circ\gamma$ MC, LUND MC and FKS MC events

Event type	$\sqrt{s}$ (GeV)	Higgs mass (GeV)	number of events
$e^+e^- \rightarrow H^\circ\gamma$	56	15	1000
	56	25	1000
	56	30	1000
	56	40	1000
	56	50	1000
LUND 7.2	57	–	39164
FKS Model	56	–	80000

3.3 Hadronic Event Selection and the Data Sample

The data used for this analysis were taken at $\sqrt{s}$= 55 to 58 GeV, as listed in Table 3-2. The complete data samples accumulated in AMY are shown in Table 2-1. Because this analysis is relatively sensitive to the energy resolution of the shower clusters, data samples taken with the damaged shower counter are disregarded, as mentioned in Section 2.2.3. Also, because the SHC energy calibration [29] [33] depends on the size of the data samples (see Section 3.1.2), the larger data samples have their SHC energy calibrated more accurately than the smaller ones. Thus the smaller size data samples are disregarded as well. A total luminosity of 40.8 pb^{-1} is used in this thesis.

The raw AMY data contains many different types of events. After applying the offline analysis, according to specific physics interest the data are divided into several non-mutually-exclusive files, such as low multiplicity events ($e^+e^- \rightarrow e^+e^-$, $\mu^+\mu^-$, $\tau^+\tau^-$), QED events ($e^+e^- \rightarrow e^+e^-$, $\gamma\gamma$), and hadronic events, *etc.* Of interest to this analysis are the hadronic event files, which consist of $e^+e^- \rightarrow \gamma/Z^\circ \rightarrow$ *hadrons*. A series of cuts are used to select hadronic events [26]:

- Number of good CDC tracks is greater than or equal to 5.
- The visible energy E_{vis}, defined as the sum of energies of all good CDC tracks and good SHC clusters, is greater than or equal to $\sqrt{s}/2$.
- The momentum imbalance, defined as the sum of the z-components of the three-momenta of all good CDC tracks and good SHC clusters, is less than or equal to 0.4 E_{vis}.
- Total SHC energy E_{shc}, defined as the sum of all good SHC cluster energies, is greater than or equal to 5 GeV.

Radiative Bhabha events $e^+e^- \rightarrow e^+e^-\gamma$ and $e^+e^- \rightarrow \tau^+\tau^-$ events, which only rarely have a charged multiplicity higher than 4, are effectively eliminated by the first cut above. The

Table 3-2: Data samples used in this analysis (Errors are statistical only).

$\sqrt{s}$ (GeV)	$\int \mathcal{L}\, dt$ (pb^{-1})	# of hadronic events
55	3.266 ± 0.039	365
56	5.993 ± 0.053	708
57	4.398 ± 0.046	478
58	27.156 ± 0.076	2709
Total	40.813 ± 0.110	4260

second cut rejects almost all beampipe-wall and beam-gas events (because for those, the total energy cannot exceed $\sqrt{s}/2$), and most of the $\tau^+\tau^-$ and two-photon events. The third cut ensures that there is no large energy leakage into the beam direction, eliminating those events with high-energy initial-state radiation photons near the beam direction, and further removes two-photon events.

The detailed definition of the good CDC track and good SHC cluster can be found in reference [26]. Basically a good CDC track will meet the following requirements:

- At least 8 axial and 5 stereo hits which could be well fitted to a helix.
- Each track is required to originate in a cylindrical fiducial volume, centered on the interaction point, with a 5 cm radius in the $r - \phi$ plane, and a length of 30 cm along the z direction.
- Acceptance cut of $|cos\theta| < 0.85$, to ensure that high momentum tracks traversed all 40 CDC layers.
- The momentum of each charged track is required to be greater than 0.2 GeV/c.
- The fit quality of each reconstructed charged track is required to be $\chi^2 \leq 8$ in the $r - \phi$ plane and $\chi^2 \leq 6$ in the z direction.

A good SHC cluster is required to have energy greater than 0.2 GeV, since below this value there are many noise clusters. Also no more than 95% of its energy should be deposited in any one of the five longitudinal layers of the SHC, because this is the sign that this cluster is caused by SHC electronic noise. In order to avoid double counting of a charged particle by the CDC and the SHC, a SHC cluster with energy below 1 GeV is also excluded if its position matches with a CDC track within 2°.

Events that pass the above hadronic event selection cuts are then eye-scanned by physicists. A very small number of obvious cosmic-ray, beam-gas, and radiative-Bhabha events are

removed from the file (less than 2% of the events are removed). The numbers of hadronic events selected by using these cuts for different center-of-mass energies are listed in Table 3-2. Using Monte Carlo methods, we have found that about two-thirds of Lund five-flavor events pass the above hadronic event selection cuts.

It should be assumed that for the rest of the thesis, these hadronic event selection cuts are applied to both the experimental data and Monte Carlo data before anything further is done.

Chapter 4

Inclusive Photon Analysis

This chapter describes details of the inclusive photon analysis. Even with all the corrections made in the SHC offline analysis mentioned in Section 3.1.2, and all the cuts applied according to the good SHC cluster definition in Section 3.3, many "fake" clusters still survive and remain in the hadronic event samples we use. So the first step of inclusive photon analysis is to find a series of cuts, in order to get rid of the "fake" clusters and keep the "good" clusters. Then Monte Carlo techniques (hadronic event generation and detector simulation) are used to establish the detector efficiency for "good" clusters. Using this result we convert the experimental inclusive photon spectra into the scaled differential cross sections for inclusive photon production. After that, the scaled cross sections are compared with those due to the known photon sources (*i.e.* the conventional sources of photons in hadronic final states we mentioned in Section 1.2), obtained with the simulation results using the five-flavor LUND Monte Carlo. Finally these cross sections are compared with the result of other experiments and also are examined to establish the existence of the final state radiation.

4.1 The "Good" Shower Clusters

The "good" shower clusters are the clusters which actually correspond to the electromagnetic showers caused by neutral particles incident upon the shower counter. An example of a "good" shower cluster initiated by a photon is shown in Figure 4-1, where the numbers in the horizontal axis are strip numbers (also θ and ϕ angles), and those in the vertical axis are ADC counts. As can be seen from this figure, the shower starts in layer 1, then gradually develops through the rest of the layers as it becomes more widely spread. Also shown in this figure is that the center of the shower in each layer follows a straight radial line; this is because a neutral particle does not change its direction when moving in the electromagnetic field. The same thing is not true for the shower caused by a charged particle, as shown in Figure 4-2: we notice that the center of the shower (labeled as N12) in each layer follows the bent path of the charged particle (labeled as C2) under the influence of the magnetic field.

Only the photon shower clusters are of concern to the inclusive photon analysis. Because of the limited position resolution of SHC, photons very close in both θ and ϕ directions could be combined together into one cluster. Since there is no way to tell them from the single photon clusters, and they do correspond to the physical photons, we treat them as good photon clusters in our analysis. There are mainly three types of misidentified photons:

1. "Ghost" clusters, *i.e.* clusters which do not correspond to any neutral particles.
2. Clusters induced by neutral hadrons, such as n and K_L°, which interact in the material of SHC and are misidentified as photons.
3. Clusters caused by charged tracks which are badly reconstructed in CDC and fail to extrapolate to the corresponding cluster in SHC.

In contrary to "good" shower clusters, "ghost" clusters do not have the shape associated

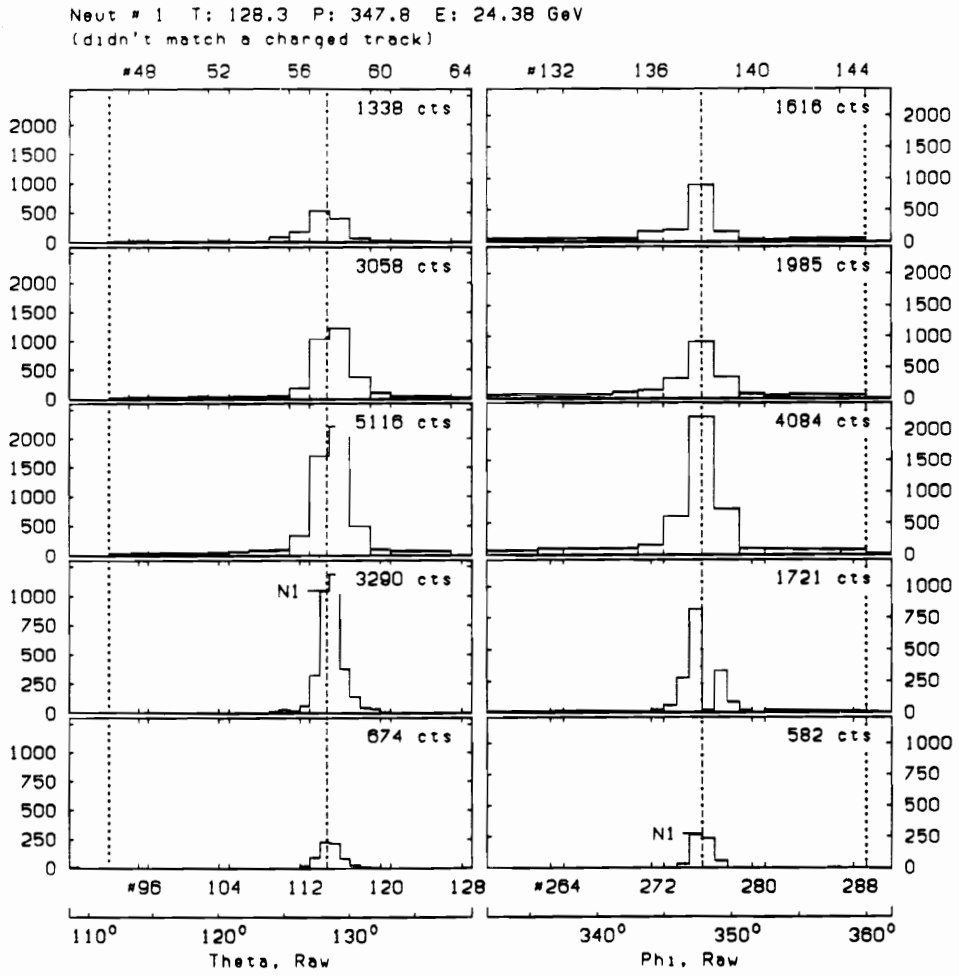

Figure 4-1: Example of a shower initiated by a photon.

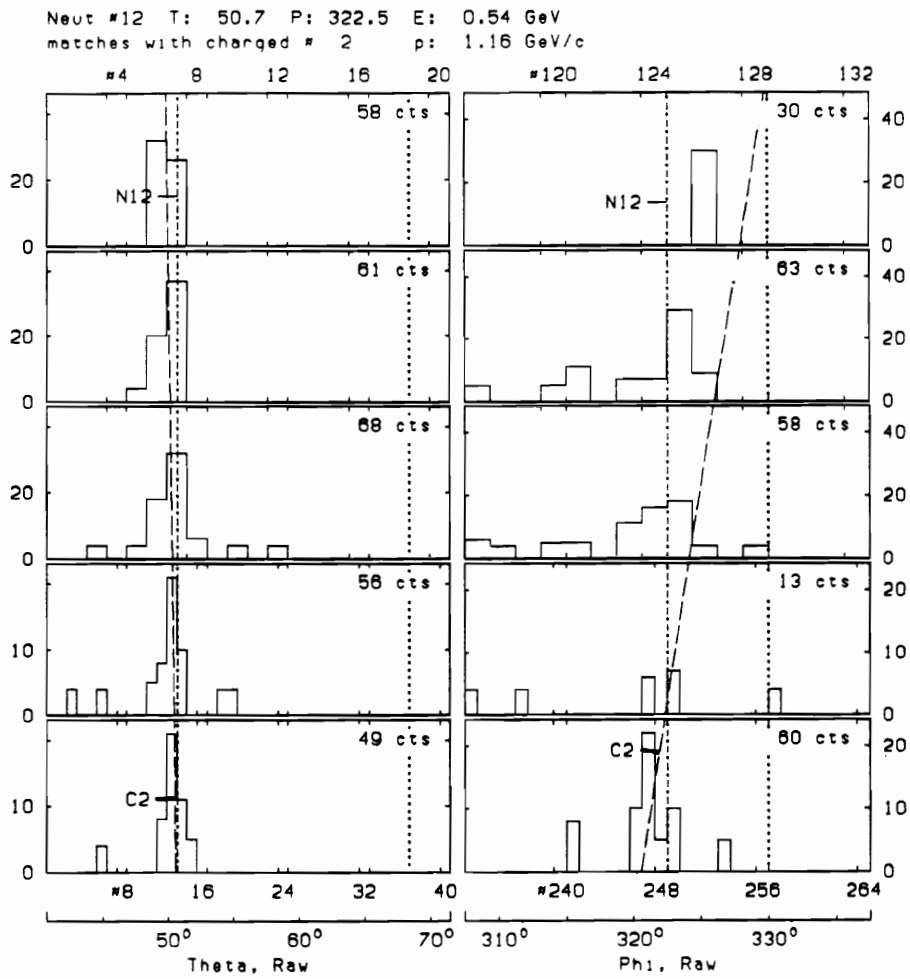

Figure 4-2: Example of a shower initiated by a charged particle.

with the shower development as described above. They may be classified as follows according to their origin [44]:

a) Clusters associated with low energy charged hadrons are sometimes mistakenly identified as neutral clusters. Most of these clusters are very low energy clusters. An example is shown in Figure 4-3.

b) Clusters which are due to hits associated with a real neutral particle, but are located far away from the main cluster. The clustering algorithm in the analysis program takes those hits and makes a new cluster out of them. These clusters normally have small energy deposits only in the 4th and 5th layers.

c) Clusters which are not merged together into one at the boundaries between detector segments.

d) Clusters caused by noise produced by discharging wires. These clusters usually have all the energy deposited in one single layer. An example is shown in Figure 4-4.

4.2 Procedure for Determination of Cuts

Several cuts are applied to all the clusters to assure that we have a relatively clean sample:

1. If the position of a cluster is matched with a CDC track within 2° in both θ and ϕ direction, the cluster is excluded.

2. A cluster which has a "complicated cluster flag" is excluded (see Section 3.1.2).

3. A cluster which doesn't satisfy shower counter acceptance cut of $|cos\theta| \leq 0.73$ is excluded, because any clusters with θ angle beyond this region will have part of their energy lost in the crack between shower counter and endcap detectors.

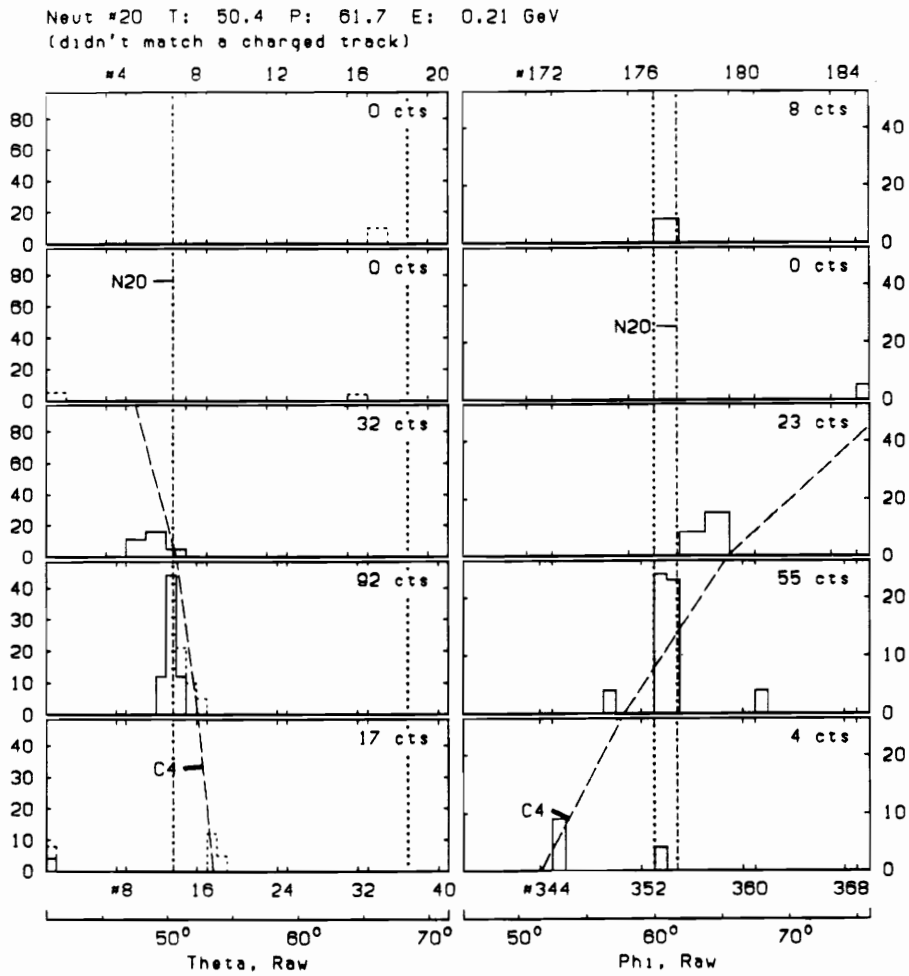

Figure 4-3: Example of a "ghost" cluster caused by charged tracks.

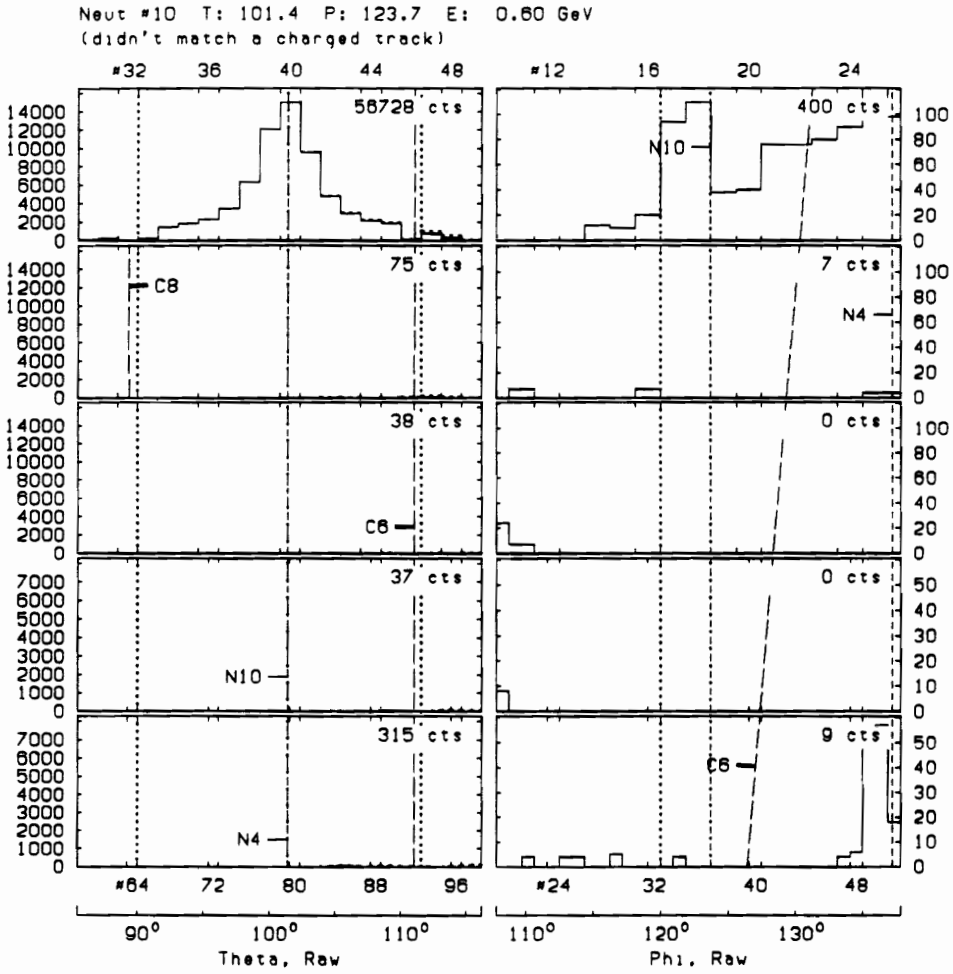

Figure 4-4: Example of a cluster caused by discharging wires.

Our goal is to develop a set of cuts to eliminate as many "ghost" clusters as possible, and meanwhile to try to keep as many good clusters as possible. These cuts are mainly developed through utilizing the difference in the shower longitudinal development behavior between the good clusters and "ghost" clusters, thus the cuts are only effective in eliminating the "ghost" clusters. As for the other two kinds of misidentified photons (see the previous section), they correspond to showers caused by real physical particles. Thus we can not simply use cuts to eliminate them. Their contribution to the inclusive photon cross sections are accounted for in the process of determing the shower counter efficiency as described in Section 4.3.1.

Let us define the variables which we use to represent the longitudinal shower development. As shown in Figure 4-5, for a given cluster E_i ($i = 1 - 5$) is the energy deposit in the i-th layer. $E_{max} = Max(E_i)$ is the maximum among the energy deposits E_i, and

$$E_{tot} = \sum_{i=1}^{5} E_i$$

is the total energy deposited for the cluster. Therefore E_i/E_{tot} is the fractional energy deposit in the i-th layer, and E_{max}/E_{tot} is the maximum fractional energy deposit in one layer for this cluster. Our goal is to compare E_i/E_{tot} and E_{max}/E_{tot} behaviors for "good" and "ghost" clusters.

A sample of 10 GeV photons was generated. After the full simulation of these photons to take into account the detector effect, we used the SHC offline analysis to go through the cluster-finding and energy-determining processes. The resultant energy spectrum of those photons is shown in Figure 4-6. Since we know the generated photon energy is 10 GeV, adding the effect of the detector, it is reasonable to expect that the peak centered around 10 GeV in the energy spectrum corresponds to the real photons which were generated. The other peak close to zero energy corresponds to "ghost" clusters. We call clusters with energies above 4 GeV "good" clusters, and those with energies below 4 GeV "ghost" clusters.

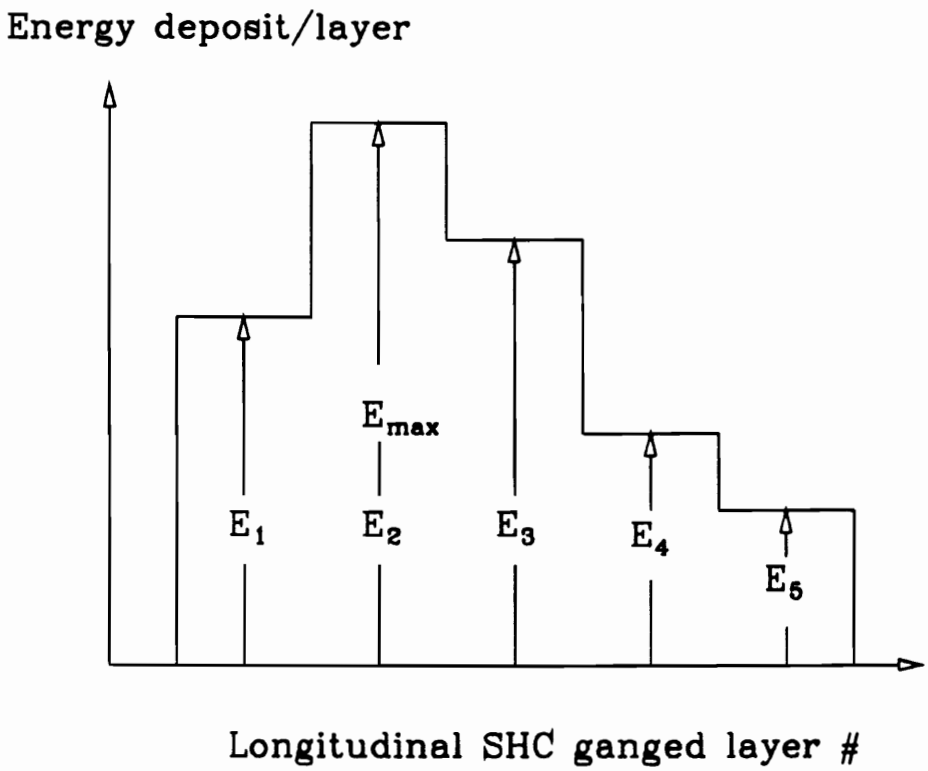

Figure 4-5: Definition of E_i and E_{max}.

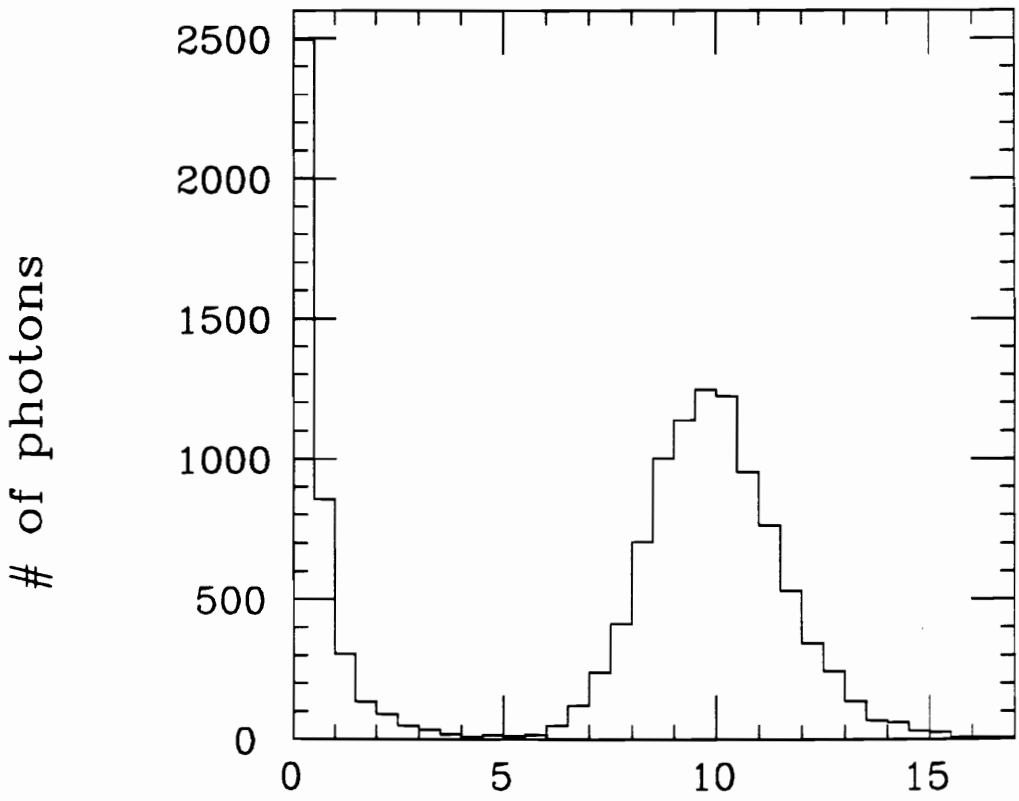

Figure 4-6: Energy spectrum of 10 GeV generated photons after simulation and SHC analysis

The maximum fractional energy deposit E_{max}/E_{tot} histograms for the "good" clusters and the "ghost" clusters are shown in Figure 4-7. So, if we set a cut at 60%, *i.e.* require the maximum fractional energy deposit in one single layer for each cluster be no more than 60%, then we will lose very few "good" clusters and get rid of about two-thirds of the "ghost" clusters.

The scatter plots for the fractional energy deposit in the second layer versus that in the third layer are shown in Figure 4-8 and Figure 4-9, for "good" clusters and for "ghost" clusters, respectively. Note that for "good" clusters there are very few clusters located near the $E_2/E_{tot} = 0$ and $E_3/E_{tot} = 0$ region, while a considerable number of "ghost" clusters are found in this region. After comparing these two figures, we decide to put the following cuts on the fractional energy deposit:

$$E_2/E_{tot} > 0$$

$$E_3/E_{tot} \geq 10\%$$

The numbers of "good" clusters and "ghost" clusters before and after our fractional energy deposit cuts are shown in Table 4-1. The energy spectrum of photons with all three fractional energy deposit cuts applied is shown in Figure 4-10. Compared to Figure 4-6, the peak corresponding to the "ghost" clusters has been reduced substantially (about 78% being cut off), while most of the "good" clusters (about 97%) survived the cuts.

Here we summarize all the cuts we discussed in this section:

1. Cluster matched with a charged track within 2° in both θ and ϕ is eliminated.
2. Cluster with the "complicated cluster flag" is eliminated.
3. $|cos\theta| \leq 0.73$.
4. $E_{max}/E_{tot} \leq 60\%$.

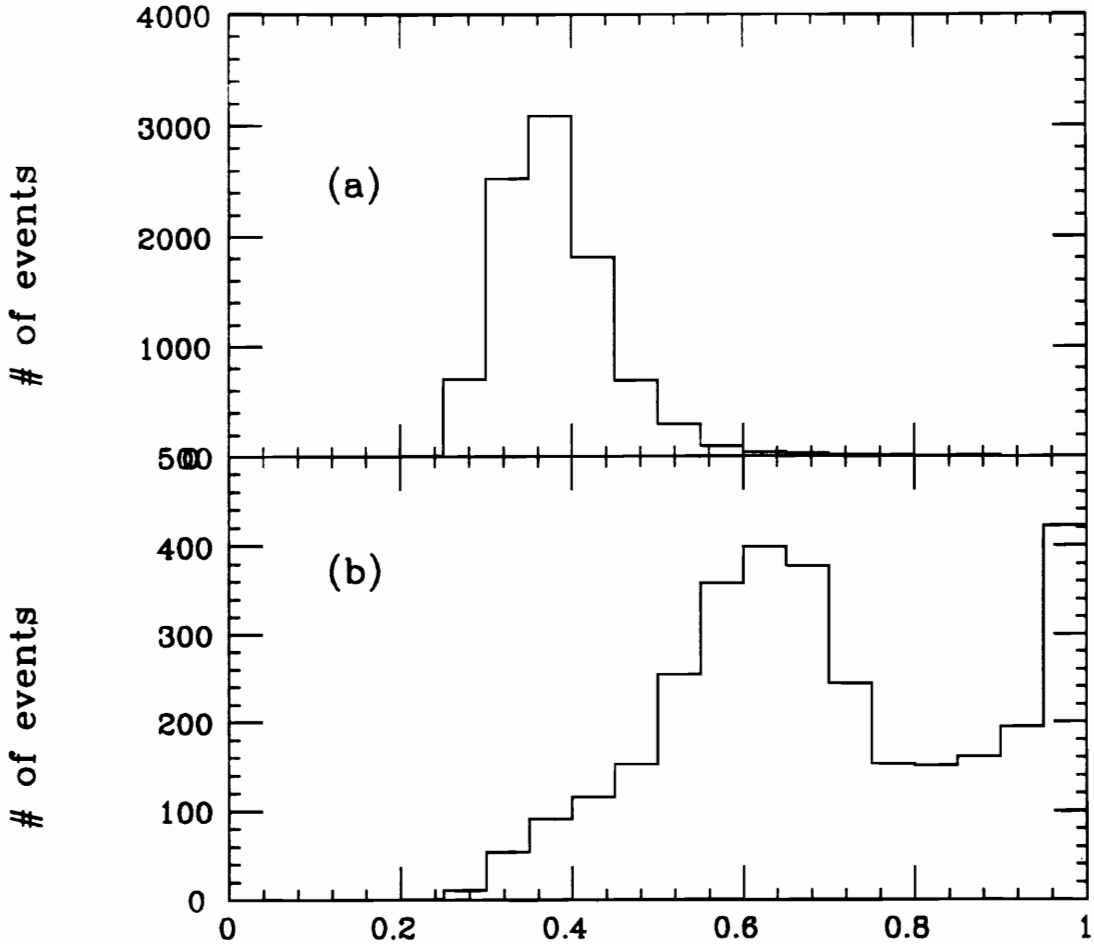

Figure 4-7: E_{max}/E_{tot} for (a) "good" clusters (b) "ghost" clusters.

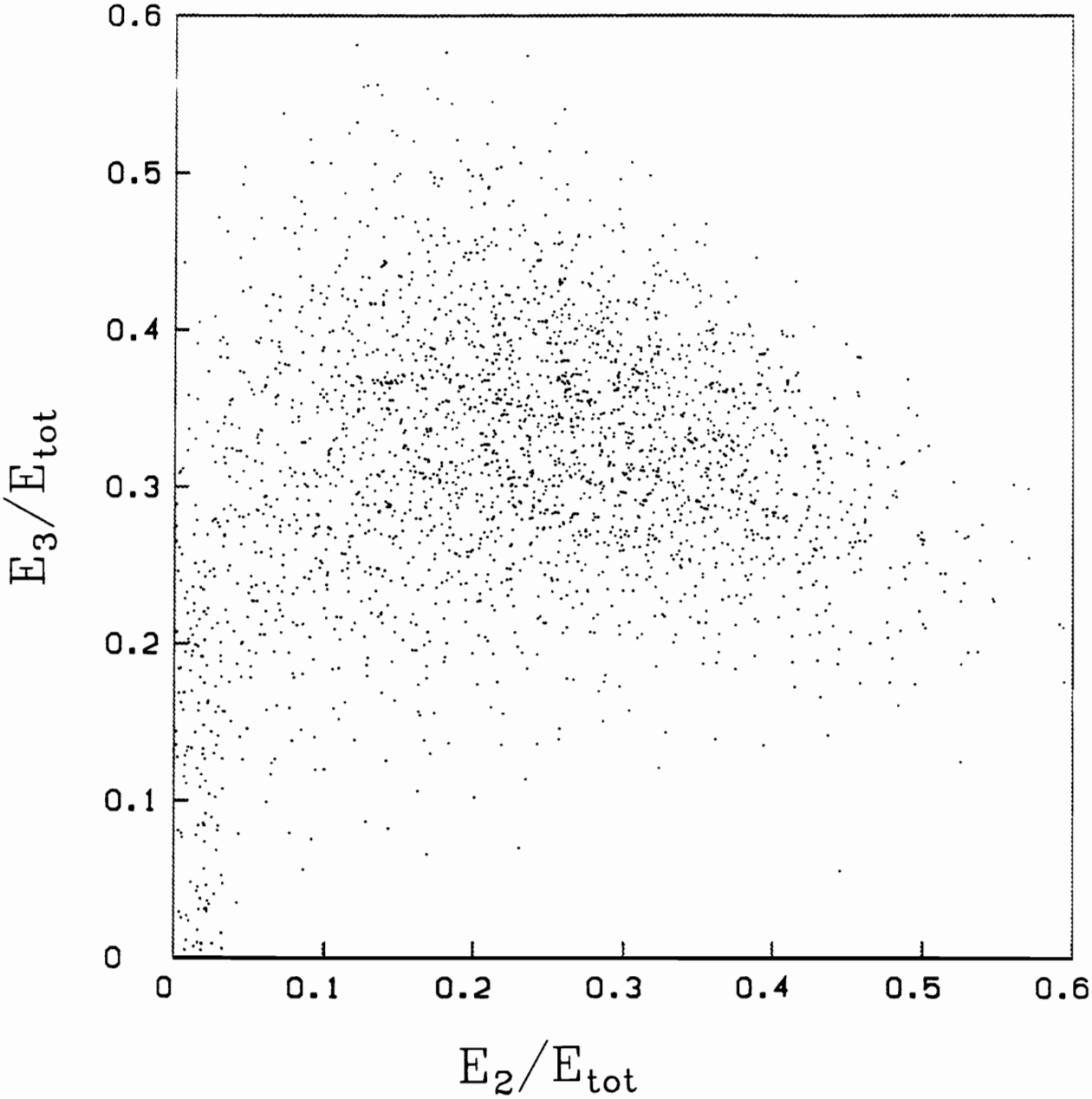

Figure 4-8: Fractional energy deposit in 2nd layer vs 3rd layer for "good" clusters

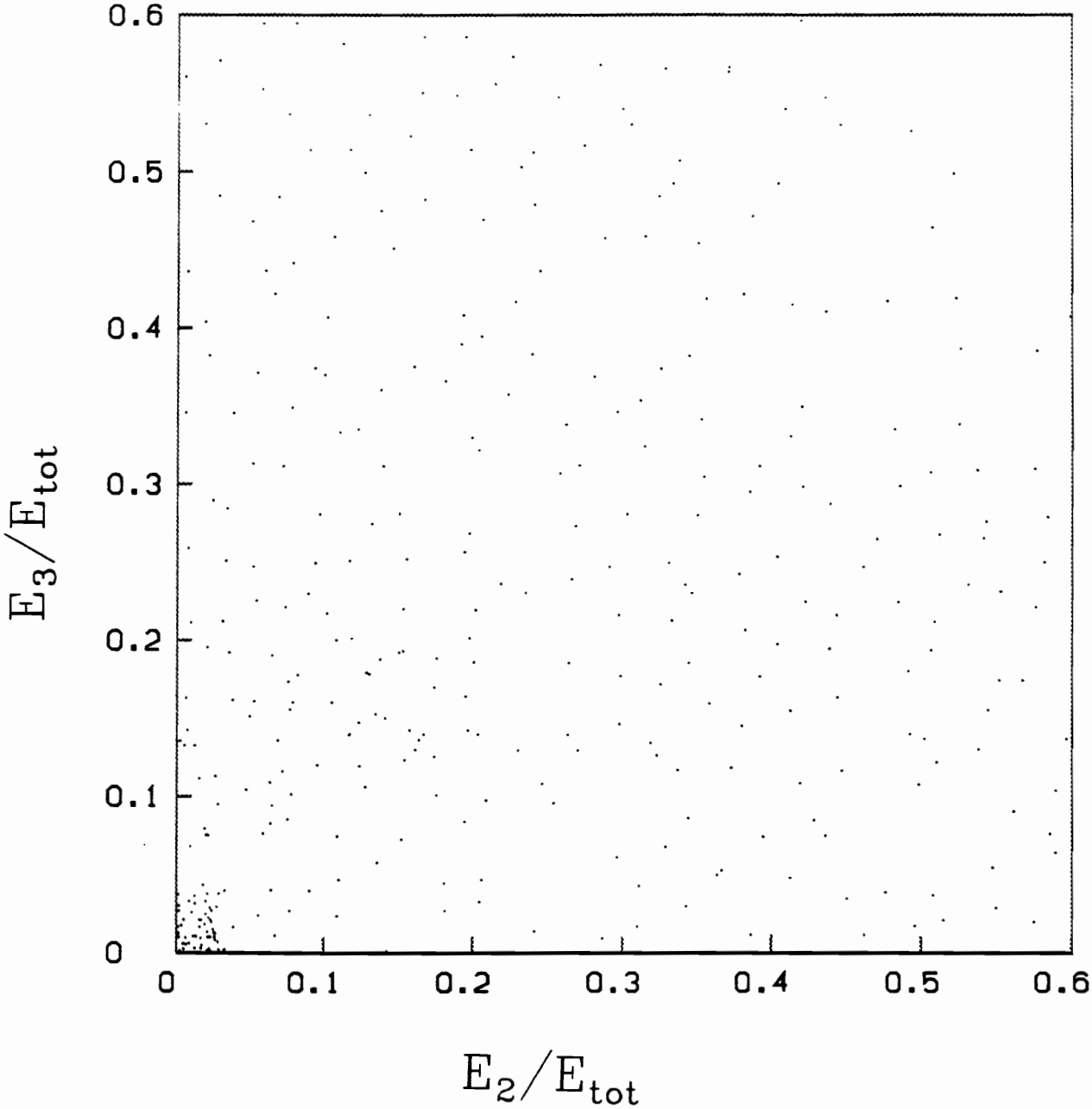

Figure 4-9: Fractional energy deposit in 2nd layer vs 3rd layer for "ghost" clusters

Table 4-1: Effect of the fractional energy deposit cuts

Cut(s)	good cluster # surviving cut(s)	ghost cluster # surviving cut(s)
No cuts	9378	3985
$E_{max}/E_{tot} \leq 60\%$ only	9213	1037
$E_2/E_{tot} > 0$ only	9249	2843
$E_3/E_{tot} \geq 10\%$ only	9189	2434
All above cuts	9119	880

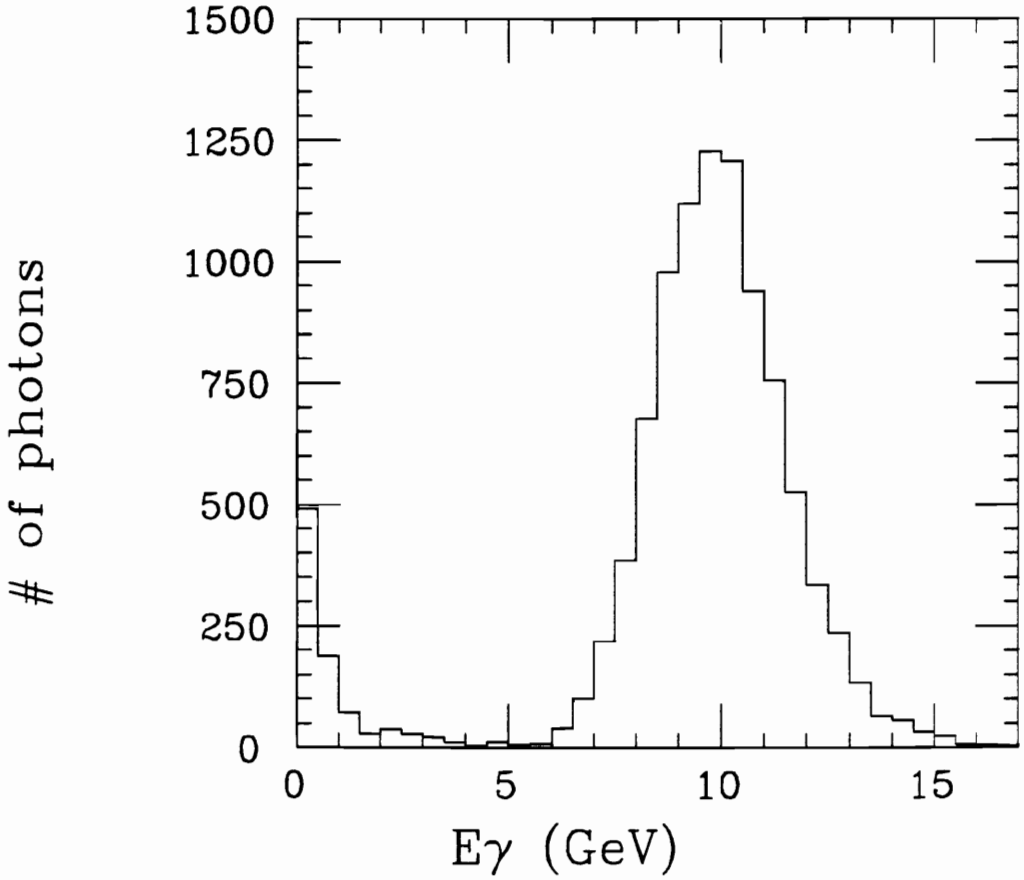

Figure 4-10: Energy spectrum of 10 GeV photons after the fractional energy deposit cuts

5. $E_2/E_{tot} > 0$.

6. $E_3/E_{tot} \geq 10\%$.

4.3 Inclusive Photon Analysis

In this section we proceed to unfold the detector effect on the experimental spectra, and then to convert the spectra into the scaled differential cross sections. Systematic errors are studied. We compare our cross sections with those obtained previously and also determine the existence of the final state radiation in the inclusive cross sections.

4.3.1 Inclusive Photon Spectrum

We use the Monte Carlo techniques to unfold the detector properties on the photon spectra, and then to obtain scaled differential cross sections for the inclusive photon production.

Using simulated and reconstructed inclusive photon spectra, we define c_i, classification fraction in the i-th bin of x, where $x = 2\,E_\gamma/\sqrt{s}$ as follows:

$$c_i = N^i_{good}/N^i_{recon}$$

Also defined is e_i, detection efficiency in the i-th bin of x as:

$$e_i = N^i_{good}/N^i_{gen}$$

where N^i_{recon} is the number of reconstructed neutral clusters in the i-th bin of x, N^i_{good} is the number of neutral clusters in the i-th bin of x which actually correspond to simulated photons, and N^i_{gen} is the number of generated photons in the i-th bin.

If N^i_{data} is the number of neutral clusters observed in the i-th bin of x, then the number of real photons in the same bin is given by

$$N^i_{real} = N^i_{data} * c_i/e_i \tag{4.1}$$

The scaled invariant differential cross section is calculated as:

$$s\,\frac{d\sigma}{dx} = s\,\frac{N^i_{real}}{L * bsn} \tag{4.2}$$

where L is integrated luminosity, and bsn is the bin size for x.

The detection efficiency and classification fraction used for $\sqrt{s} = 57$ GeV is shown in Figure 4-11 and Figure 4-12 respectively.

The differential cross section spectra for different center-of-mass energies are shown in Figure 4-13, Figure 4-14, Figure 4-15, and Figure 4-16 (only statistical errors are included in these figures).

The comparison of AMY data with those of the JADE experiment [17] is shown in Figure 4-17 (only statistical errors are included). The AMY data shown are combined data at 55 GeV, 56 GeV, 57 GeV and 58 GeV. In the region of $x < 0.5$, our data agree well with the JADE data at $\sqrt{s} = 34$ GeV. This is expected because in this region photons mainly come from hadron decays, thus the differential cross section scales with the center-of-mass energy as a function of x as mentioned in Section 1.2.1. Note that our first data point at $x = 0.05$ appears to be higher than the corresponding JADE data point; it is caused by a binning effect. Our data point includes the region of $x = 0-0.1$, while for the JADE data, each data point includes a interval of 0.01 of x only. Since this is the steepest part of the spectrum, the binning effect appears more obvious in comparison with the rest of the spectrum. In the region of $x > 0.5$, photons mainly come from radiative processes. This part of the inclusive spectrum is not expected to be scale invariant. As shown in Figure 4-17, AMY data have a different shape from the JADE data in the $x > 0.5$ region.

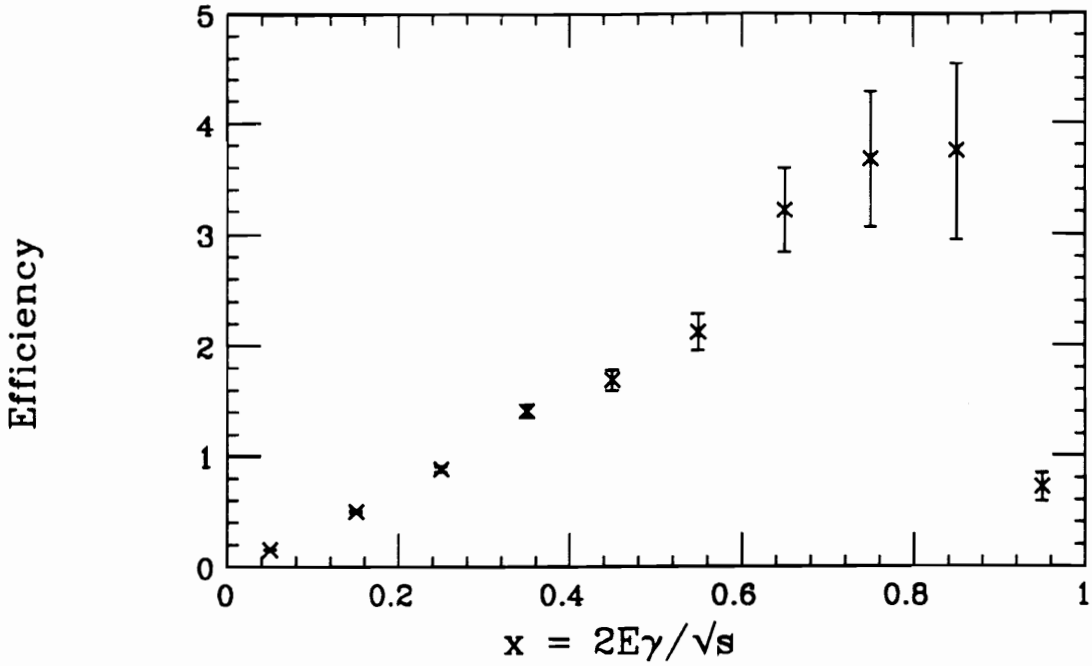

Figure 4-11: Detection efficiency.

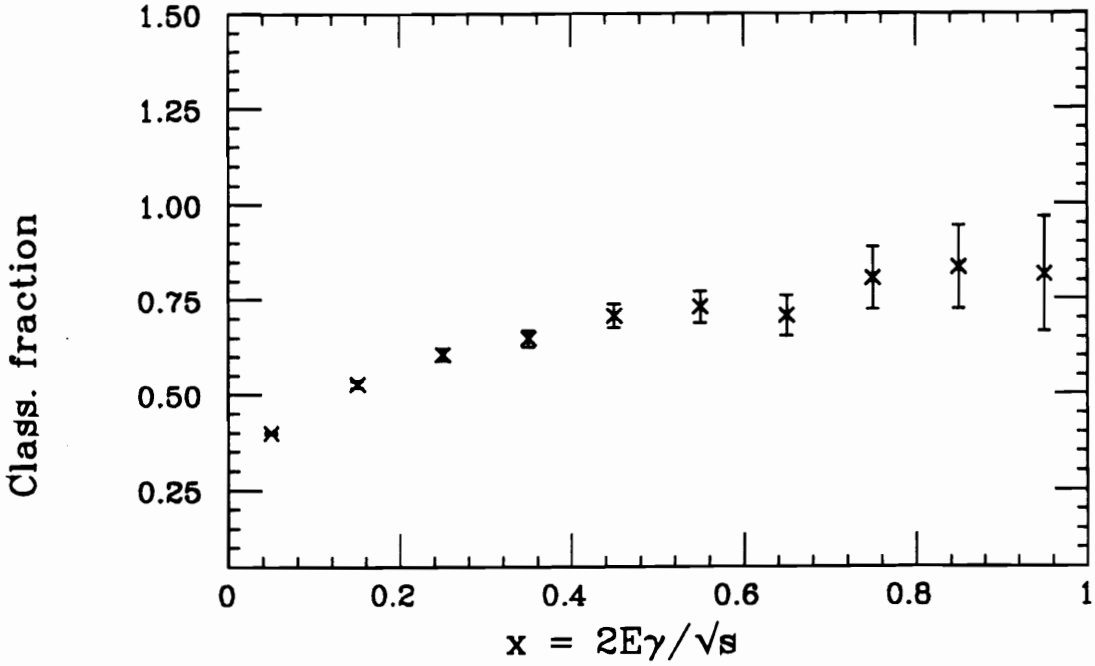

Figure 4-12: Classification fraction.

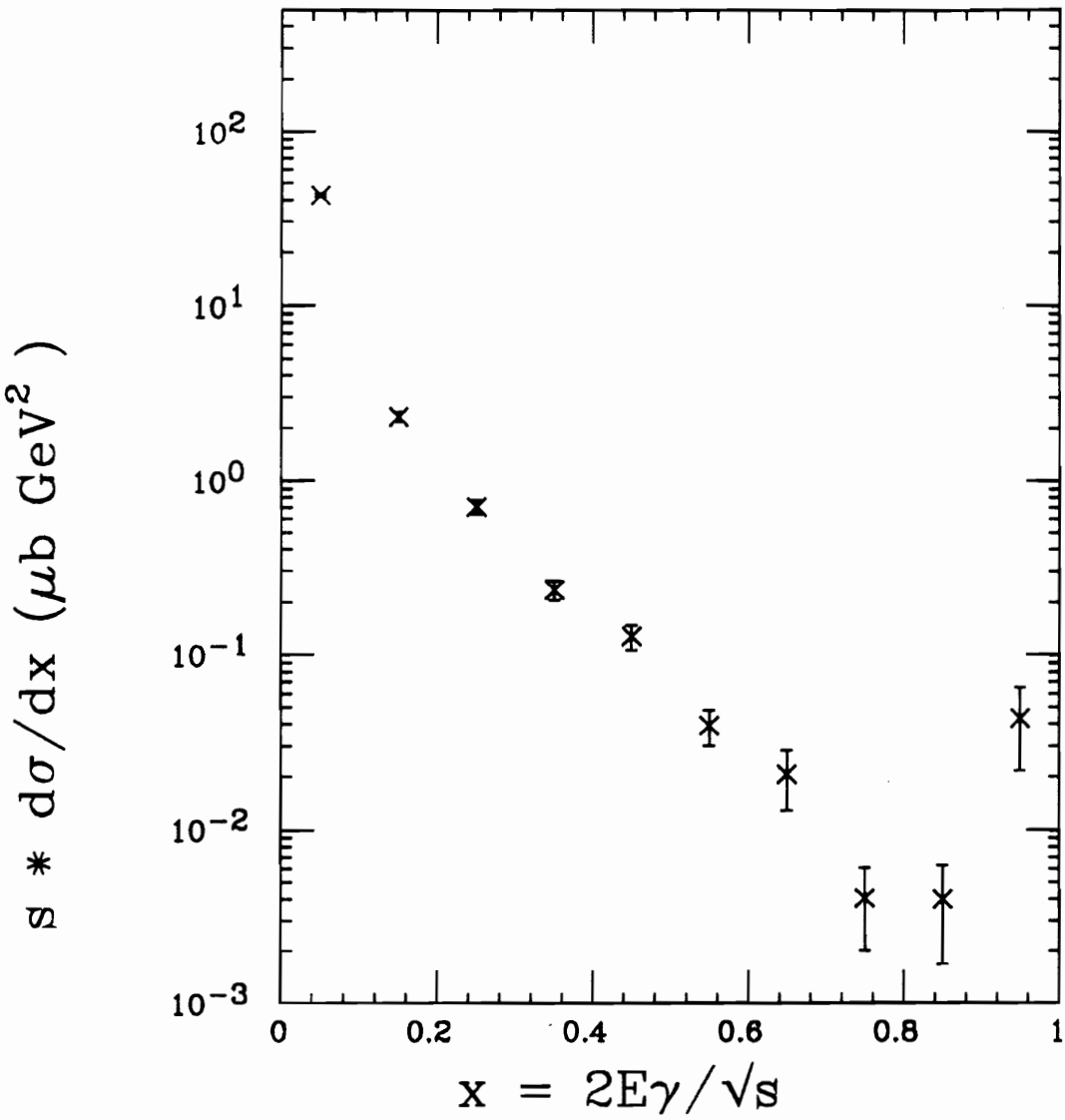

Figure 4-13: Inclusive photon spectrum for 55 GeV data.

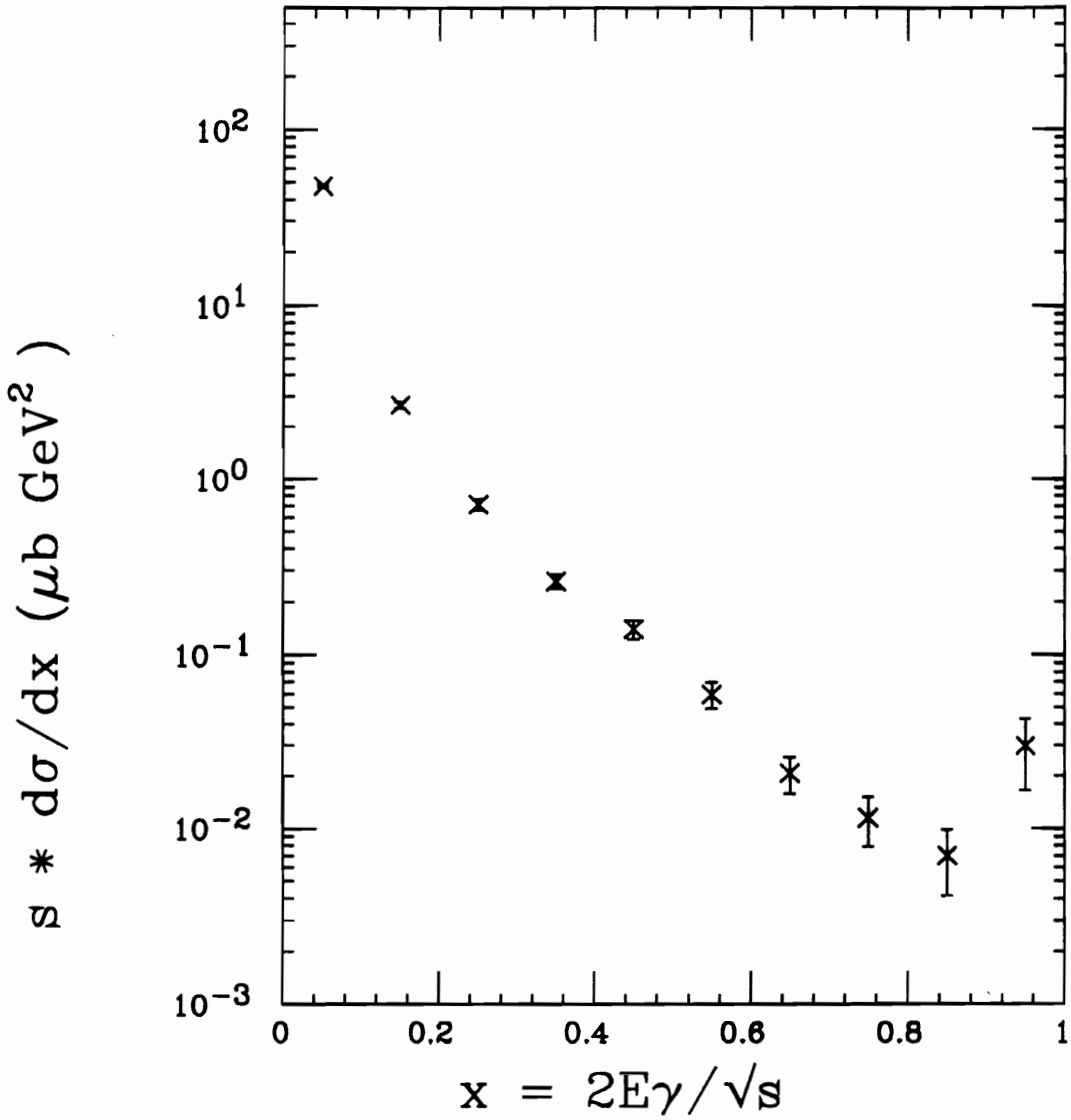

Figure 4-14: Inclusive photon spectrum for 56 GeV data.

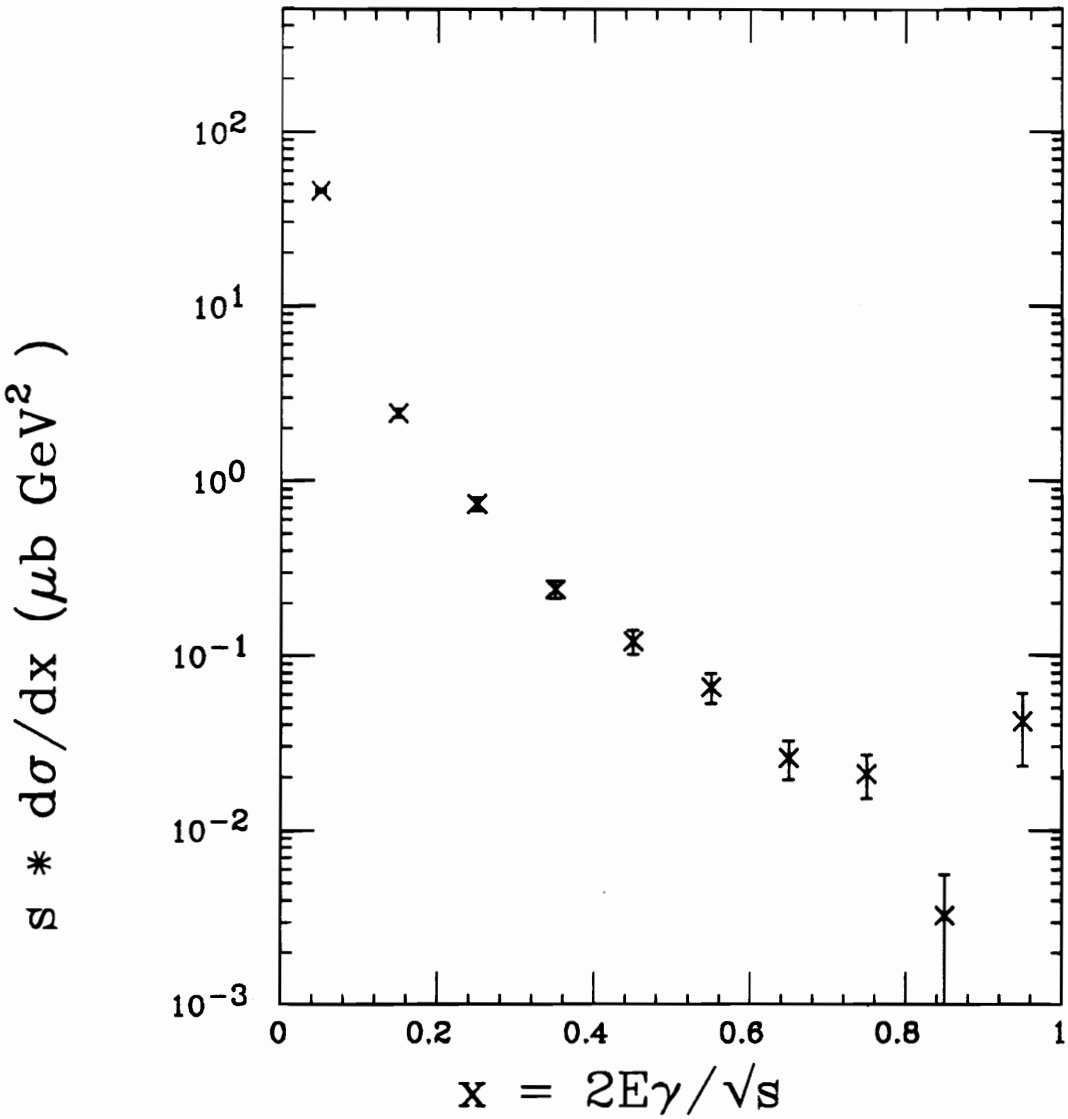

Figure 4-15: Inclusive photon spectrum for 57 GeV data.

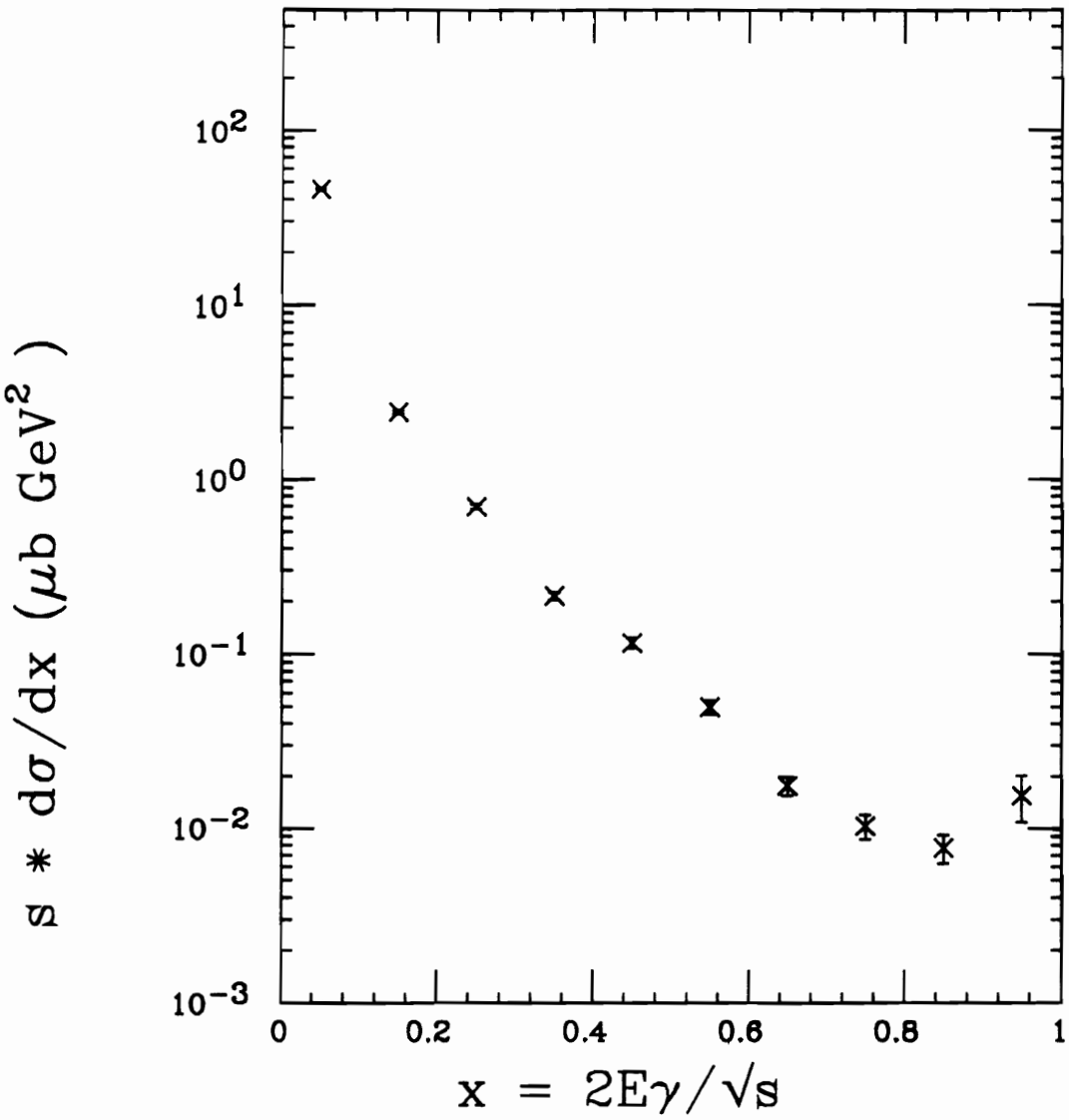

Figure 4-16: Inclusive photon spectrum for 58 GeV data.

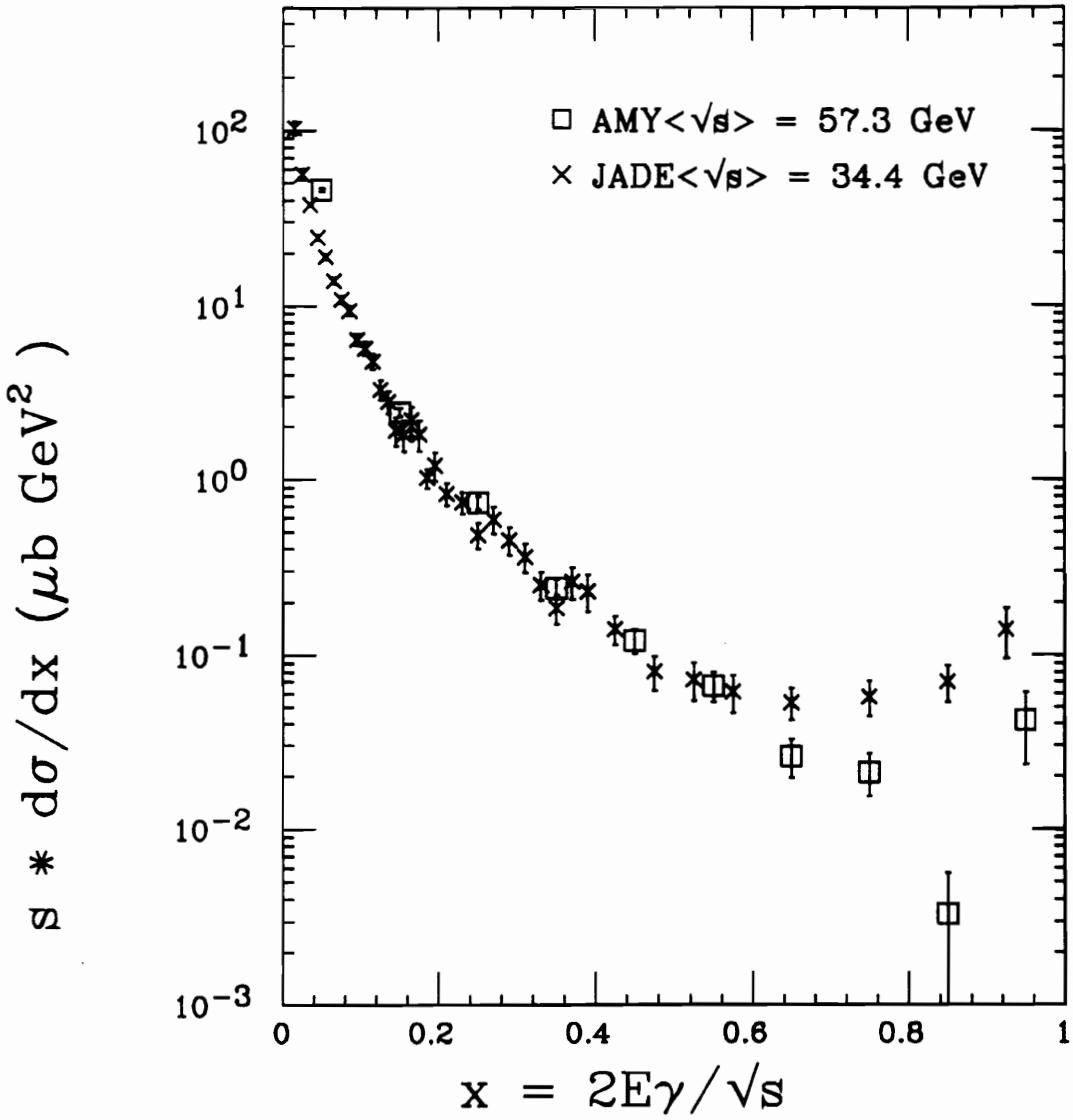

Figure 4-17: Comparison of inclusive photon spectrum between AMY data and JADE experiment data.

4.3.2 Systematic Errors

From Equation 4.1 and Equation 4.2, we know that luminosity L, detection efficiency e_i and classification fraction c_i contribute directly to the systematic errors of the cross sections. Besides the above, triggering system's inefficiency also could contribute to the systematic errors.

The systematic errors in luminosity measurements for real data, including uncertainties in detector alignment, are about 2.4% [32] [45].

Inefficiency in the trigger system is estimated by comparing relative efficiencies of redundant trigger components. For hadronic events, the overall inefficiency is less than 1% [26].

The errors contributed by detector efficiency e_i and classification fraction c_i are shown in Figure 4-11 and Figure 4-12.

All the above are added together in quadrature to give us the total systematic errors.

Table 4-2 shows the inclusive photon cross sections for combined AMY data of 55 GeV, 56 GeV, 57 GeV and 58 GeV, including both statistical and systematic errors.

4.3.3 Final State Radiation in Inclusive Photon Spectra

We want to compare our experimental data with the theoretical prediction for the final state radiation (FSR). As a theoretical prediction we use Lund 7.2 (Section 3.2.1), which is a 5-flavor fragmentation model with initial and final state photon emissions, included with the option that final state radiation effect can be turned off.

A comparison of the inclusive photon spectrum generated by Lund 7.2 with and without final state radiation is shown in Figure 4-18. The solid line is with final state radiation, dotted line is without final state radiation. Both histograms here are at generator level, *i.e.*

Table 4-2: Inclusive photon cross sections at center-of-mass energy of 57.3 GeV

$< x >$	$s\, d\sigma/dx(\mu b\, GeV^2) \pm stat.err \pm sys.err$
0.05	45.79 ± 0.93 ± 1.19
0.15	2.43 ± 0.14 ± 0.09
0.25	0.73 ± 0.06 ± 0.03
0.35	0.24 ± 0.03 ± 0.01
0.45	0.12 ± 0.02 ± 0.009
0.55	0.066 ± 0.01 ± 0.007
0.65	0.026 ± 0.006 ± 0.004
0.75	0.021 ± 0.006 ± 0.004
0.85	0.0033 ± 0.002 ± 0.0008
0.95	0.042 ± 0.02 ± 0.01

without going through full simulation and SHC analysis. The final state radiation effect shows up only around $x = 0.5$–0.9 region, with photons from fragmentation and initial state radiation dominating at the other values of x. The difference between the two histograms in Figure 4-18 is estimated to be 0.3%.

The ratio of the histogram values in each bin without final state radiation to the corresponding value with final state radiation is shown in Figure 4-19.

The comparisons between our experimental data and Lund 7.2 Monte Carlo with and without final state radiation are shown in Figure 4-20 for 55 GeV and 56 GeV, Figure 4-21 for 57 GeV and 58 GeV data respectively. Here the solid histogram corresponding to Lund 7.2 with final state radiation is calculated by using fully simulated Monte Carlo events, while the dotted one corresponding to Lund 7.2 without final state radiation is calculated by using the same fully simulated Monte Carlo events multiplied by the correction ratio shown in Figure 4-19. All the figures here include only statistical errors. The same also is true for the χ^2 calculations below.

In the region of $x < 0.5$, photons from fragmentation processes dominate. As shown in Figure 4-20b and Figure 4-21a, 56 GeV and 57 GeV data agree with the Monte Carlo calculations very well in the fragmentation region.

As shown in Figure 4-20a, 55 GeV data do not agree with Monte Carlo very well in this region. The most likely reason is that for 55 GeV data, the shower counter used HRS gas (for the rest of the data, 49.3% Ar, 49.3% C_2H_6, 1.5% C_2H_5OH is used), as mentioned in Section 2.2.3. Because of limited statistics, the saturation effects for HRS gas are not well studied and it is not possible to do SHC energy calibration accurately for 55 GeV data. As a result, the uncertainty of the energy calibration is 3 to 4 times worse in comparison with the other data sets. Thus the comparison between 55 GeV data and Lund MC is subject to more uncertainty.

As shown in Figure 4-21b, 58 GeV data are consistently lower than the Monte Carlo calcu-

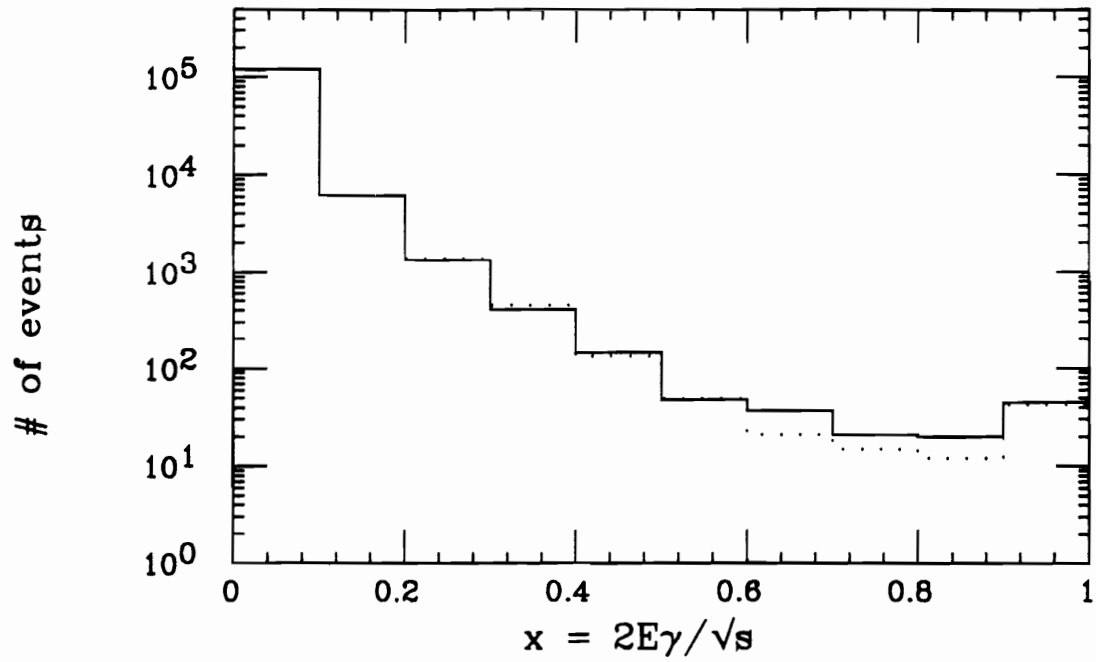

Figure 4-18: Comparison between Lund 7.2 with and without final state radiation.

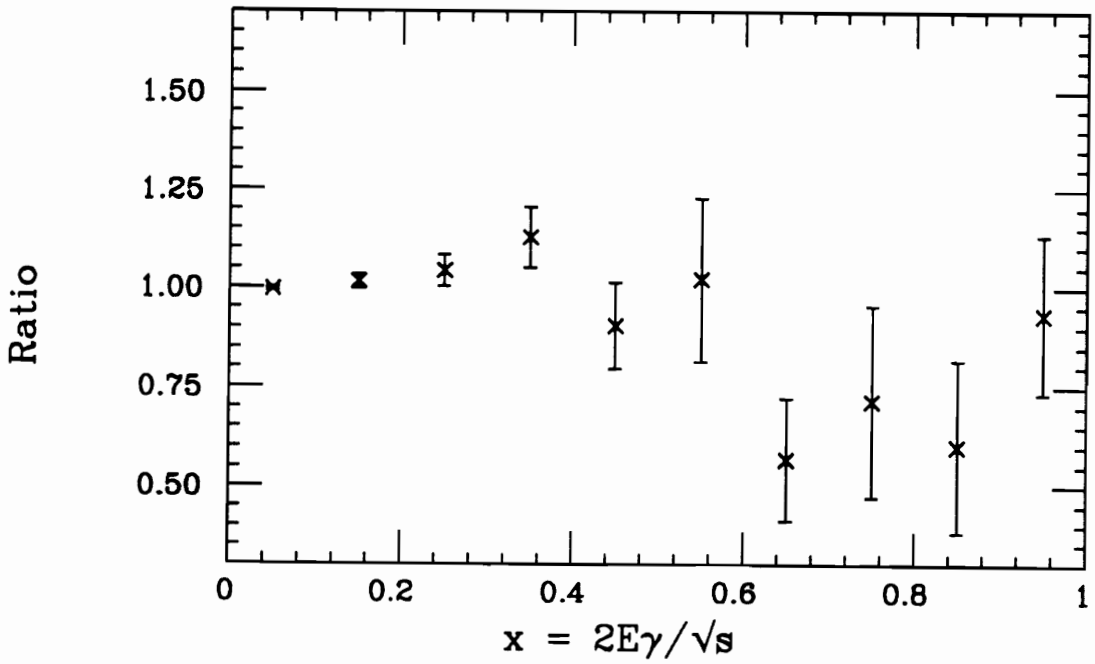

Figure 4-19: Ratio of Lund 7.2 without to with final state radiation.

lations for $x < 0.5$ region. Thus we suspect the luminosity for this energy may be measured too high. We force the data in the first bin (x=0.05) to agree with the Monte Carlo calculation, then use the adjusted luminosity to re-calculate the data points in the other bins. The data points using the adjusted luminosity agree well with Lund MC in the fragmentation region. For consistency this same method is also used for adjusting luminosities for 55 GeV, 56 GeV and 57 GeV data.

As we indicated earlier in this section, the effect of final state radiation mainly shows up in the higher energy region. So we limit ourselves to the x = 0.4–1.0 region for the following discussion.

As shown in Figure 4-20 and Figure 4-21, in this region 56 GeV and 57 GeV data agree with the solid histogram better, which corresponding to Lund 7.2 with both initial state radiation and final state radiation corrections. χ^2 values of the data to the two different histograms in x = 0.4–1.0 region are given in Table 4-3. For both 56 GeV and 57 GeV data, we get a better agreement between the data and the Monte Carlo calculation which includes the final state radiation effect, for either the measured or the adjusted luminosities.

As shown in Figure 4-21b, 58 GeV data also agree with the solid histogram better in the x = 0.4–1.0 region by using the adjusted luminosity. The χ^2 value is shown in Table 4-3.

χ^2 calculations for the data to the two different MC histograms in the x = 0–1.0 region are shown in Table 4-4 for all 4 data sets. Again we get better agreement between data and Lund MC which includes final state radiation, for 56 GeV, 57 GeV and 58 GeV data, by using either the measured or the adjusted luminosities.

In general we think that the solid histogram in Figure 4-20 and Figure 4-21, which corresponds to Lund 7.2 with full radiation corrections, describes our experimental data better than the dotted histogram, which only has initial state radiation correction.

Table 4-3: χ^2 values of data to Monte Carlo in the x=0.4–1.0 region.

Data	Luminosity (pb^{-1})	deg. of freedom	χ^2 (with FSR)	χ^2 (no FSR)
55GeV	3.266±0.039	6	27.10	16.28
56GeV	5.993±0.053	6	1.95	4.79
57GeV	4.398±0.046	6	7.28	9.16
58GeV	27.156±0.076	6	26.37	18.47
	Using adjusted luminosities			
55GeV	2.787±0.033	6	15.77	10.47
56GeV	5.734±0.051	6	1.58	5.86
57GeV	4.046±0.042	6	6.95	10.64
58GeV	24.916±0.069	6	11.52	15.81

Table 4-4: χ^2 values of data to Monte Carlo in the x=0–1.0 region.

Data	Luminosity (pb^{-1})	deg. of freedom	χ^2 (with FSR)	χ^2 (no FSR)
55GeV	3.266±0.039	10	87.55	79.68
56GeV	5.993±0.053	10	10.78	16.18
57GeV	4.398±0.046	10	33.57	38.81
58GeV	27.156±0.076	10	172.07	193.31
	Using adjusted luminosities			
55GeV	2.787±0.033	9	17.91	12.61
56GeV	5.734±0.051	9	1.84	7.46
57GeV	4.046±0.042	9	9.34	14.62
58GeV	24.916±0.069	9	23.30	47.52

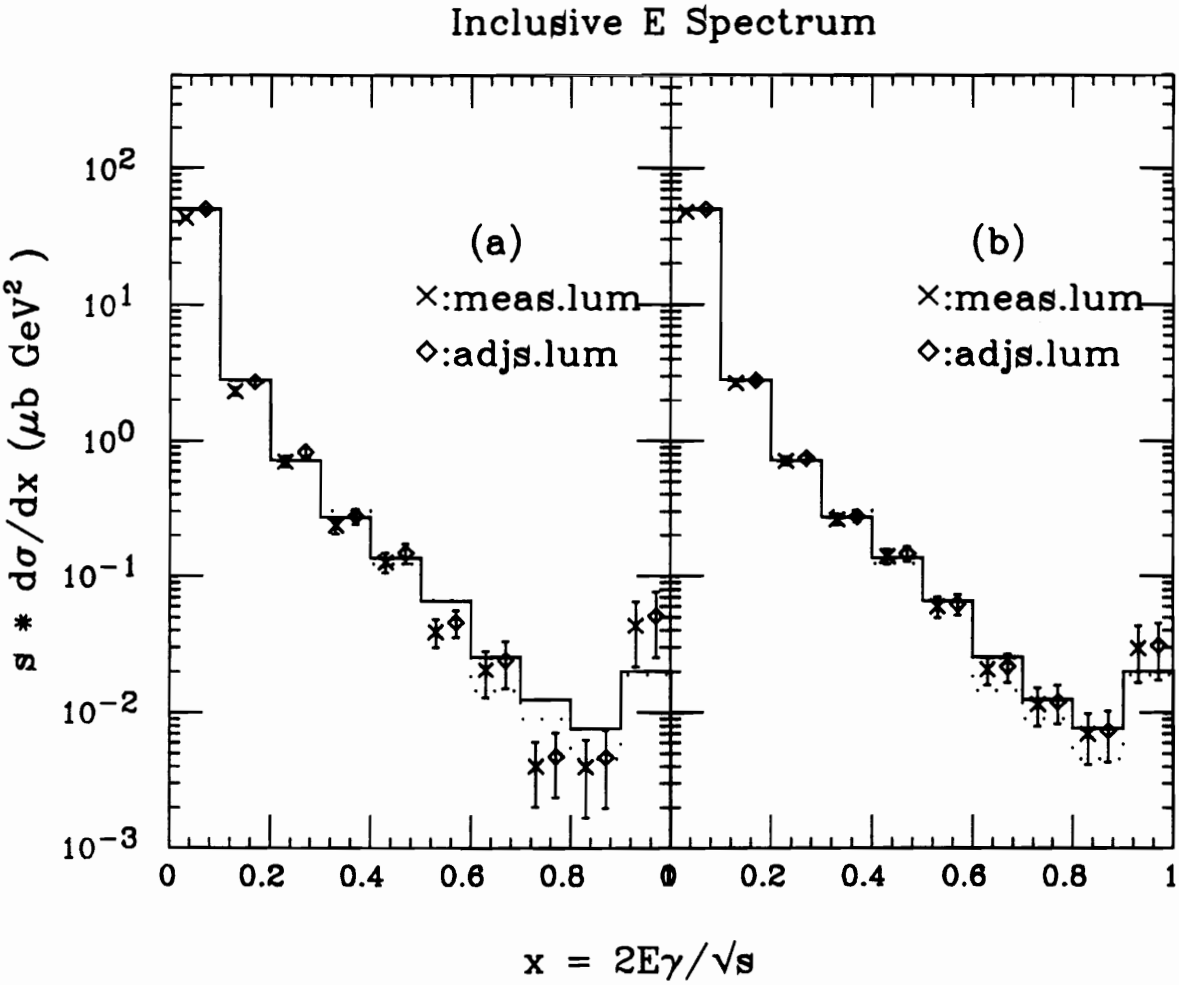

Figure 4-20: Comparison of inclusive photon spectrum between data and Lund Monte Carlo. (a) 55 GeV. (b) 56 GeV.

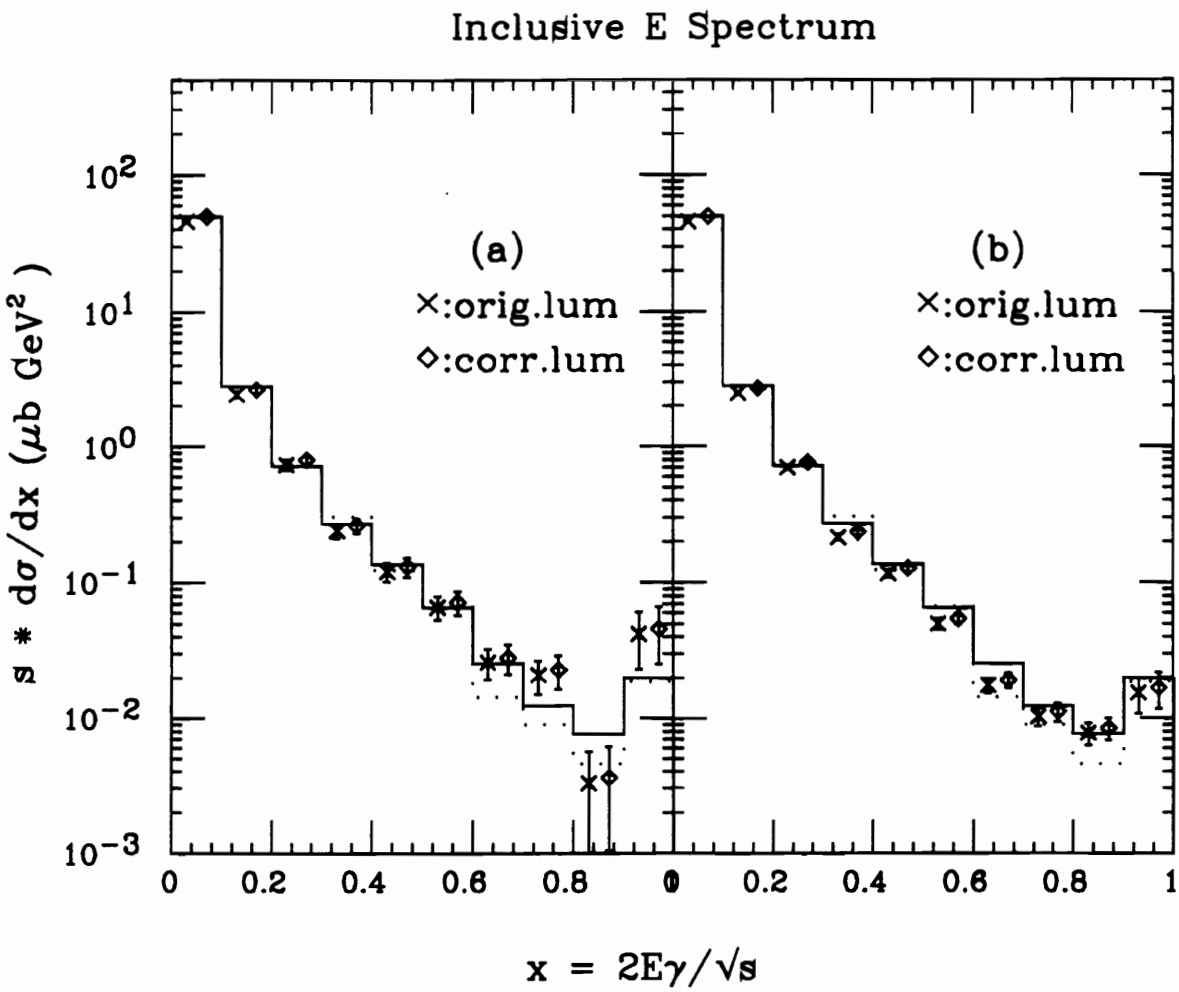

Figure 4-21: Comparison of inclusive photon spectrum between data and Lund Monte Carlo. (a) 57 GeV. (b) 58 GeV.

Chapter 5

Isolated Photon Analysis

The initial and final state radiation processes are both characterized by an isolated energetic photon. On the other hand, as discussed in Section 1.2, photons from unstable hadron decays are usually inside the hadronic jets and have relatively low energies. So, by selecting hadronic events which contain isolated energetic photons, we can pick out a mixture of concentrated initial state radiation and final state radiation events. As discussed in Section 1.2.2, if final state radiation does exist in our experiment, then it is expected that a charge asymmetry will occur in the resultant hadronic jets with respect to the incident beam direction, due to the interference between the hadronic final states with initial state radiation and final state radiation. The first part of this chapter describes the forward-backward charge asymmetry analysis.

In the second part of this chapter, we study the possibility of a new particle production which may manifest itself in the isolated photon process $e^+e^- \rightarrow \gamma + H^\circ$, where H° is the new particle. (see Section 1.2.3). Upper limits on new particle production cross sections are given.

5.1 Forward-Backward Charge Asymmetry Study

Event selection criteria are developed to select events having an energetic photon from the radiative process $e^+e^- \rightarrow q\overline{q}\gamma$ (either initial or final state radiation). The directions of the original quark pair are determined from the reconstructed hadronic jet axes. The reconstructed charges of the hadronic jets are then assigned to the respective quarks. Finally, the forward-backward charge asymmetry of the quark jets with respect to the incident beam direction is measured and compared to theoretical predictions.

5.1.1 Event Selection

In order to observe the charge asymmetry effect, we need to select the events which have photons coming from the radiative processes.

Lund 7.2 Monte Carlo events at generator level are used to develop the event selection criteria. Photons from different sources—hadron decays, initial state radiation (ISR) and final state radiation (FSR)—are compared and their differences are utilized to develop the selection criteria.

The energy spectra of the photons produced by the three different processes, after SHC acceptance cut $|cos\theta| \leq 0.73$, are presented in Figure 5-1. The photons from hadron decays are dominant in the lower energy regions, while those from radiative processes extend out to much higher energy regions. Energy cuts at the low end and high end of the energy spectrum are needed to eliminate photons from hadron decays and some of the initial state radiation photons.

Since photons from the radiative processes tend to be isolated from the hadronic jet, we impose an isolation condition on the candidate events. A cone with a half opening angle α is formed around the direction of the selected photon as in Figure 5-2. The sum of the both neutral and charged energy deposited in this cone (excluding the selected photon), E_{cone},

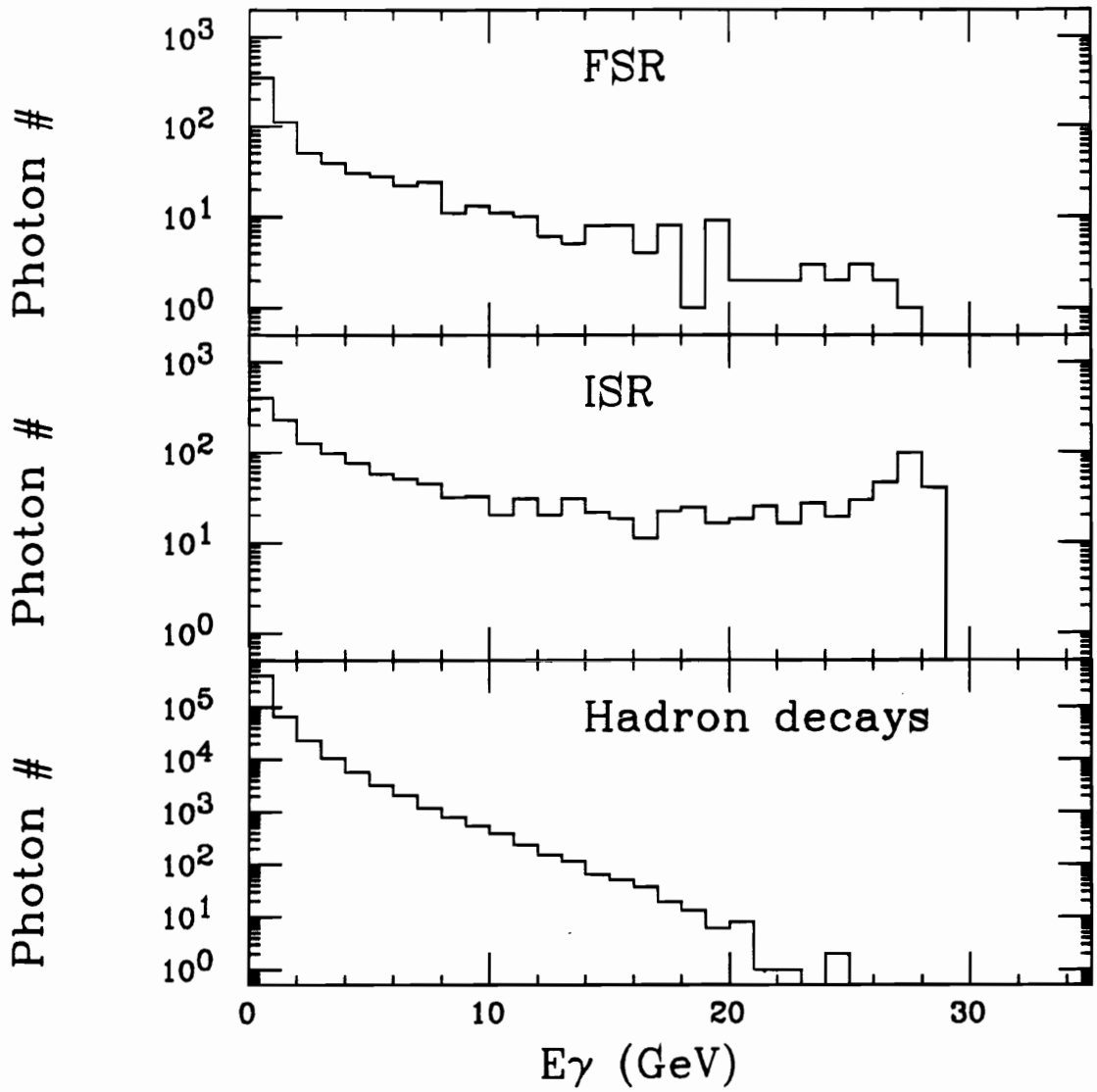

Figure 5-1: Energy spectra of photons produced by different processes.

is required to be smaller than a selected value (we call this value the cone energy cut). Figure 5-3 shows the scatter plot of photon energy vs. the cone energy E_{cone} (for $\alpha = 20°$) for photons from the final state radiation; Figure 5-4 and Figure 5-5 are the corresponding plots for photons from the initial state radiation and hadron decays. As shown in these figures, if a cone energy cut of a few GeV is applied, most of the photons from hadron decays will be eliminated while relatively few radiative photons are lost.

Figure 5-6 shows the effect of different isolation cuts for photons from the final state radiation (a pre-cut of $E_\gamma \geq 2GeV$ is applied). The vertical axis is the fraction of the photons selected for a particular choice of α and cone energy cut. We want this fraction to be as large as possible for photons from the final state radiation, and to be minimized for photons from hadron decays. Figure 5-7 is the same plot for photons from hadron decays.

After careful comparison between all the above figures, we decide to impose a photon energy cut of $4\,GeV \leq E_\gamma \leq 20\,GeV$ (for $\sqrt{s} = 57\,GeV$), and a cone energy cut of 1 GeV for $\alpha = 20°$. In order to be consistent with different center-of-mass energy data, our photon energy cut is re-written as $0.14 \leq x \leq 0.70$, where $x = 2\,E_\gamma/\sqrt{s}$.

A summary of the event selection criteria is given below:

1. Energy cut: $0.14 \leq x \leq 0.70$.
2. Isolation cut: the additional energy (both neutral and charged) deposited in a cone of 20° half opening angle around the isolated photon should be less than 1 GeV.

The efficiency of the above selection criteria for photons from different sources is listed in Table 5-1.

5.1.2 Energy Spectrum of Isolated Photons

We want to compare the isolated photon energy spectrum of our data with the theoretical prediction. We again use Lund 7.2 as the theoretical prediction.

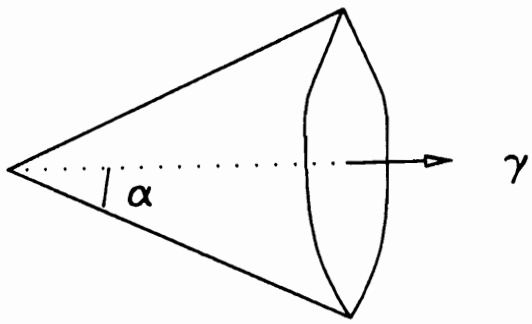

Figure 5-2: Definition of isolation cone.

Table 5-1: Efficiency of the selection criteria

Photons passing cut(s)	Photons from ISR	Photons from FSR	Photons from hadron decays
No cuts	22524	1137	767560
$cos\theta \leq 0.73$	1679	768	511212
$0.14 \leq x \leq 0.70$	501	198	14744
Isolation cut	453	117	33
Percentage of passing cuts	2.0%	10.3%	0.004%

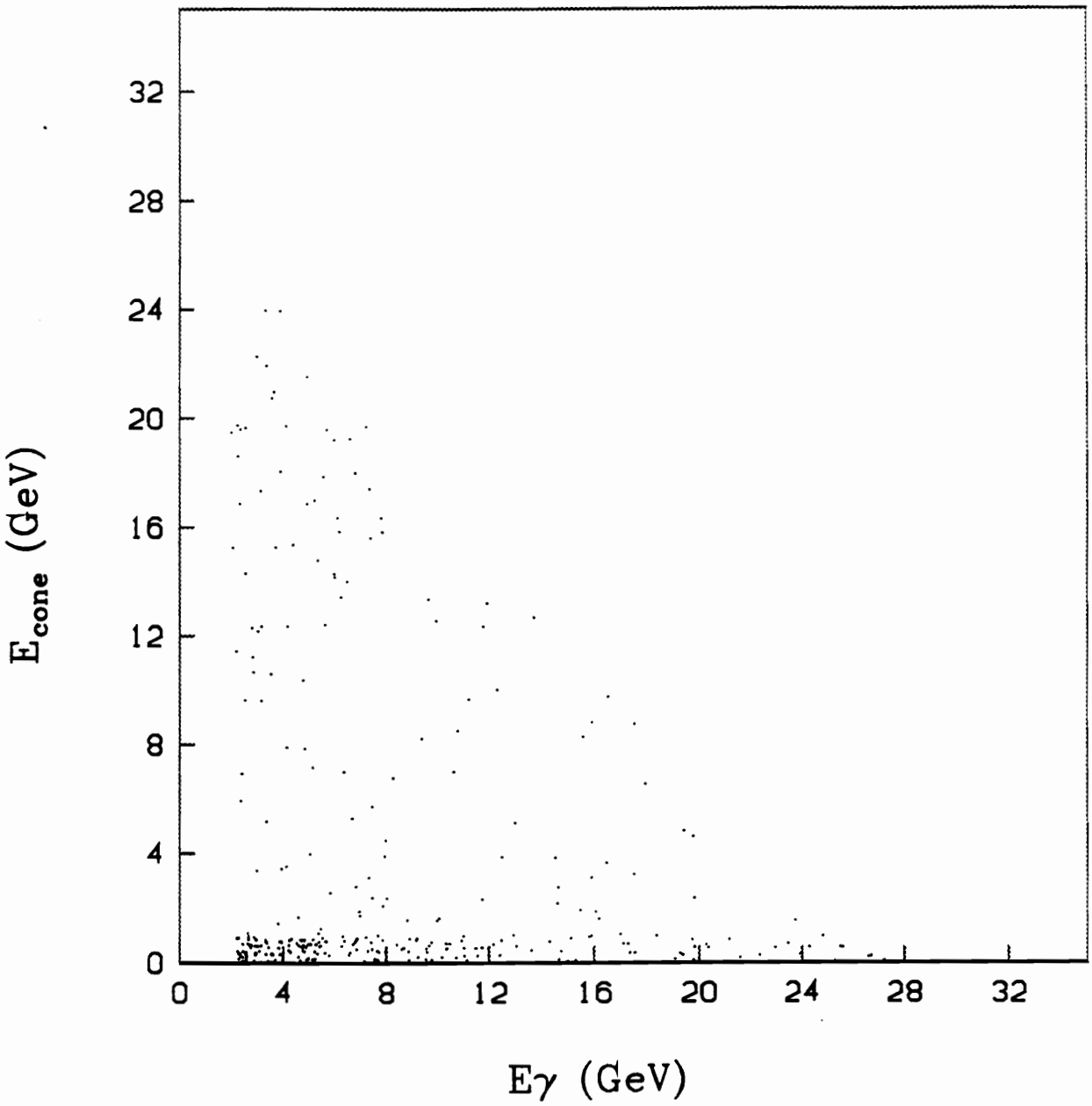

Figure 5-3: Photon energy vs. the cone energy for photons from the final state radiation.

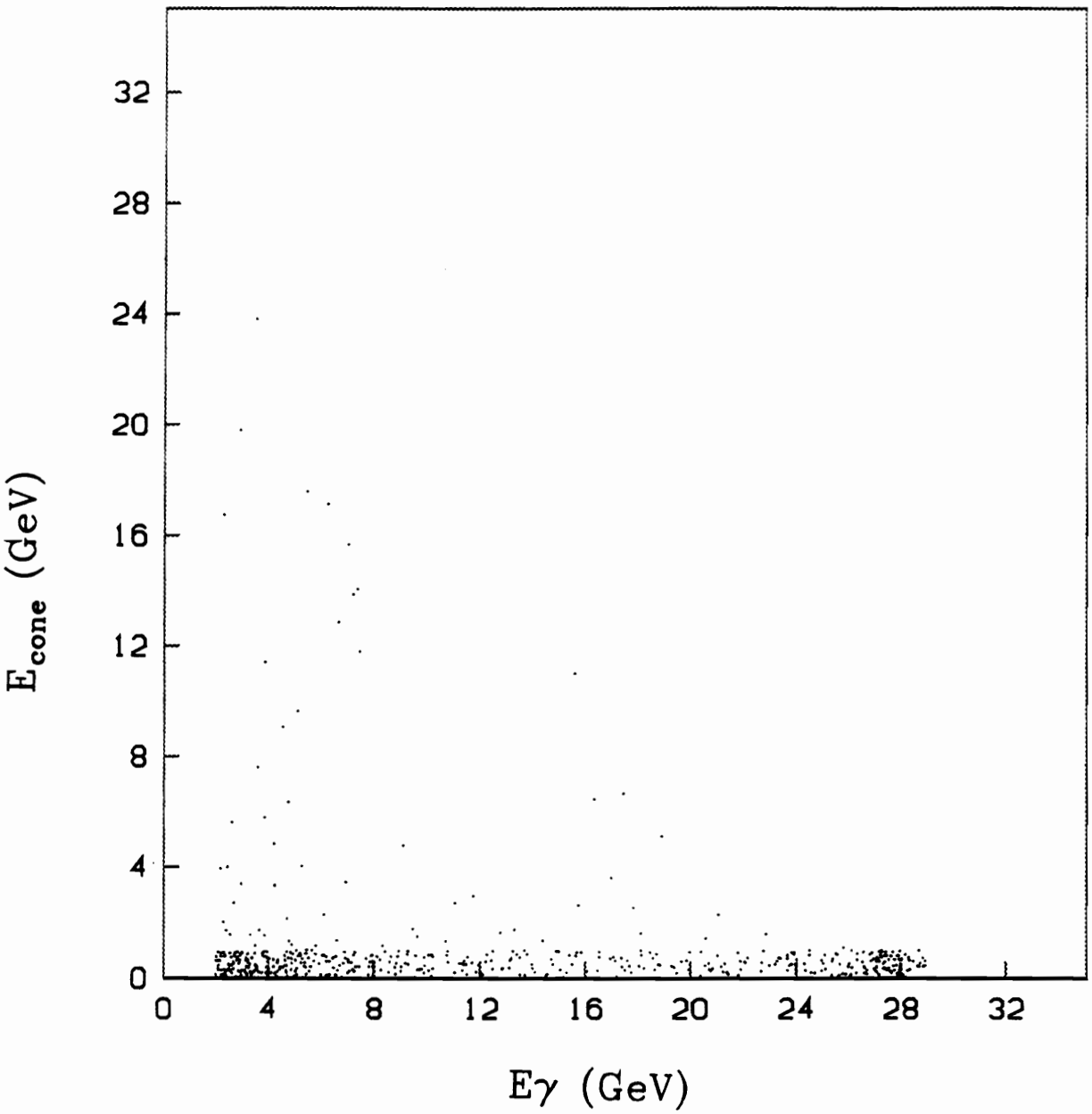

Figure 5-4: Photon energy vs. the cone energy for photons from the initial state radiattion.

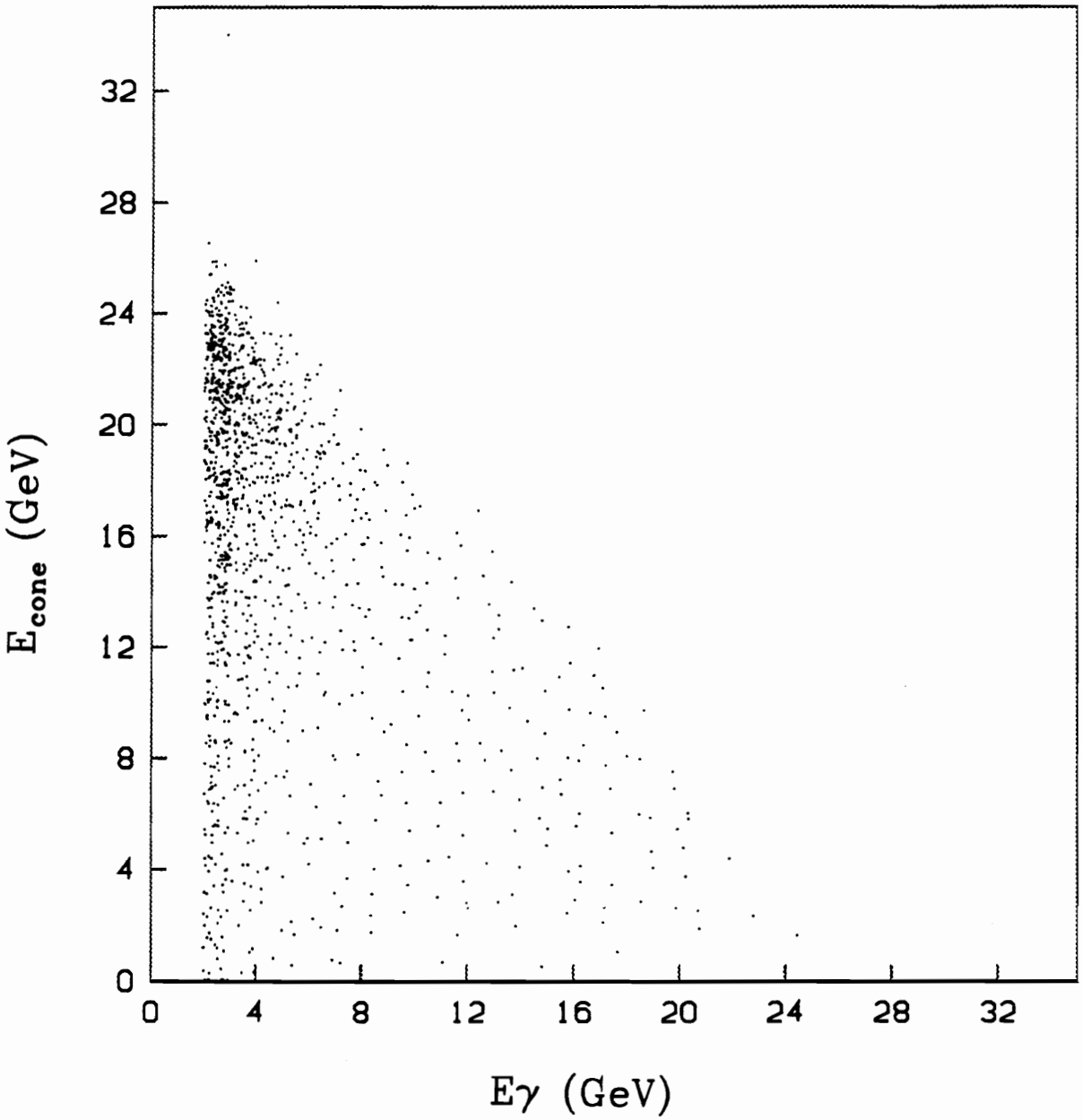

Figure 5-5: Photon energy vs. the cone energy for photons from hadron decays.

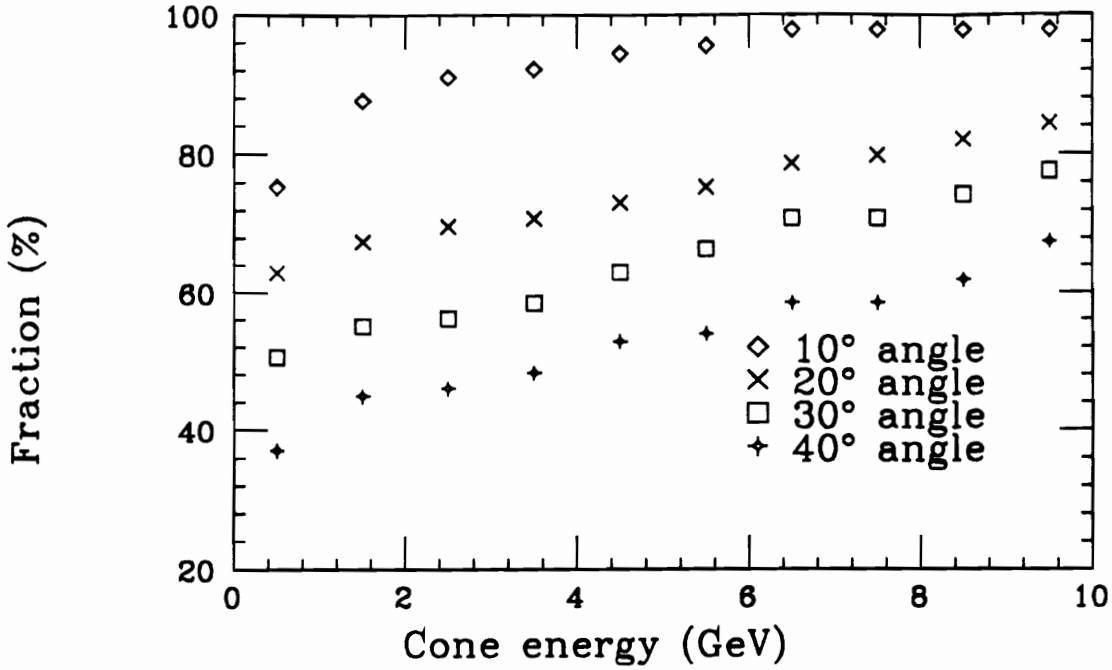

Figure 5-6: Effect of isolation cuts to photons from final state radiation.

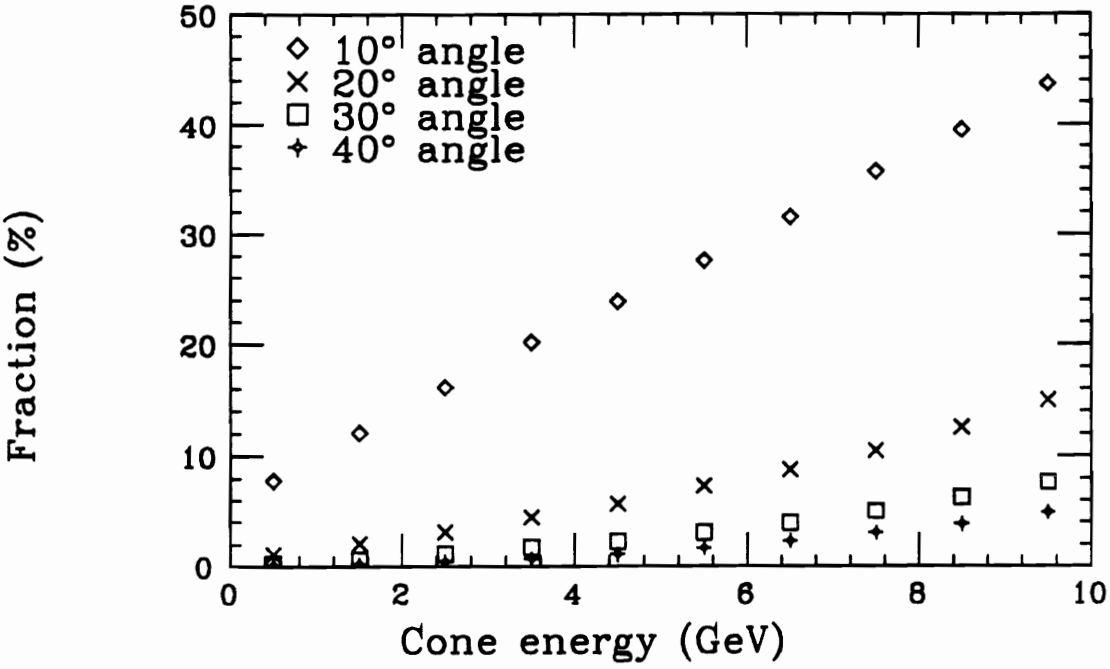

Figure 5-7: Effect of isolation cuts to photons from hadron decays.

A comparison of the isolated photon energy spectra generated by Lund 7.2 with and without final state radiation is shown in Figure 5-8. The solid line is with final state radiation, and the dotted line is without final state radiation. Both histograms here use the generator level MC events. The final state radiation constitutes 22% of the selected isolated photons.

The ratio of the histogram values in each bin without final state radiation to the corresponding values with final state radiation is shown in Figure 5-9.

The comparisons between our data and Lund 7.2 with and without final state radiation are shown in Figure 5-10. The solid histogram corresponding to Lund 7.2 with final state radiation is calculated by using fully simulated Monte Carlo events, while the dotted one corresponding to Lund 7.2 without final state radiation is calculated by using the same fully simulated Monte Carlo events multiplied by the ratio shown in Figure 5-9. As shown in Figure 5-10, the data agree better with the solid histogram. This again confirms our conclusion from the inclusive photon analysis that final state radiation does exist in our data sample. The reason that the integrated data spectrum is about 24% higher than the solid histogram is possibly because the mechanism of Lund 7.2 is not advanced enough in dealing with the calculation of the radiative correction [36]. Three experiments in LEP have observed about 15% more final state photons than the Lund Model predicts (in LEP energy region the final state radiation dominates the radiation processes).

5.1.3 Reconstruction of Quark Axis

After applying the event selection criteria discussed in Section 5.1.1, we assume our event sample consists of events from the $e^+e^- \rightarrow q\bar{q}\gamma$ processes. In the hadronic final states this appears as two hadronic jets plus one energetic isolated photon from the radiative process. The hadronic jets are reconstructed, and a kinematic fitting is performed with the constraint of requiring four-momenta conservation to improve the accuracy of the photon energy and hadronic jet energy determination. The directions and momenta of the hadronic jets are then assigned to be those of the respective primary quarks.

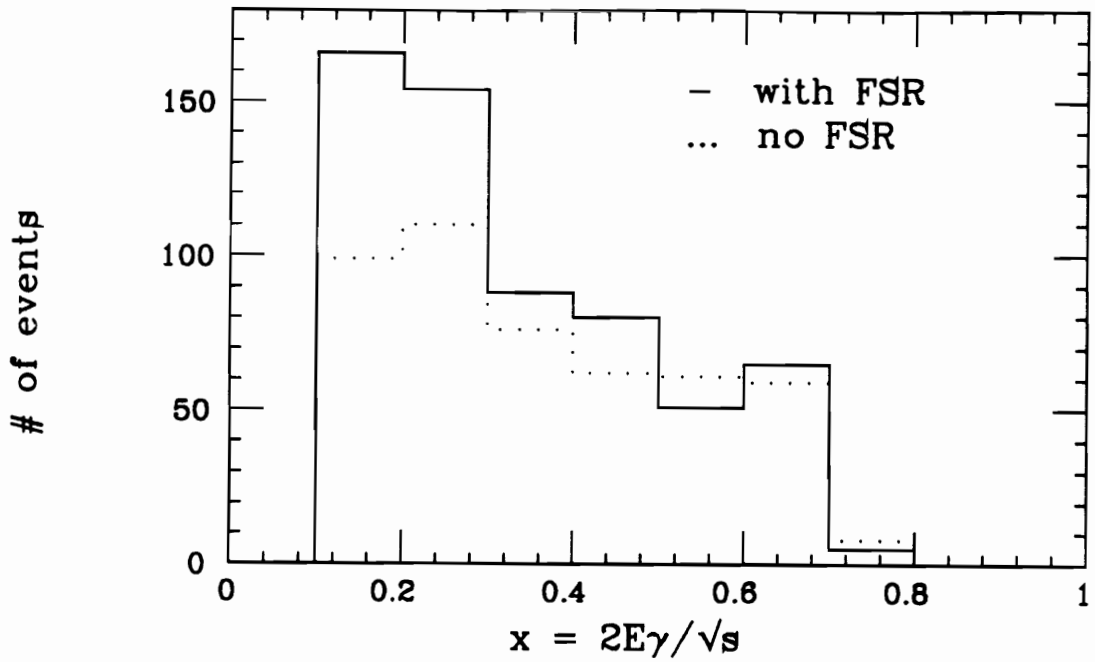

Figure 5-8: Comparison of isolated photon spectrum between Lund 7.2 with and without final state radiation.

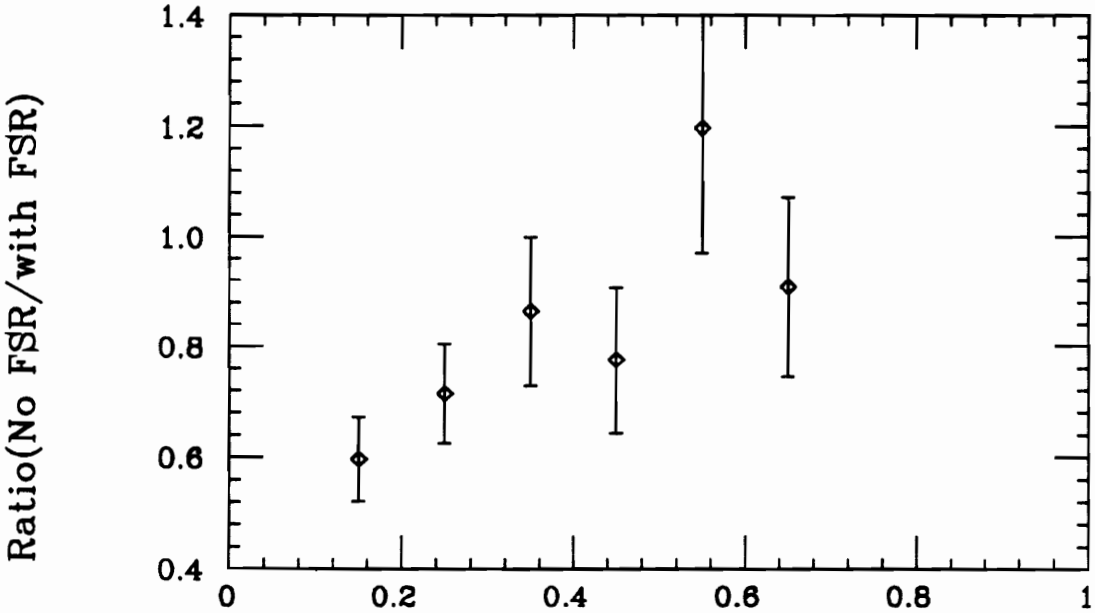

Figure 5-9: Ratio of Lund 7.2 without to with final state radiation.

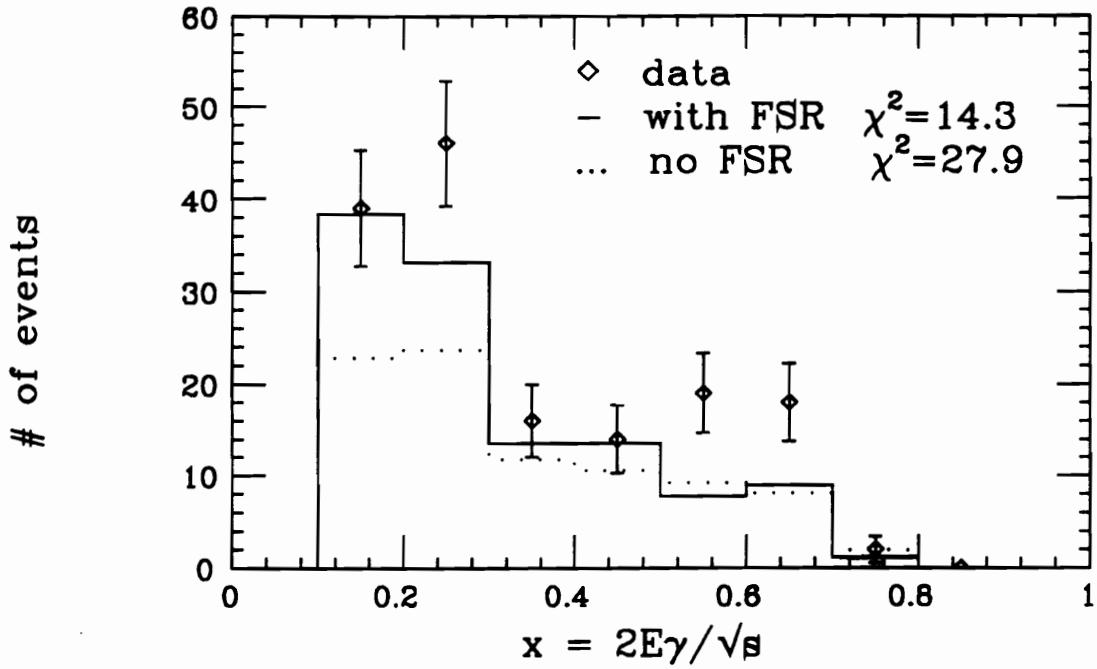

Figure 5-10: Comparison of isolated photon spectrum between data and Lund MC.

First we want to introduce a common shape variable, thrust, which measures the directional uniformity of the distribution of momenta in the event. It is defined as:

$$THR = max(\frac{\sum_i |\vec{P_i} \cdot \hat{n}|}{\sum_i |\vec{P_i}|}) \tag{5.1}$$

where $\vec{P_i}$ is the momentum of the ith particle, and unit vector $\hat{n}$ is chosen to maximize THR. The sum is over both charged and neutral tracks. $\hat{n}$ is defined as the thrust axis. This thrust variable is going to be used in the rest of this analysis.

We assign particles (except the isolated photon) in the hadronic final state to two hadronic jets in the following way. The isolated photon four-momenta vector is used to boost all other particles into the $q\bar{q}$ center-of-mass system, in which the thrust axis is determined. A plane perpendicular to the thrust axis devides the space into two hemispheres. Particles in each hemisphere are combined together into a jet respectively. The system is transfered back to the lab system, and the corresponding jet axes are obtained. Then a kinematic fitting with the constraint requiring the four-momenta conservation is performed, and fitted momenta for the isolated photon and two jets are obtained. In order to be sure that each particle has been assigned to the correct jet, we use the fitted momenta of the isolated photon to repeat the boosting process and check if every particles is assigned to the previously assigned jet. If not, then another round of fitting is performed. This goes on until the jet assignment of each particle is stablized. For most events, one or two round of kinematic fitting will serve this purpose. Events that have bad χ^2 values ($\chi^2 \geq 10$ for 7 degrees of freedom) for the fitting are assumed not having the 3-jet event shape and thus are removed at this stage.

The hadronic jet axes thus determined are compared to the original primary quark directions for Lund MC. Figure 5-11 shows the angle in space between the primary quark direction and reconstructed hadronic jet axis. For more than 85% of the cases, the angular difference is smaller than 10°.

The reconstructed hadronic jet axis is used as the primary quark direction in our charge asymmetry analysis.

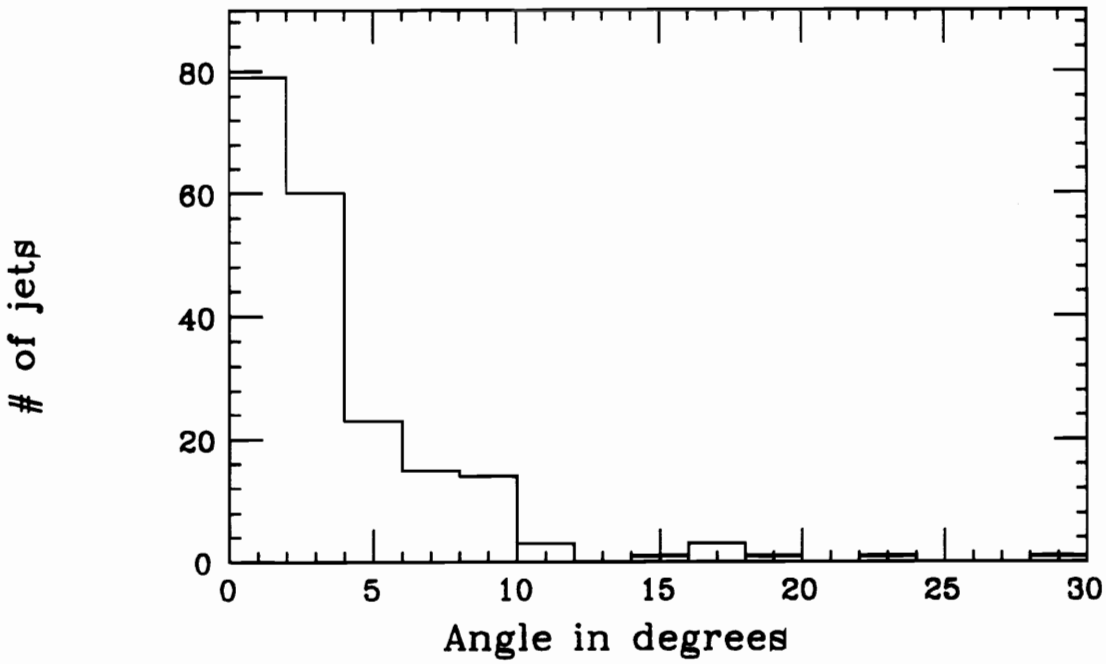

Figure 5-11: Angle between the primary quark direction and the reconstructed jet axis.

5.1.4 Reconstruction of Quark Charge

To determine which one of the two jets originates from the positively charged quark, a jet charge Q_{jet} is determined as following:

$$Q_{jet} = \frac{\sum q_i \, w_i^{\alpha}}{\sum w_i^{\alpha}}$$

where q_i is the charge of the i-th charged particle in this jet, the sum is over all charged particles in the jet, and w_i and α are a physical observable and a weight parameter, respectively. The calculation is done in the $q\,\overline{q}$ system. We calculate Q_{jet} for each jet, then assign a positive sign to the jet having the larger Q_{jet}. As for w_i, we tested the following three observables:

1. Longitudinal momentum observable, which is defined as

$$w_i = \frac{P_{||}^i}{\sum_j P_{||}^j}$$

   where $P_{||}^i$ is the longitudinal momentum of the i-th charged particle with respect to the thrust axis; the sum goes over both charged and neutral particles in the jet.

2. Rapidity observable, which is defined as

$$w_i = \frac{1}{2} \ln(\frac{E^i + P_{||}^i}{E^i - P_{||}^i})$$

   where E^i and $P_{||}^i$ are energy and longitudinal momentum of the i-th charged particle in the jet.

3. Momentum observable, which is defined as

$$w_i = \frac{P^i}{E_{jet}}$$

   where P^i is the absolute value of the momentum of the i-th charged particle in the jet; E_{jet} is the energy of the jet.

Figure 5-12 shows the probability f of correctly identifying the charge of the jet as a function of parameter α for all three charge determining methods. The first and the second method have very similar behavior, and they both peak around $\alpha = 0.4$. Thus we choose to use the first method with $\alpha = 0.4$ for our charge asymmetry analysis. The second method with $\alpha = 1.3$ is also used independently to give us a cross check on our results.

5.1.5 Forward-Backward Charge Asymmetry

The forward-backward charge asymmetry is defined as

$$A = \frac{N_f - N_b}{N_f + N_b} \tag{5.2}$$

where N_f is the number of positively charged jets with an angle smaller than $\pi/2$ relative to the positron beam direction, and N_b is the number of positively charged jets with an angle greater than $\pi/2$ relative to the positron beam direction.

Similarly we define

$$A' = \frac{N'_f - N'_b}{N'_f + N'_b} \tag{5.3}$$

where N'_f is the number of negatively charged jets with an angle smaller than $\pi/2$ relative to the electron beam direction, and N'_b is the number of negatively charged jets with an angle greater than $\pi/2$ relative to the electron beam direction.

The angular distribution of the positive jets with respect to the positron beam direction of the data is shown in Figure 5-13. Also shown in the same figure are the theoretical predictions of Lund MC and FKS MC (see Section 3.2.1) (all calculated by the charge determining method 1). The Lund MC histogram is calculated with the fully simulated Lund Monte Carlo events. The FKS MC histogram is calculated with the fully simulated MC events containing photons from radiative processes generated by FKS generator, plus the fully simulated MC events containing photons from fragmentation processes generated

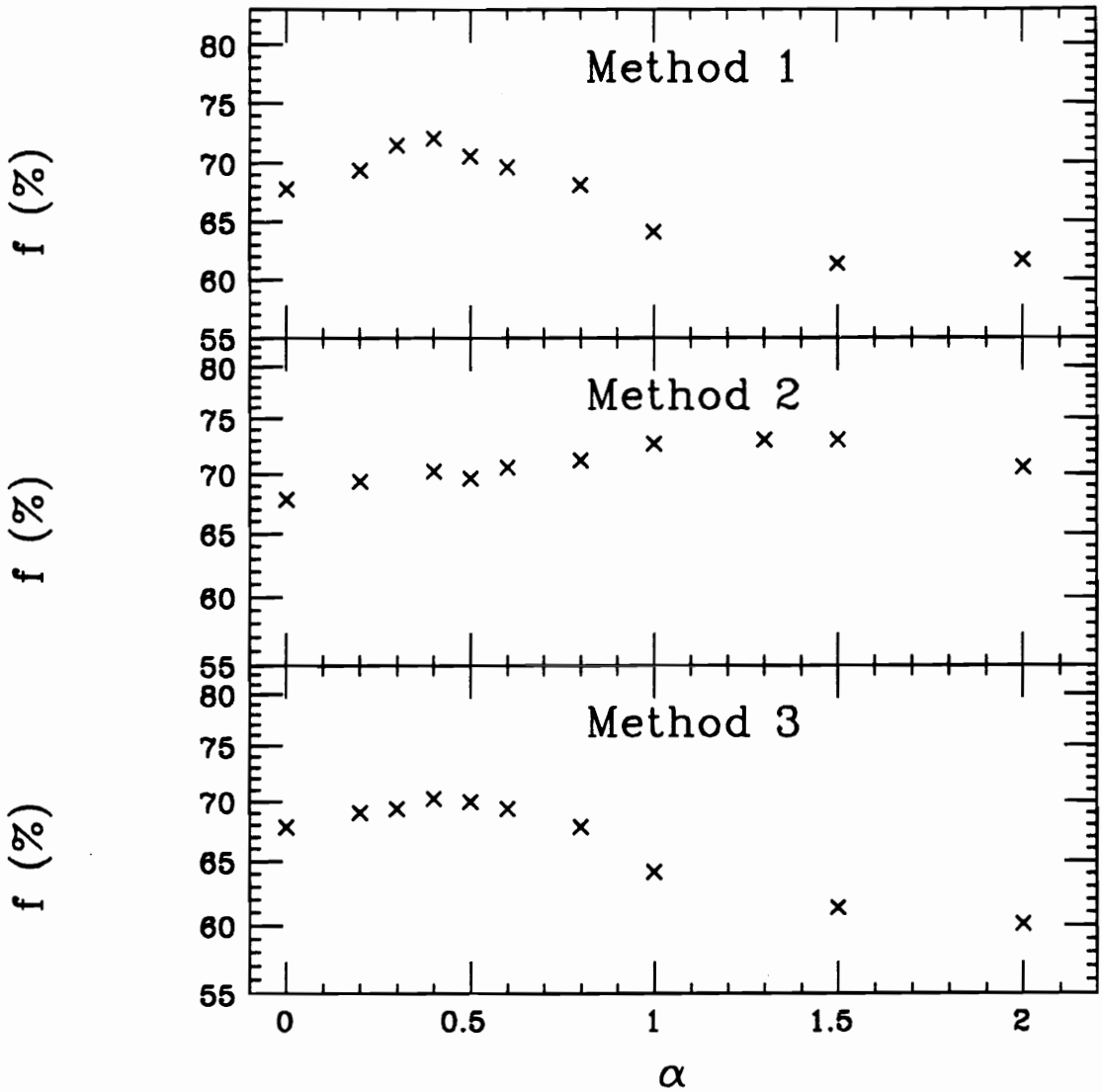

Figure 5-12: Probability f for different α.

by Lund generator. The similar plot for the negative jets with respect to the electron beam direction is shown in Figure 5-14.

The charge asymmetry values A and A' calculated according to Equation 5.2 and Equation 5.3 for data and MC are listed in Table 5-2, where the results calculated using the both method 1 and 2 of charge determination are shown. Only statistical errors are included.

Since Lund 7.2 MC does not include the interference term between the initial state and final state radiation (see Section 3.2.1), we believe the charge asymmetry value predicted by FKS MC (which does include full QED corrections) is more reliable. As shown in Table 5-2, the charge asymmetry measured for our data is null within its error, but does not disagree with the FKS MC prediction due to the large errors. We need more data for a conclusive result.

The results of several other experiments [21], together with the AMY result are listed in Table 5-3.

5.2 New Particle Search through Isolated Photon Event

A process like $e^+e^- \rightarrow \gamma + H^\circ$ could give additional isolated photon events, where H° is a unknown heavy neutral particle (such as a scalar neutral Higgs particle). Because of the law of momentum and energy conservation, a process like this will have an energetic isolated photon recoiling against the heavy neutral particle. If indeed this process occurs, the isolated photon will have a monochromatic energy spectrum, or equivalently we will see a peak above the background in the recoil mass spectrum. We will first describe the event selection criteria, and then show the recoil mass spectrum for our data. Finally we will extract upper limits for the production cross section of the H° for a range of the H° mass.

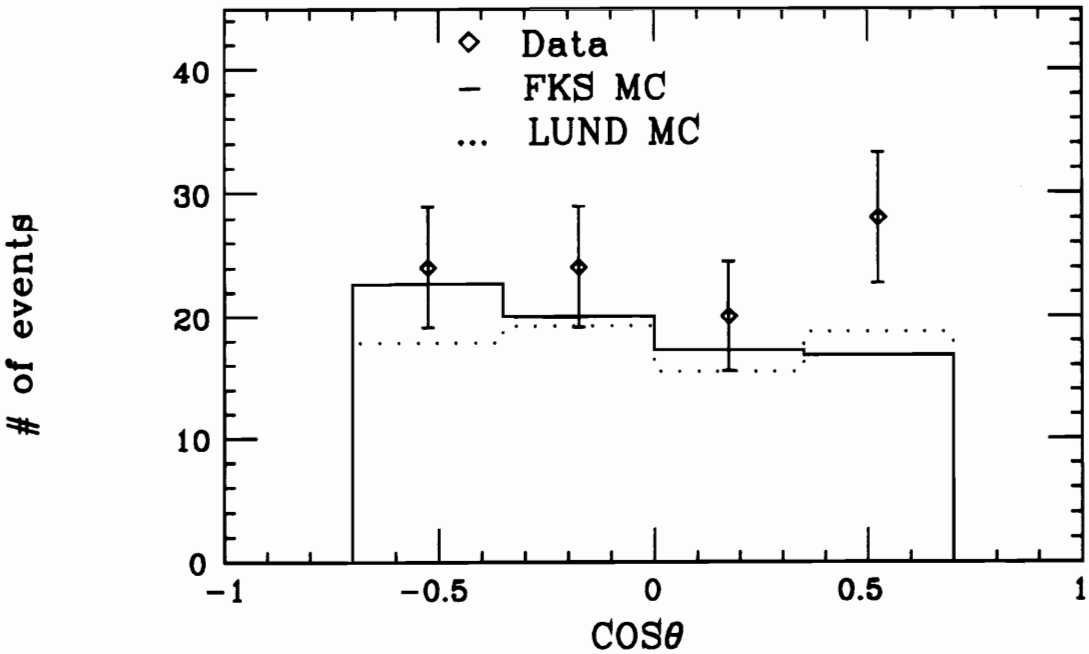

Figure 5-13: Angular distribution of positive jets of data and MC with respect to the positron beam direction.

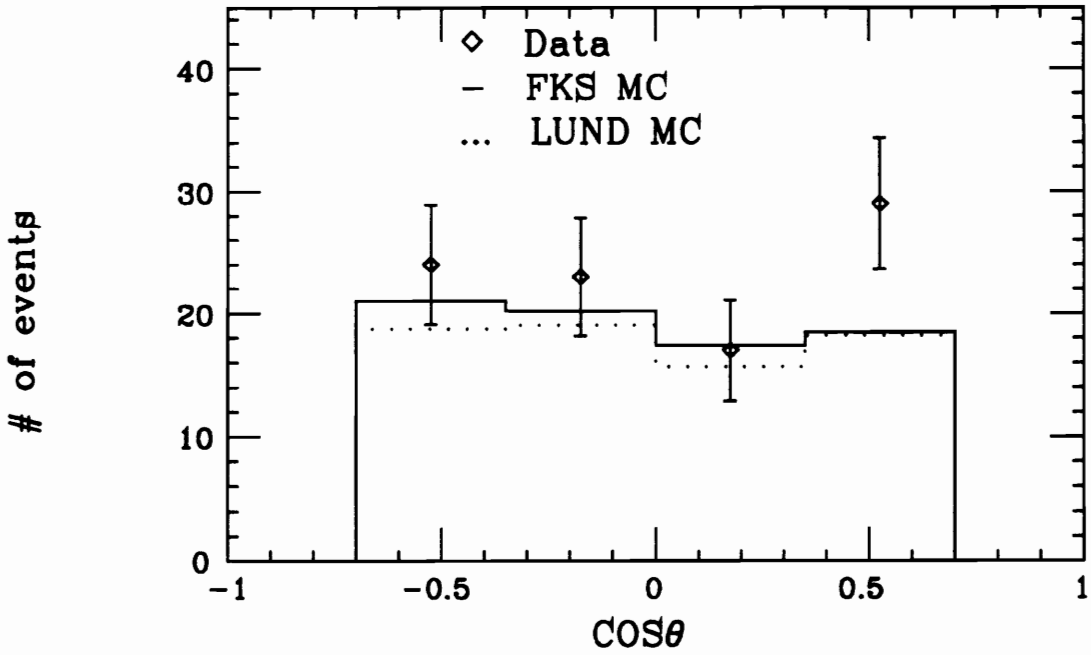

Figure 5-14: Angular distribution of negative jets of data and MC with respect to the electron beam direction.

Table 5-2: Charge asymmetry values.

	Charge	A	A'
Data	Method 1	0.000 ± 0.102	-0.011 ± 0.104
	Method 2	0.063 ± 0.102	0.054 ± 0.104
FKS MC	Method 1	-0.112 ± 0.039	-0.070 ± 0.039
	Method 2	-0.070 ± 0.039	-0.028 ± 0.039
Lund MC	Method 1	-0.041 ± 0.049	-0.055 ± 0.049
	Method 2	-0.012 ± 0.049	-0.026 ± 0.049

Table 5-3: Comparison of charge asymmetry values with other experiments.

Experiment	A data	A MC
MAC(1985) $\sqrt{s}$=29 GeV	-0.123 ± 0.035	-0.117 ± 0.026
JADE(1985) $\sqrt{s}$=34 GeV	-0.06 ± 0.07	-0.14 ± 0.05
MARK II(1986) $\sqrt{s}$=29 GeV	-0.246 ± 0.055	-0.23 ± 0.06
TASSO(1988) $\sqrt{s}$=14–34 GeV	-0.32 ± 0.07	-0.153 ± 0.011
JADE(1989) $\sqrt{s}$=35–44 GeV	-0.141 ± 0.041	-0.122 ± 0.014
AMY(1991) $\sqrt{s}$=57.3 GeV	0.000 ± 0.102	-0.112 ± 0.039

5.2.1 Event Selection

The event selection criteria are developed by comparing the Higgs-gamma Monte Carlo events (Section 3.2.1), which is our signal in this analysis, with the Lund 7.2 five-flavor Monte Carlo events, being the background. The criteria are such as to keep the maximum number of signal events, while eliminating the maximum number of background events.

We start with the photon energy cut. The photon energy spectra above 2 GeV for $H^\circ\,\gamma$ Monte Carlo ($M_{H^\circ} = 25$ and 40 GeV) and Lund 7.2 Monte Carlo are shown in Figure 5-15 a, b and c, respectively . After careful comparison we decide to put a photon energy cut $x \geq 0.32$, where $x = 2\,E_\gamma/\sqrt{s}$.

The isolation cuts are defined the same as those in Section 5.1.1 (see Figure 5-2). Figure 5-16 and Figure 5-17 show the effect of different combinations of half cone angle and cone energy cuts, for $H^\circ\,\gamma$ MC and Lund MC respectively. The vertical axis is the fraction of events selected if a certain cone angle and cone energy cut are chosen. Figure 5-18 shows the ratio

$$Fraction(H^\circ\,\gamma)/\sqrt{Fraction(Lund72)}$$

for the $M_{H^\circ} = 40$ GeV case, where *Fraction* is shown in Figure 5-16 and Figure 5-17. The numerator is the fraction of the signal, and the denominator is proportional to the error bar of the signal. The maximum value of this curve should correspond to the best choice of cone angle and cone energy cuts for the purpose of maximizing the signal and minimizing the error bars of the signal. After careful comparison between Figure 5-16, Figure 5-17 and Figure 5-18, we decide to use 20° cone angle and 2 GeV cone energy cut.

Besides the isolation cuts, we also require the thrust axis (as defined in Equation 5.1) of isolated photon events within $|cos\theta| \leq 0.73$, to assure that most momenta of the event fall within the SHC fiducial region.

Here is a summary of the selection criteria for Higgs production events:

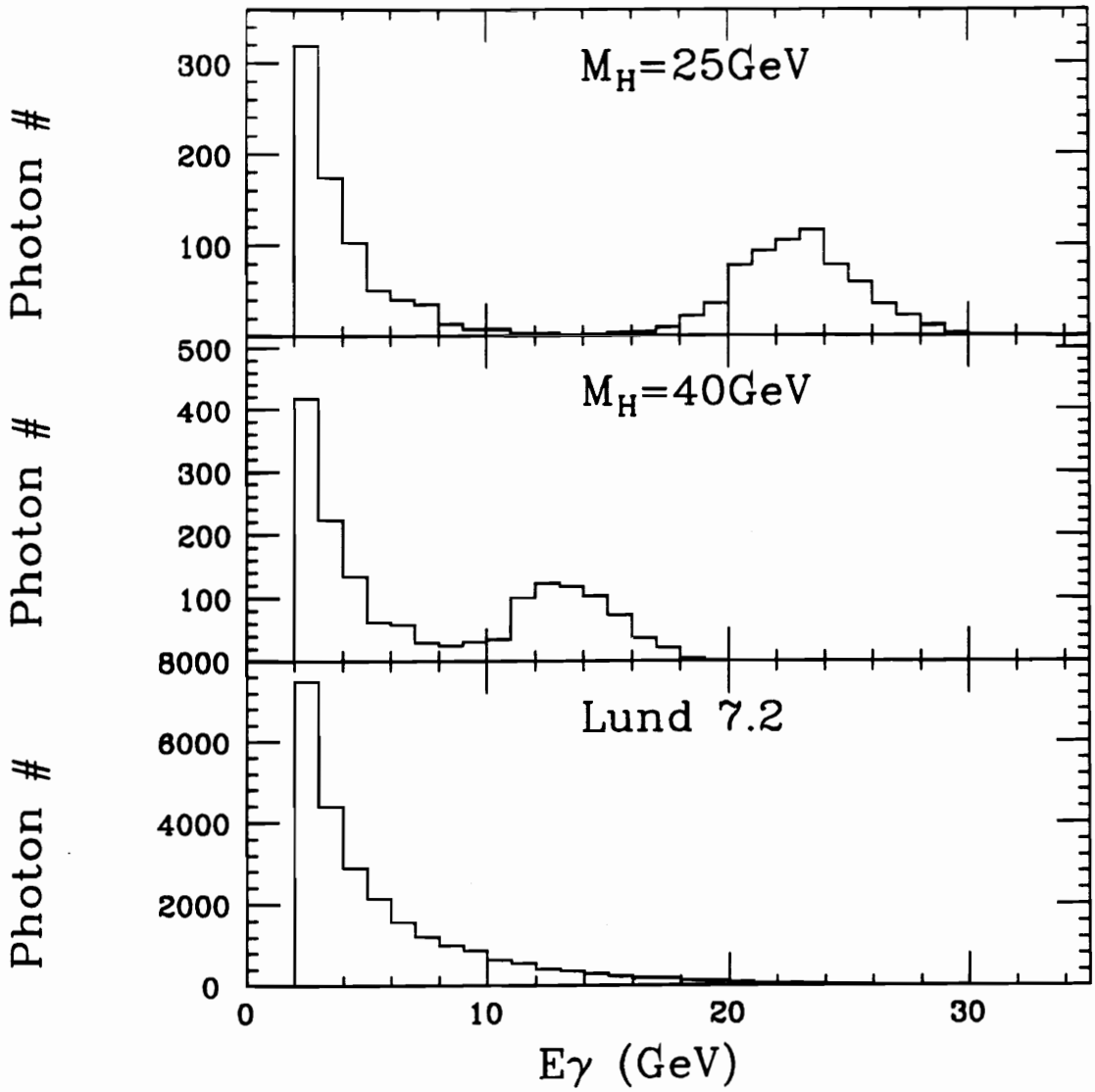

Figure 5-15: Photon energy spectrum for Higgs-gamma MC (a,b) and Lund MC (c).

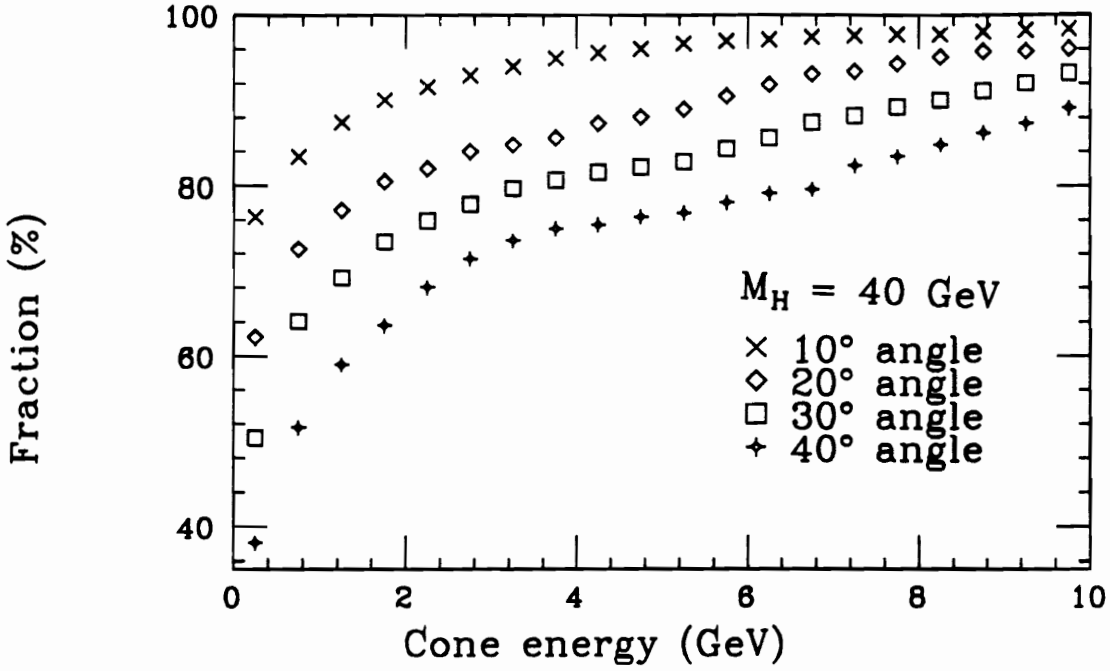

Figure 5-16: Effect of different isolation cuts for Higgs-gamma MC.

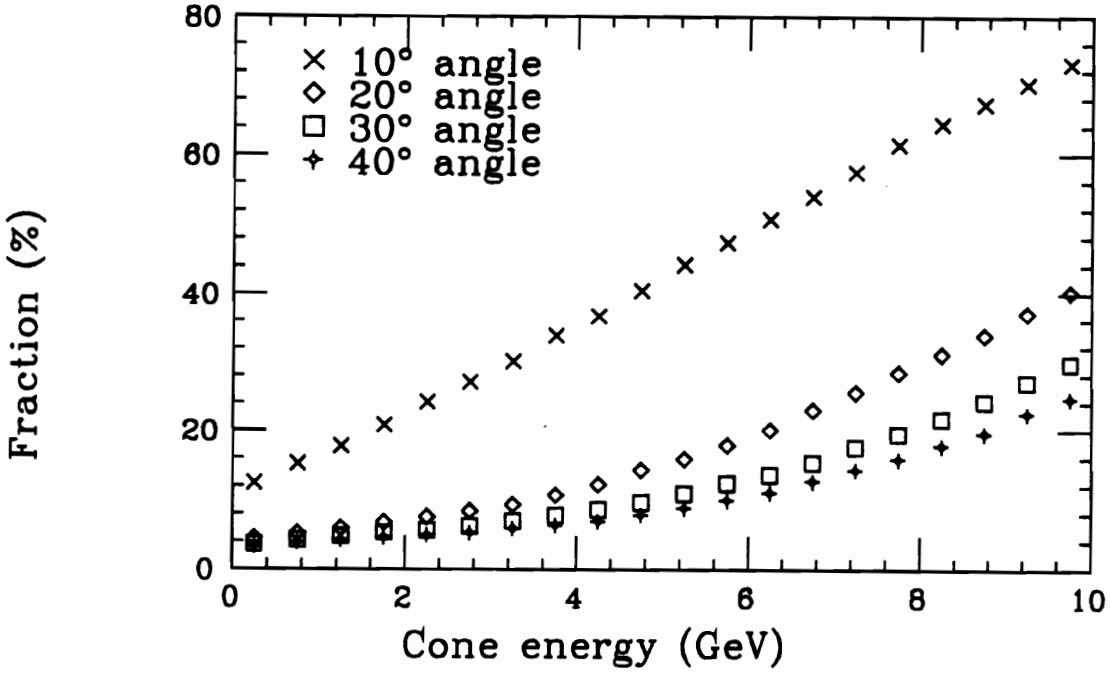

Figure 5-17: Effect of different isolation cuts for Lund MC.

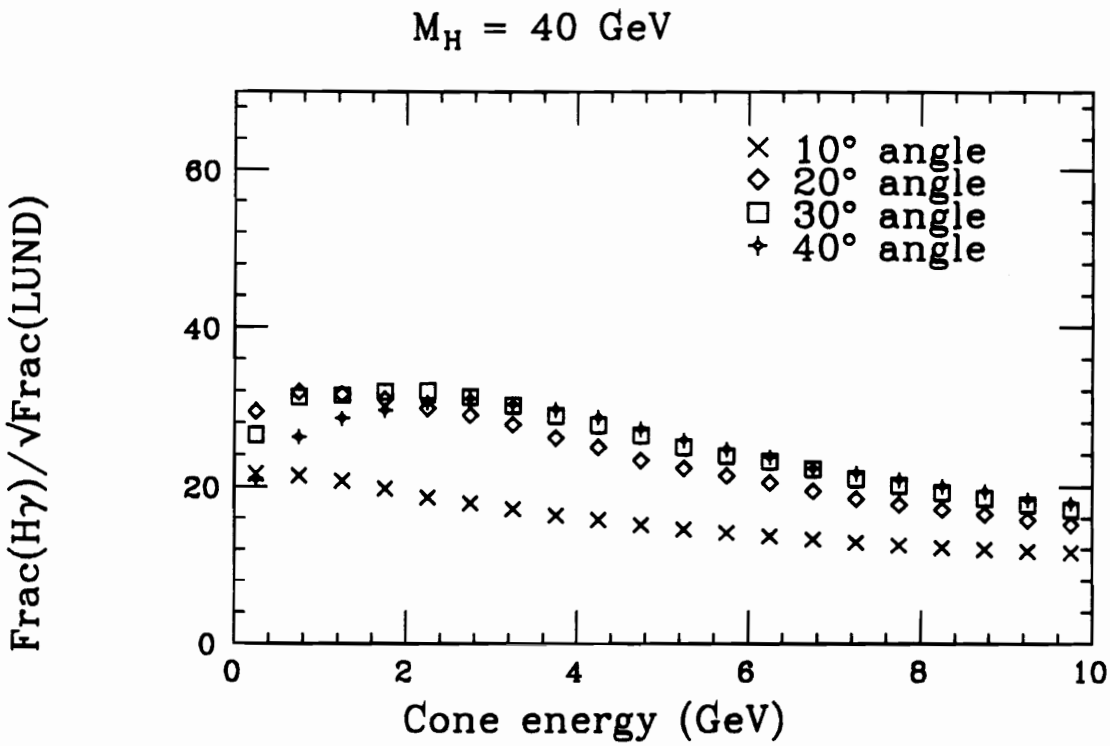

Figure 5-18: Signal to error bar ratio for different isolation cuts.

1. Photon energy cut: $x \geq 0.32$, where $x = 2\,E_\gamma/\sqrt{s}$.

2. Isolation cut: additional energy (both neutral and charged) deposited in a 20° half opening angle cone around the selected photon should be less than 2 GeV.

3. Thrust axis of the event satisfies $|cos\theta_{THR}| \leq 0.73$.

The efficiency for the above selection criteria for different M_{H° is shown in Table 5-4. It is clear that this analysis is sensitive only to the region of $M_{H^\circ} \leq 40$ GeV.

5.2.2 Recoil Mass Spectrum of the Isolated Photon Events

Now we proceed with the study of the isolated photon events. As indicated in Section 1.2.3, if $e^+e^- \rightarrow \gamma + H^\circ$ does occur, then H° will decay into a $q\,\overline{q}$ pair. Thus the final state for this process is a 3-jet event, *i.e.* one isolated photon plus 2 hadronic jets. By using this 3-jet property, and the constraint of 4-momenta conservation in the hadronic final state, we perform a kinematic fitting to improve the resolution of the recoil mass spectrum of our signal, $H^\circ\gamma$ MC. Then the recoil mass spectrum for AMY data is presented, after applying the same kinematic fitting to enhance any signal events which might possibly exist.

We assign particles in an isolated photon event to 2 hadronic jets in the following way (with the isolated photon itself forming the third jet). The isolated photon four-momenta vector is used to boost all other particles into the $q\,\overline{q}$ center-of-mass system, in which the thrust axis is determined. A plane perpendicular to the thrust axis divides the space into two hemispheres. Particles in each hemisphere are combined together into a jet, respectively. The system is transfered back to the lab system, and the corresponding jet axis direction is obtained. Then a kinematic fitting with constraints requiring four-momenta conservation is performed, and fitted momenta for isolated photon and 2 jets are obtained. Events that have bad χ^2 values ($\chi^2 \geq 10$) for the fitting are assumed not to have the 3-jet event shape and are thus removed at this stage. Figure 5-19 shows the scatter plot of isolated photon

Table 5-4: Efficiency of the selection criteria for new particle search

Events passing cut(s)	M_H 15 GeV	M_H 25 GeV	M_H 30 GeV	M_H 40 GeV	M_H 50 GeV	Data
No cuts	1000	1000	1000	1000	1000	–
AMY hadronic cuts	719	754	749	813	805	4260
$x \geq 0.32$	639	681	643	609	111	1147
Isolation cut	621	667	611	520	8	133

energy before fitting vs. after fitting for $H^\circ\,\gamma$ MC, and Figure 5-20 is the same plot for data.

The recoil mass M_{rec} of an isolated photon event is defined as

$$M_{rec} = \sqrt{(\sqrt{s} - E_\gamma)^2 - E_\gamma{}^2}$$

and invariant mass M_{inv} is defined as

$$M_{inv} = \sqrt{(E_{j1} + E_{j2})^2 - (\vec{P}_{j1} + \vec{P}_{j2})^2}$$

where E_γ is the energy of the isolated photon, and E_{ji} and $\vec{P}_{ji}$ (i=1,2) are the energy and momenta of the ith hadronic jet. Figure 5-21 shows the recoil mass spectra for $H^\circ\,\gamma$ MC (M_{H° = 25 GeV) before fitting and after fitting. Figure 5-22 shows the invariant mass spectra for the same MC before fitting and after fitting. Fitting has not only improved resolution for both M_{rec} and M_{inv}, but also centered the peak at the correct mass values (25 GeV in this case). The same is true for other M_{H° values in the region of 15–40 GeV.

For an ideal event (an event which satisfies 4-momenta conservation), we have $M_{rec} = M_{inv}$. Since the fitting requires 4-momenta conservation, our fitted recoil mass always equals the fitted invariant mass. Thus in the rest of this analysis, we choose to use the fitted M_{rec}. Figure 5-23 shows the recoil mass spectrum for our data after going through the same kinamatic fitting. As seen in this figure, the spectrum is rather flat, and there is no visible peak sitting on top of the background.

5.2.3 Upper Limits on the New Process Cross Sections

We compare the recoil mass spectrum of the data to those of Lund 7.2 MC and $H^\circ\gamma$ MC to determine if there is evidence for the new process $e^+e^- \rightarrow \gamma + H^\circ$ or not. If not, we proceed to extract the upper limit of the cross sections for this new process.

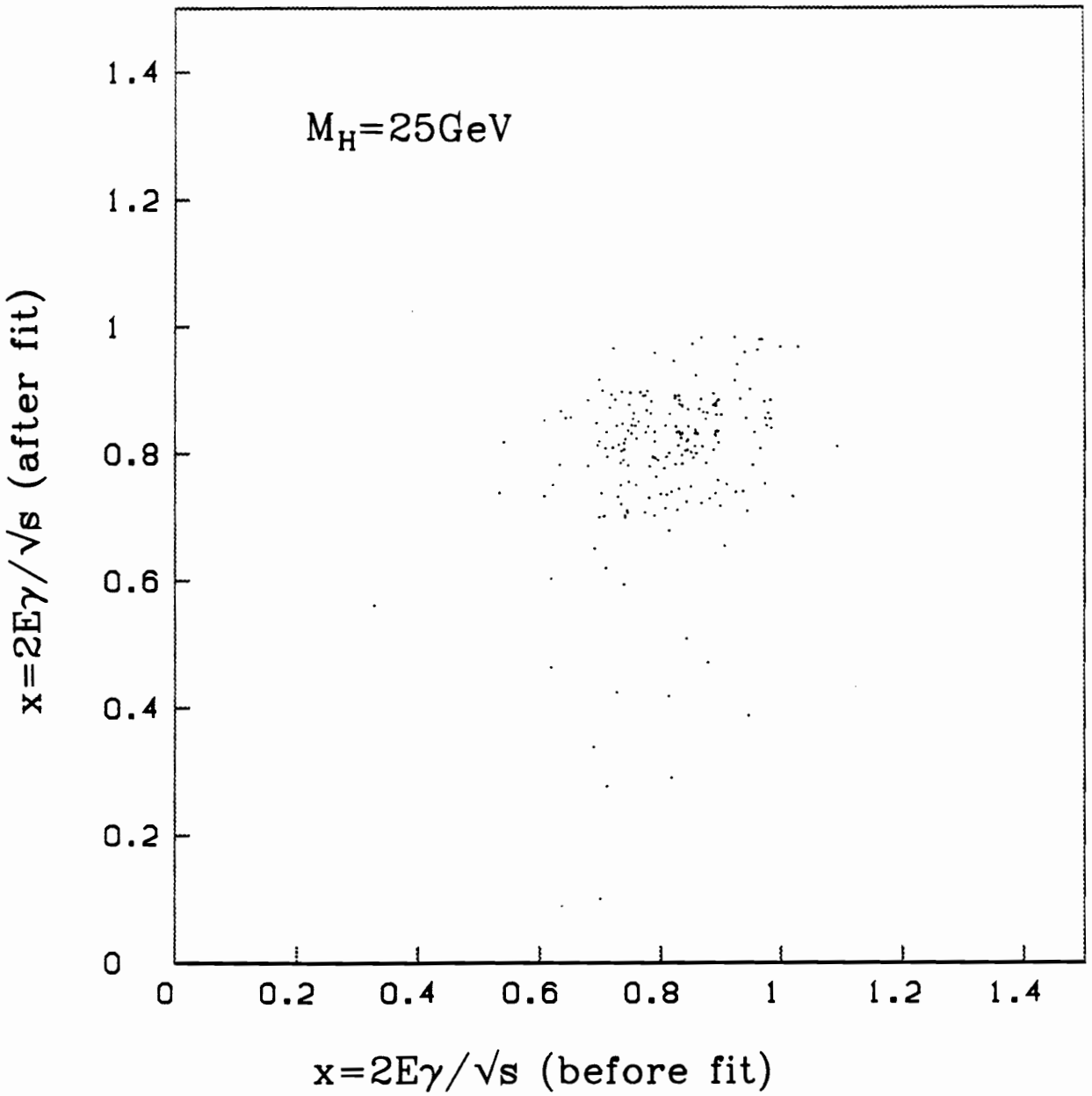

Figure 5-19: Isolated photon energy before fitting vs. after fitting for Higgs-gamma MC.

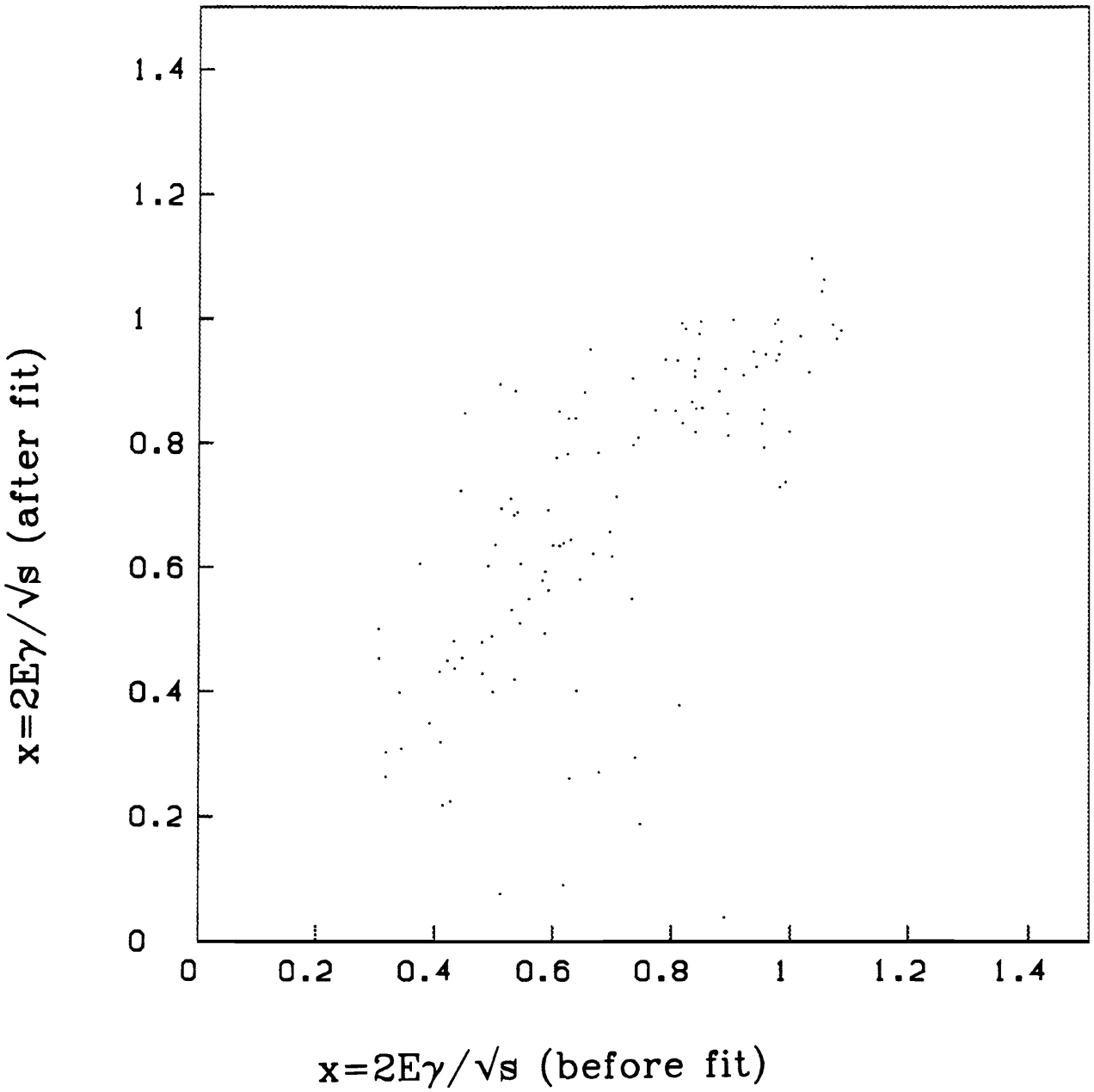

Figure 5-20: Isolated photon energy before fitting vs. after fitting for data.

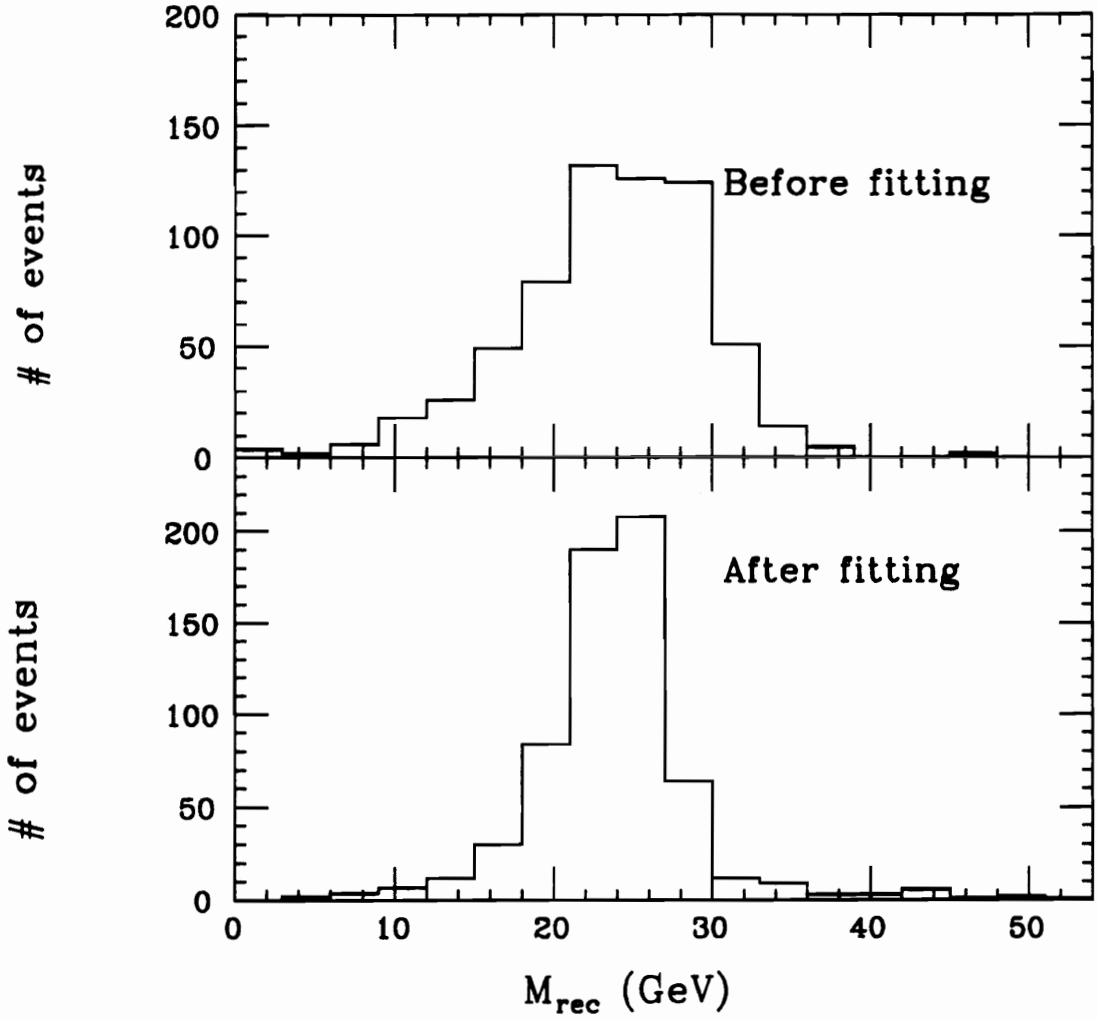

Figure 5-21: Recoil mass spectra for Higgs-gamma MC (M_{H°=25 GeV).

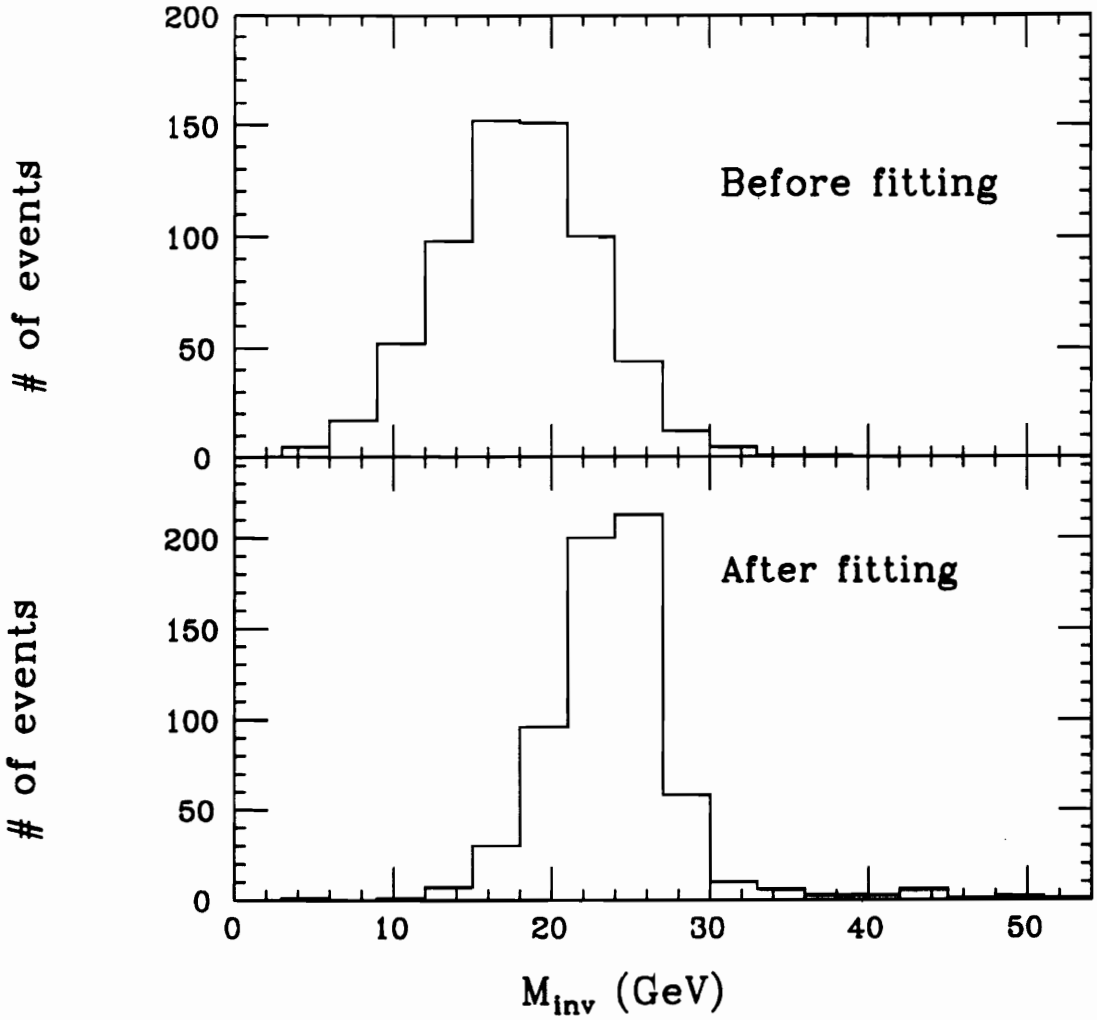

Figure 5-22: Invariant mass spectra for Higgs-gamma MC (M_{H°=25 GeV).

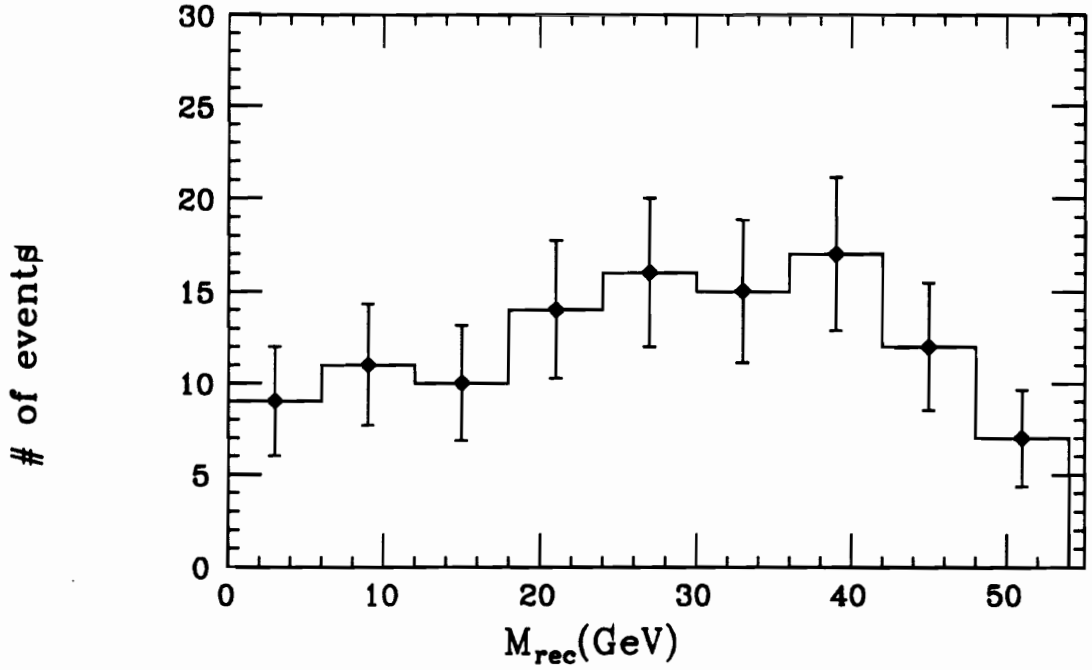

Figure 5-23: Recoil mass spectrum for data after kinematic fitting.

A comparison of the recoil mass spectrum of the data to those of Lund MC is shown in Figure 5-24. The data have basically the same shape as the theoretical prediction, *i.e.* Lund MC. The χ^2 value here is 9.92 for 9 degrees of freedom, because in most of the regions data are slightly higher than the Lund MC prediction. There are three possible reasons for this. One is that because our data sample is small, the statistical fluctuations are rather large. The second reason, probably the most important, is that Lund MC may not be able to describe the photon radiative corrections adequately; three LEP experiments have seen a discrepancy between their data and what Lund 7.2 predicted, in all the cases the Lund program gives about 15% fewer radiative photons than observed experimently [36]. The third reason is that the new process $e^+e^- \rightarrow \gamma + H^\circ$ does occur in our data. This possibility is very unlikely, because if the new process occurs, then the extra events should concentrate in one narrow mass region, not widely spread out like what we observe. Nevertheless the combination of all three of these may be the real situation, in which case we can still set limits for the H° production cross section.

A maximum likelihood fitting is performed to our data in order to extract the upper limits of the cross sections for the new process $e^+e^- \rightarrow \gamma + H^\circ$.

We compute the probability of each event being due to either $e^+e^- \rightarrow$ ***hadrons*** or $e^+e^- \rightarrow \gamma + H^\circ$. The likelihood function is defined as

$$\mathcal{L}(\alpha) = \prod_i^N [\frac{(1-\alpha)\, P_{had}(M_i) \; + \; \alpha\, P_{H\gamma}(M_i,\, M_H)}{P_{had}(M_i)}]$$

where α is the fraction of events in our data which comes from $e^+e^- \rightarrow \gamma + H^\circ$, N is the total number of events, $P_{had}(M_i)$ is the probability for an event coming from $e^+e^- \rightarrow$ ***hadrons*** to have a recoil mass value M_i, and $P_{H\gamma}(M_i,\, M_H)$ the probability for an event coming from $e^+e^- \rightarrow \gamma + H^\circ$ to have a recoil mass value M_i if the H° has a mass M_H.

The probability distribution $P_{had}(M_i)$ is calculated from Lund 7.2 MC as shown in Figure 5-25, where a polynomial fitting is done to the histogram to get a smooth distribution. After

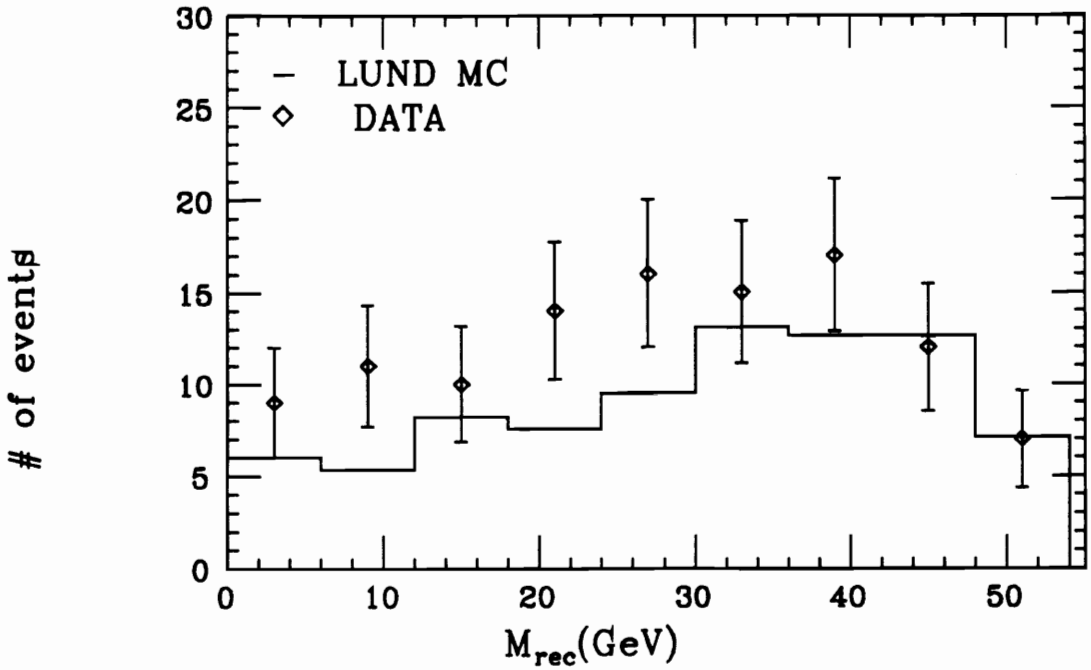

Figure 5-24: Recoil mass spectrum comparison between data and Lund MC.

renomalization, we have

$$P_{had}(M_i) = \frac{1}{A}(25.36 + 0.357M_i - 0.0472M_i^2 + 0.00389M_i^3 - 0.00006M_i^4)$$

where A is the nomalization constant.

The probability distribution $P_{H\gamma}(M_i, M_H)$ comes from $H^\circ\gamma$ MC as shown in Figure 5-26, where a gaussian fit is performed to the M_{rec} histogram. After renomalization, we have

$$P_{H\gamma}(M_i, M_H) = \frac{1}{\sqrt{2\pi s^2}} \exp[-\frac{(M_i - M_H)^2}{2s^2}]$$

where s is the parameter that characterises the width of the distribution, and M_H is the center of the distribution. The parameter s is primarily determined by the SHC energy resolution and Figure 5-27 shows s as a function of H° mass M_H.

Likelihood $\mathcal{L}$ as a function of αN, *i.e.* number of events from the $e^+e^- \rightarrow \gamma + H^\circ$ process, is shown in Figure 5-28 for $M_H = 35$ GeV. The dotted line gives us the 95% confidence level (C.L.) upper limit for the number of events from the new process for this M_H value.

The 95% C.L. upper limit for the number of new process events (we call it N_{up}) can be converted to 95% C.L. upper limit for the production cross section (we call it σ_{up}) as the following:

$$\sigma_{up}(M_H) = \frac{N_{gen}(M_H)}{L_{data}\, N_{pass}(M_H)} N_{up}(M_H)$$

where $N_{gen}(M_H)$ is the number of generated events for Higgs mass M_H, L_{data} is the integrated luminosity for the data, and $N_{pass}(M_H)$ is the number of $H^\circ\gamma$ MC events (with M_H) which pass all the event selection cuts.

The upper limit for the cross sections as a function of Higgs mass M_H is shown in Figure 5-29; also shown are the limits obtained by JADE experiment [17] for the same new process search. The region above the curves are excluded with 95% confidence level. Our results have significantly extended the previous JADE limits in a much wider H° mass region.

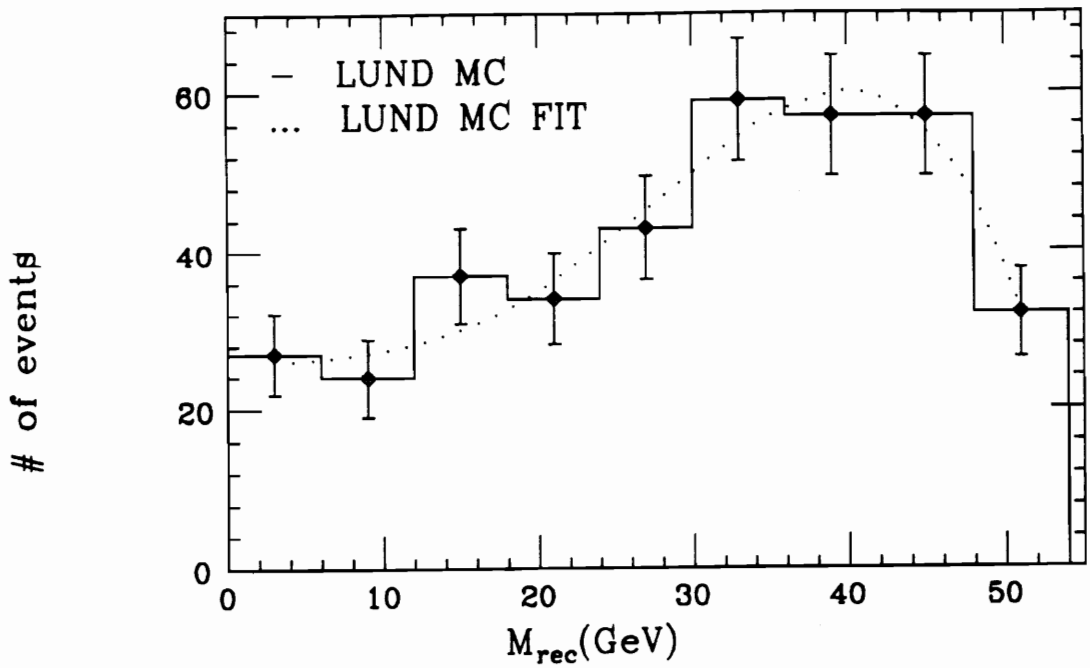

Figure 5-25: Probability distribution for hadronic process.

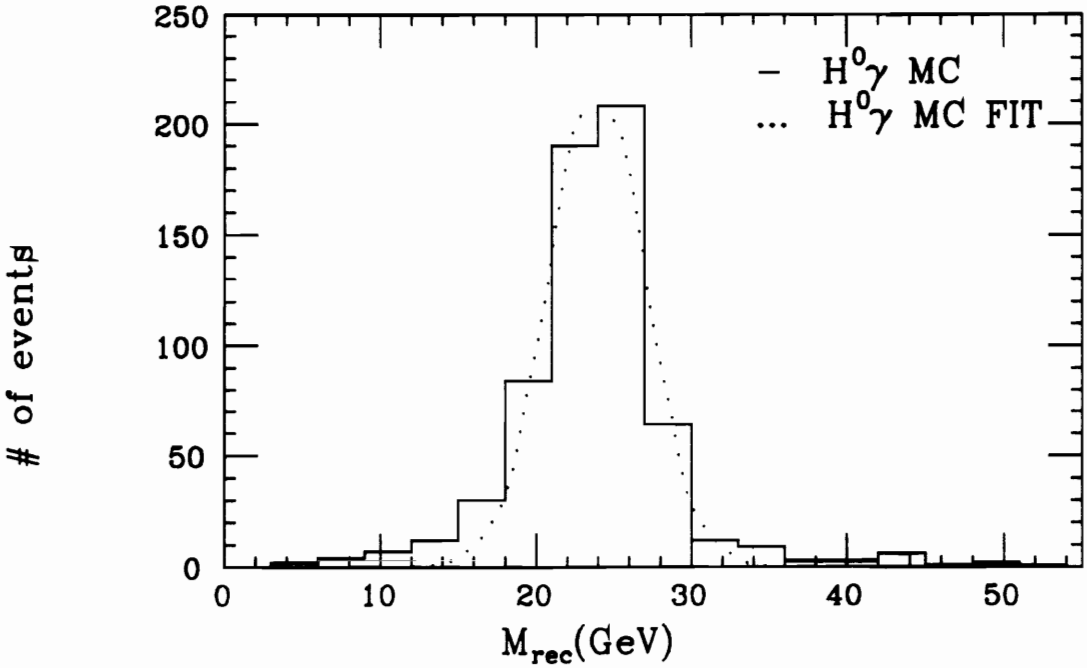

Figure 5-26: Probability distribution for Higgs-gamma process (M_H=25 GeV).

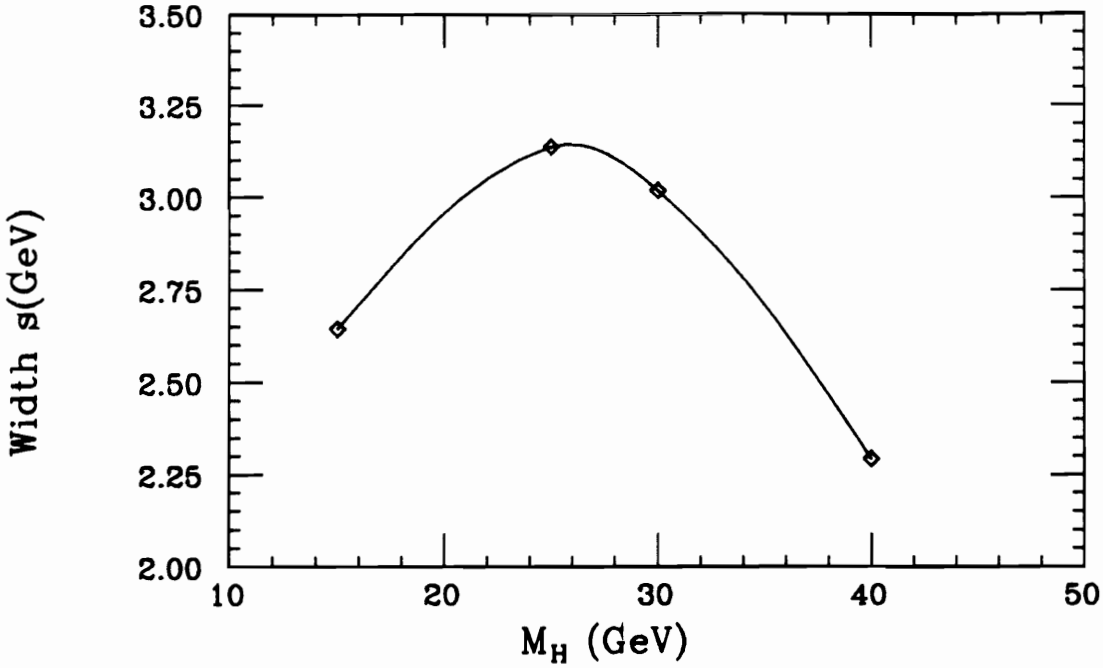

Figure 5-27: Width s of gaussian distribution as a function of Higgs mass.

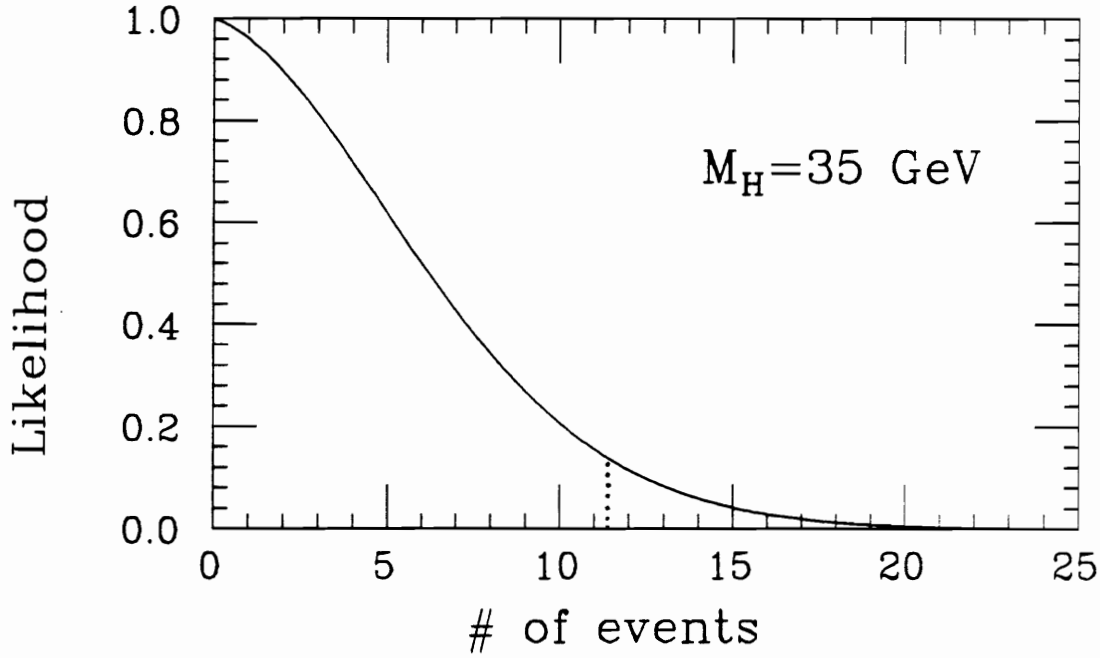

Figure 5-28: Likelihood as a function of number of new process events.

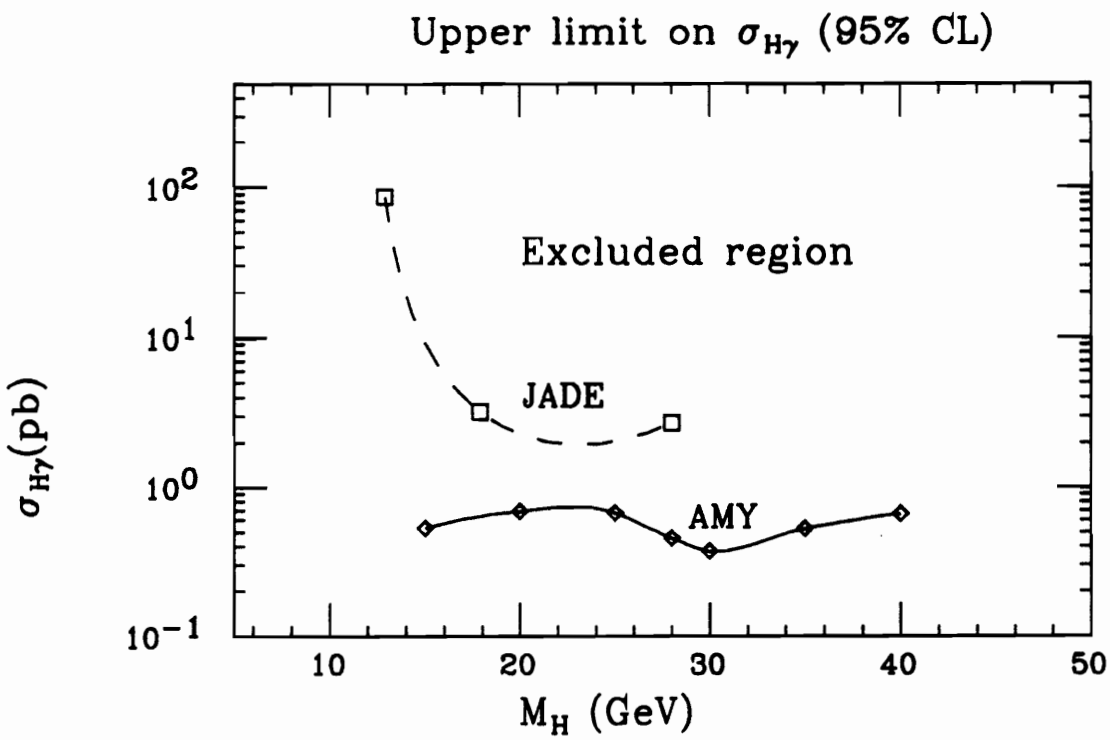

Figure 5-29: Upper limit of the new process cross sections as a function of Higgs mass.

Chapter 6

Conclusions

In the first part of this thesis we presented a study of inclusive photon production in hadronic final states. The inclusive photon cross sections have been measured and are found to scale with the center-of-mass energies $\sqrt{s}$ as a function of Feynman variable $x = 2\,E_\gamma/\sqrt{s}$. Our inclusive photon cross sections also agree with those measured previously by the JADE experiment at $\sqrt{s} = 34$ GeV. The existence of final state radiation has been determined by comparing our inclusive photon cross sections at $\sqrt{s} = 56$, 57, and 58 GeV with the theoretical prediction. The Lund Monte Carlo program (in which the string fragmentation model is used) has been found to describe our data reasonably well for the photons from the fragmentation process.

In the second part of this thesis a study of isolated photon production in hadronic final states is presented. Our isolated photon spectrum again indicates the existence of final state radiation. Also the Lund Monte Carlo has been found to be inadequate to describe the radiative correction; the program gives about 24% less isolated photons than measured experimentally. The forward-backward charge asymmetry of quark jets with respect to the incoming beam direction in the $e^+e^- \to q\bar{q}\gamma$ processes has been measured to be 0.000 ± 0.102, with the theoretical prediction of -0.112 ± 0.039. Because of the limited statistics of our

experiment, no conclusive results for the asymmetry can be reported. Finally a search of a new heavy neutral scalar particle H° via the process $e^+e^- \rightarrow H^\circ + \gamma$ has been performed. No evidence for the existence of H° is found. The upper limits for the cross section of the new process have been set at the 95% confidence level for the H° mass region of 15–40 GeV.

Bibliography

[1] S. Weinberg, Phys. Rev. Lett. **19**, 1264 (1967);
S. L. Glashow, Nucl. Phys. **22**, 579 (1961);
A. Salam, *Proceedings of the Eighth Nobel Symposium on Elementary Particle Theory, Relativistic Groups and Analyticity*, Stockholm (1968).

[2] S. Gusken *et al.*, Phys. Lett. **155B**, 277 (1985);
W. J. Marciano, Phys. Rev. **D29**, 580 (1984);
J. Jersak, E. Laermann and P. M. Zerwas, Phys. Rev. **D25**, 1218 (1982);
T. Appelquist and H. D. Politzer, Phys. Rev. **D12**, 1404 (1975).

[3] W. Gelmaster and R. J. Gonsalves, Phys. Rev. Lett. **44**, 560 (1980);
V. G. Chetyrkin *et al.*, Phys. Lett. **85B**, 277 (1979);
M. Dine and J. Sapirstein, Phys. Rev. Lett. **43**, 668 (1979).

[4] R. Bundy, Phys. Lett. **45B**, 340 (1973).

[5] S. G. Gorishny, A. L. Kataev and S. A. Larin, Phys. Lett. **212B**, 238 (1988).

[6] F. A. Berends, R. Kleiss, and S. Jadach, Nucl. Phys. **B202**, 63 (1982);
F. A. Berends *et al.*, Comput. Phys. Commun. **29**, 185 (1983);
F. A. Berends and R. Kleiss, Nucl. Phys. **B178**, 141 (1981).

[7] J. Fujimoto and Y. Shimizu, Mod. Phys. Lett. **A3**, 581 (1988);
J. Fujimoto, K. Kato and Y. Shimizu, Prog. Theo. Phys. **79**, 701 (1988).

[8] AMY Collab., T. Kumita *et al.*, Phys. Rev. **D42**, 1339 (1990);
AMY Collab., T. Mori *et al.*, Phys. Lett. **B48**, 499 (1989);
AMY Collab., H. Sagawa *et al.*, Phys. Rev. Lett. **60**, 93 (1988).

[9] T. Sjostrand, Int. J. Mod. Phys. **A3**, 751 (1988).

[10] B. Anderssen, G. Gustatsson, G. Ingelman, and T. Sjostrand, Phys. Rep. **97**, 33 (1983).

[11] T. Sjostrand and M. Bengtsson, Comput. Phys. Commun. **43**, 367 (1987).

[12] T. Sjostrand, *A Manual to the Lund Monte Carlo for Jet Fragmentation and e^+e^- Physics, JETSET version 7.2*, CERN/TH (1989).

[13] R. D. Field and R. P. Feynman, Nucl. Phys. **B136** 1 (1978);
P. Hoyer *et al.*, Nucl. Phys. **B161**, 349 (1979);
A. Ali *et al.*, Phys. Lett. **93B**, 155 (1980).

[14] G. C. Fox and S. Wolfram, Nucl. Phys. **168**, 285 (1980);
R. D. Field and S. Wolfram, Nucl. Phys. **B213**, 65 (1983).

[15] B. R. Webber, Nucl. Phys. **B238**, 492 (1984).

[16] T. D. Gottschalk, Nucl. Phys. **B214**, 201 (1983); **B239**, 325 (1984); **B239**, 349 (1984).

[17] JADE Collab., W. Bartel *et al.*, Z. Phys. **C28**, 343 (1985);
CELLO Collab., H. J. Behrendt *et al.*, Z. Phys. **C20**, 207 (1983);
TASSO Collab., W. Brandelik *et al.*, Phys. Lett. **108B**, 71 (1982).

[18] F. A. Berends and R. Kleiss, Nucl. Phys. **B177**, 237 (1981);
M. H. Ye and P. Gu, private communication.

[19] E. Laermann *et al.*, Nucl. Phys. **B207**, 205 (1982).

[20] W. T. Ford *et al.*, Phys. Rev. Lett. **51**, 257 (1983);
K. Sazaki, Phys. Rev. **D24**, 1177 (1981);
S. J. Brodsky *et al.*, Phys. Rev. **D14**, 2264 (1976).

[21] JADE Collab., D. D. Pitzl *et al.*, JADE preprint (1989);
TASSO Collab., W. Braunschweig *et al.*, Z. Phys. **C41**, 385 (1988);
M. S. Gold, *Doctoral Thesis*, LBL-22434 (1986);
JADE Collab., W. Bartel *et al.*, Z. Phys. **C28**, 343 (1985);
MAC Collab., E. Fernandez *et al.*, Phys. Rev. Lett. **54**, 95 (1985).

[22] V. D. Barger and R. J. N. Phillips, *Frontiers in Physics—Collider Physics* (Addison-Wesley Publishing Co., 1987).

[23] A. Ali, *Phenomenology of the Higgs Boson*, DESY 81–060 (1981).

[24] A. Ali and G. Mikenberg, Z. Phys. **C3**, 147 (1979);
F. Wilczek, Phys. Rev. Lett. **39**, 1304 (1977).

[25] ALEPH Collab., D. Decamp *et al.*, CERN–EP/90–16 (1990);
OPAL Collab., CERN–EP/89–174 (1989);
F. Abe *et al.*, FERMILAB–Pub–89/250–E (1989), to be published in Phys. Rev. D;
G. D. Barr *et al.*, CERN–EP/89–156 (1989), to be published in Phys. Lett. B;
R. N. Cahn, Rep. Prog. Phys. **52**,389 (1989);
CLEO Collab., M. S. Alam *et al.*, Phys. Rev. **D40**, 712 (1989);
A. Snyder *et al.*, Phys. Lett. **229B**, 169 (1989);
P. Yepes, Phys. Lett. **229B**, 156 (1989);
M. Davier and H. Nguyen Ngoc, Phys. Lett. **229B**, 150 (1989);
P. Yepes, Phys. Lett. **227B**, 182 (1989);
S. Egli *et al.*, Phys. Lett. **222B**, 533 (1989);
CUSB Collab., P. Franzini *et al.*, Phys. Rev. **D35**, 2883 (1987);
N. Baker *et al.*, Phys. Rev. Lett. **59**, 2832 (1987);
I. Beltrami *et al.*, Nucl. Phys. **A451**, 679 (1986);
S. J. Freeman *et al.*, Phys. Rev. Lett. **52**, 240 (1984).

[26] T. Mori, *Doctoral Thesis*, University of Rochester Report UR–1104(1988).

[27] D.G. Cassel and M. Ogg, *DUET — A Track-Finding Program for Cylindrical Geometries*, CLEO Internal Report (1983).

[28] F. Kajino, A. Abashian, and K. Gotow, Nucl. Inst. Meth. **A245**, 507(1986).

[29] S. S. Myung, *Doctoral Thesis*, korea University (1988).

[30] Y. Doi *et al.*, Nucl. Inst. Meth. **A274**, 95(1989)

[31] S. Igarashi, *Doctoral Thesis*, Tokyo Institute of Technology (1988).

[32] S. K. Kim, *Doctoral Thesis*, Korea University (1988).

[33] H. J. Kim, *Doctoral Thesis*, Korea University (1989);
F. Kajino, AMYNOTE 369.

[34] M. Bengtsson and T. Sjostrand, Phys. Lett. **185B**, 435 (1987).

[35] M. Bengtsson and T. Sjostrand, Nucl. Phys. **B289**, 810 (1987).

[36] T. Sjostrand, private communication.

[37] HRS Collab., H. Althoff *et al*, Phys. Rev. **D31**, 1 (1985);
MARK II Collab., A. Petersen *et al.*, Phys. Rev. **D37**, 1 (1988).

[38] TASSO Collab., H. Althoff *et al.*, Z. Phys. **C22**, 307 (1984);
TASSO Collab., W. Braunschweig *et al.*, DESY 88–107 (1988).

[39] AMY Collab., Y. K. Li *et al.*, Phys. Rev. **D41**, 2675 (1990).

[40] K. Kato and T. Munehisa, *Electron Positron Collision Simulator*, KEK report 87–5 (1987).

[41] *Review of Particle Properties*, Phys. Lett. **B239**, (1990).

[42] W. R. Nelson it et al., *The EGS_4 Code System*, SLAC–Report–265 (1985).

[43] A. Grant, Nucl. Inst. Meth. **131**, 167 (1975).

[44] E. J. Kim, private communication.

[45] Y. Kurihara, *Systematic Error of the Luminosity Measurement by the PTC*, AMYNOTE 504(1989).

Vita

Kangping Hu (Loewenstein) was born on March 27, 1963, in Xi-An, People's Republic of China. In 1984, she received her B.S. in physics from Beijing University in Beijing, People's Republic of China. She taught physics in Shanghai Railway Medical College from 1984 to 1986. She received her M.S. in physics from Virginia Polytechnic Institute and State University in May, 1990. She received her Ph.D in physics from Virginia Polytechnic Institute and State University in August, 1991. During her studies at VPI, she has been a research assistant in high energy physics, working on the AMY experiment at TRISTAN. Her thesis advisor has been Alexander Abashian.

Kangping Hu